Stochastic modeling of active biological transport in inhomogeneous environments

Dissertation

zur Erlangung des Grades
des Doktors der Naturwissenschaften
der Naturwissenschaftlich-Technischen Fakultät II
— Physik und Mechatronik —
der Universität des Saarlandes

von
Philip Greulich

Saarbrücken
2009

Tag des Kolloquiums:	26. März 2010
Dekan:	Prof. Dr. Christoph Becher
Mitglieder des Prüfungsausschusses:	Prof. Dr. Karin Jacobs (Vorsitzende) Prof. Dr. Ludger Santen (Doktorvater und 1. Berichterstattender) Prof. Dr. Andreas Schadschneider (2. Berichterstattender) Dr. Christian Hoffmann (Beisitzer)

Contents

Abstract

This thesis considers systems of actively driven particles on biased tracks in inhomogeneous environments. One example is vehicular- and pedestrian traffic. The main focus of this work, however, is on modeling collective directed motion of molecular motors involved in protein production or the transport of cargo on intracellular filaments.

Transport on inhomogeneous tracks exhibits a jamming transition that emerges if the particle current attains the *transport capacity* of a bottleneck, which marks the maximum current. Jamming can be observed in traffic, but also for molecular motors. An analytical scheme to predict the transport capacity and critical parameters of this transition is developed. The presented models apply to tracks with slow sites (*defects*). These can for example be induced by biomedical drugs. In the context of intracellular traffic, defects are presently discussed as a cause of several diseases, e.g. Alzheimer's disease. Particular codons on mRNA can also slow down ribosomes.

Furthermore, transport on (filament-) networks is investigated. It is shown that particle clusters emerge. In contrast to regular networks or diffusion limited (reversible) aggregation, inhomogeneous networks exhibit a scale-free distribution of cluster sizes. This result can help to distinguish microscopic dynamics and structures by analyzing macroscopic particle cluster patterns. Applied to clusters of membrane proteins that promote the internalization of toxins, an analysis of clusters might improve the understanding of toxic pathways.

Kurzzusammenfassung

Diese Arbeit behandelt Systeme aktiv getriebener Teilchen auf gerichteten Pfaden in inhomogenen Umgebungen. Ein Beispiel ist Straßenverkehr. Hauptgesichtspunkt ist jedoch die Modellierung gerichteter kollektiver Bewegung von molekularen Motoren bei Proteinproduktion oder Transport auf intrazellulären Filamenten.

Auf inhomogenen Bahnen können Staus auftreten, wenn die *Transportkapazität* eines Engpasses (Maximalwert des Stromes) erreicht wird. Staus können sowohl im Verkehr, als auch bei molekularen Motoren beobachtet werden. Es wird eine Analytische Methode zur Vorhersage von Transportkapazität und kritischen Parametern für Staubildung entwickelt. Das Model kann auf Systeme mit langsamen Stellen (Defekte) angewandt werden, die z.B. durch künstliche Wirkstoffe erzeugt werden. Es wird vermutet, dass Defekte in intrazellulärem Transport Auslöser von Krankheiten wie z.B. der Alzheimerkrankheit seien. Bestimmte Kodone können außerdem Ribosomen auf mRNA bremsen.

Zusätzlich wird Transport in (Filament-) Netzwerken untersucht. Es wird gezeigt, dass Teilchen-Cluster entstehen. Im Gegensatz zu regulären Netzen oder (reversibler) diffusionsbegrenzter Aggregation, weisen inhomogene Netze eine skalenfreie Größenverteilung auf. Diese Ergebnisse können helfen, von makroskopischen Cluster-Mustern auf mikroskopische Strukturen und Dynamik zu schließen. Im Hinblick auf Membranprotein-Cluster, die die Aufnahme von Toxinen fördern, kann eine Untersuchung der Cluster das Verständnis der Internalisierung von Toxinen verbessern.

Chapter 1

Introduction

The dynamics of many complex systems is based on active transport processes. For example vehicle and pedestrian traffic constitute part of the infrastructure for human society and economy, while the metabolism of biological cells is maintained by transport of vesicles and organelles mediated by motor proteins. In this terminology active transport is characterized by biased dynamics of driven or self-propelled objects with a preferred direction in contrast to passive, undirected transport e.g. by diffusion.

In recent decades modeling active transport systems in social and biological context increasingly came into the focus of statistical physics [14, 15, 23, 27, 48, 53, 54, 64, 69, 71, 75, 85]. At first glance most of these systems do not appear to be treated by physics. However, despite their diversity in scale and interactions, these systems are conceptually quite similar and they can in fact be analyzed by applying methods of non-equilibrium statistical mechanics. First of all, modeling implies a simplification of (the usually quite complex) dynamics and states of the system. A powerful approach for modeling complex systems without losing crucial properties is the introduction of *stochastic transition rates* instead of deterministic dynamics. This way, complex subprocesses that are involved in a specific transition process of one state of the system into another can be captured by phenomenological transition rates that serve as parameters for the model system. For given discrete time steps, these rates are implemented as transition probabilities. The stochastic approach is appropriate, since due to the complexity of the considered systems a deterministic prediction of the time evolution is not possible. Thus stochastic model systems can be constructed that are accessible by analytical and numerical methods of statistical mechanics.

This work is mainly motivated by transport processes in biological cells, in particular transport by molecular motors attached to biopolymers. These macromolecules consume chemical energy to move along biopolymer tracks in a directed manner. For example cargo is transported by motor proteins that move along polarized cytoskeletal filaments in one direction. A similar process is performed by RNA-polymerase and ribosomes [2]. These molecular motors move along nucleic acid strands to read the DNA/RNA-sequence template sequentially and polymerize mRNA/proteins. Although no cargo is transported in this process, the basic dynamics and topology (collective directed motion with steric interactions) are similar and the production rate of mRNA/proteins as well as the delivery rate of cargo is determined by the particle current. There-

fore they are treated in a similar manner as "transport" systems, using the same terminology.

Many results (at least those of chapter 3) are generic for a larger class of transport systems which show the following common features:

1. They are "driven" systems, i.e. the average motion of components is, at least locally, biased in one direction, corresponding to a permanent drift. This drift can originate from an external potential gradient (combined with a pumping mechanism) or by self-propelled components (i.e. vehicles, pedestrians, molecular motors). The continuous drift implies that they are non-equilibrium systems requiring a steady energy input.

2. Components cannot interpenetrate each other. This is due to their steric repulsion. In traffic models this interaction is implemented as an exclusion rule.

3. The active transport takes place on quasi-one-dimensional tracks that are strongly confining the components in all but one dimension, so that blocking of components due to exclusion is relevant.

These features are obviously exhibited for example in highway traffic, pedestrian and evacuation dynamics, intracellular transport and granular transport through narrow tubes. Also data processing in computer networks exhibit similar features [14].

In the past, many transport systems have been modelled and extensively investigated by numerical and analytical methods. A widely used class of systems that are used to model active transport with the features listed above are stochastic cellular automata known as *driven lattice gases* which describe biased particle hopping dynamics on a lattice. One prominent example of a model system for active transport on a single track is the *asymmetric simple exclusion process (ASEP)* [66, 92] whose *totally* asymmetric version (TASEP) is probably the most simple non-trivial active transport model that covers the properties listed above. Its dynamics and phenomenology are spotlighted in chapter 2.3. The TASEP serves as a paradigmatic model, since, despite its simplicity, it exhibits some generic phenomena that can be observed in real transport systems. One observes *boundary induced phase transitions* [60], e.g. one between a low and high density phase if particle influx exceeds a critical value, leading to a situation similar to a traffic jam. Slight extensions of the TASEP [75, 27] make it suitable for modeling intracellular transport processes and predict some of their phenomenology [71]. What makes the TASEP interesting from a theoretical point of view is the fact that its steady state can be exactly solved [17, 86], which is a rare feature of non-equilibrium systems.

Most of the investigations on transport systems have been performed for homogeneous systems where transition rates do not depend on the position in the system and are equal for all components. However, usually real systems are spatially inhomogeneous. For example in highway traffic there can be roadworks where the average velocity of vehicles is decreased. In particular in the biological example of intracellular transport inhomogeneities are abundant. Macromolecules can bind to cell filaments and locally impede movement of motor proteins (e.g. *microtubule associated proteins (MAPs)* [2, 93] or artificial blockages [22, 88]). Polymerization of proteins by ribosomes (translation) does not

occur with constant velocity, but the process depends on local patterns of the mRNA-sequence. Modeling these systems requires spatially varying transition rates.

Candidates for modeling inhomogeneous single track systems are driven lattice gases with site-dependent transition rates. Most investigations have been performed on the inhomogeneous ASEP, mainly with periodic boundary conditions [5, 12, 19, 24, 29, 46, 47, 50, 61], that revealed a number of effects not observed in homogeneous systems. Even the presence of a single *defect* (site with lower transition rate) leads to the emergence of qualitative new macroscopic phenomena such as a jamming transition in front of the defect [46]. However, right now only for inhomogeneities associated to particles, the TASEP is solved exactly (for periodic boundary conditions in [62]). For generic driven lattice gases with site-associated inhomogeneities, despite a few analytical results [47, 12, 56], a deep analytical understanding is still pending.

In many transport systems, several tracks for transport are connected with each other to form complex networks (streets, actin filaments in cells). Since objects cannot interpenetrate each other, objects travelling on different tracks can block each others movement[1]. The inhibition of movement effectively lowers the passing rate at these points, hence intersections act as defects on either of the crossing tracks and traffic jams can be induced [15].

Not only just the presence of intersections but also the global structure of networks appears to have impact on large scale dynamics of transport. In [73] transport of particles on an inhomogeneous topological network (graph with nodes connected by links) was shown to exhibit an inhomogeneous distribution of particles despite undirected particle dynamics and absence of interactions. However, until now studies of transport on inhomogeneous networks did not take into account the explicit spatial structure (i.e. distances and angles) together with steric interactions of active transport objects. In these systems new phenomena are expected.

Due to the complexity of intracellular processes and thermal fluctuations, microbiological systems often assemble in a rather random fashion. Single cytoskeletal filaments can exhibit an inhomogeneous, disordered structure, since macromolecules attach randomly at distinct binding sites of filaments (e.g. degenerated tau proteins in neurons affected by Alzheimer's disease [93]). On the other hand networks of filaments that constitute the cytoskeleton often exhibit a non-regular structure (in particular actin networks) due to the growth dynamics and thermal fluctuations on prevailing length scales. A main focus of this thesis will therefore be on *disordered* model systems, characterized by a random generation of the system structure, hence statistical properties of ensembles of systems appear to capture the properties of the system rather than single samples. While *disordered driven lattice gases*, exhibiting randomly distributed defects are used to model transport on single inhomogeneous filaments, a network of randomly distributed and orientated TASEP-like tracks appears appropriate to model transport on parts of the cytoskeleton.

The investigations presented in this work will be separated in two parts:

Chapter 3 considers driven lattice gases with inhomogeneous transition rates,

[1] This interaction can also be mediated indirectly, e.g. by traffic lights at intersections, see e.g. [15].

suited to model transport on inhomogeneous filaments and nucleotide templates, such as actin, microtubules and DNA/mRNA. The goal of this part is the development of an analytical approximation scheme for macroscopic properties like average transport currents and phase transitions. The main interest will be in disordered systems, where site-wise inhomogeneities (*defects*) are randomly distributed. Therefore statistical tools like extreme value statistics are used to relate properties of random configurations to specific configurations of single stretches of defects (*bottlenecks*), for which analytical results can be obtained. While in this chapter mainly the TASEP with some extensions is considered, it is claimed that the introduced principles have a rather generic character and can be applied in a similar manner also to other disordered driven lattice gases.

In chapter 4, a model for intracellular transport of vesicles on actin filament networks is introduced. The model explicitly includes the growth dynamics of actin filaments, whose stochastic character leads to an disordered, inhomogeneous structure of the network. By modeling vesicles as extended hard-core particles, one observes the formation of particle clusters. While in most recent publications, cluster formation was related to attractive interactions of particles (e.g. [18, 67, 31]) this indicates that transport induced cluster formation can also play a role in aggregation of macromolecules inside cells and in the plasma membrane. The goal is to identify robust properties of cluster distributions and point out differences to diffusion limited aggregation and regular networks. On a cellular level it is easier to observe clusters than single proteins by optical techniques. Hence, relating macroscopic properties of cluster distributions with microscopic dynamics can provide tools for experimental identification of microscopic dynamics. The second part of the chapter studies the effect of confining boundaries on network structure and particle dynamics. These boundaries break translational symmetry of the system that influences particle- and network dynamics.

Chapter 2

Theoretical background

In this chapter the biological and physical facts that constitute the foundation for the theoretical treatment of (intracellular) active transport systems, including gene expression processes, are introduced. In the first section the biological background is discussed, basically referring to the textbook of Alberts et al. [2], if not stated differently. Also figures are taken from this book. In section 2.2 some basic concepts to develop stochastic models for complex systems are presented, especially those tailored for intracellular transport and their implementation as computer simulations. Models of this kind are *driven lattice gases*, for example their most simple and common representative, the *totally asymmetric simple exclusion process (TASEP)*, which are presented in section 2.3. Despite being a rather simple system, the relevance of the TASEP is due to its wide applicability, since it is the basic system from which most stochastic transport models are derived.

2.1 Collective movement of molecular motors on biopolymers

The functions of biological cells are mainly performed and regulated by proteins. These are polymers of amino acids that perform specific tasks in the cell like catalytic reactions (*enzymes*), work (*motor proteins*) or acting as structural units of the cell. Any amino acid sequences is determined according to partial nucleotide sequences (*genes*) on the DNA[1].

In order to execute their function, first proteins must be produced using the information stored in the DNA templates (*gene expression*). Then they have to be (actively) transported to the location where there action is required (*active intracellular transport*). Both processes are mainly driven by molecular motors that move along biopolymers, serving as tracks, in a directed manner. In contrast to undirected processes like Brownian motion, directed motion is a non-equilibrium process that needs to dissipate energy to maintain biased motion. Molecular motors obtain this energy by hydrolysis of nucleotides like *adenosine triphosphate (ATP)*: By dissociation of a phosphate ligand, *adenosine*

[1]The function of a protein is not fully determined by the sequence of amino acids, but by its three dimensional structure after folding. This structure can also be modified by other proteins, hence its function may indirectly also depend on other genes.

diphosphate (ADP) remains while the energy released by this process induces a conformational change that can exert work on the track bound to a molecular motor. If there are many motors on these tracks their mutual steric interaction can lead to traffic-like collective behavior.

The information for protein (amino acid) sequences is stored as sequences of nucleotides on DNA. The production of proteins by interpreting the gene templates occurs in two main steps[2]: First a gene is transcribed into a complementary mRNA-strand by the molecular motor *RNA-polymerase (RNAP)* that moves along the DNA sequence in a directed manner and polymerizes mRNA-strands. The latter fits the DNA-sequence nucleotide by nucleotide (*transcription*). Then *ribosomes* attach to the mRNA-strands and move along them to polymerize amino acid chains according to the nucleotide sequence (*translation*). The detailed dynamics will be discussed in Sec. 2.1.1. There can be many RNAPs/ribosomes on a single strand and their mutual steric interaction inhibit each others movement which can lead to traffic-like phenomena (see Fig. 2.1) [3].

Transport of proteins, but also of many other macromolecules, is crucial for maintenance of cell metabolism, since usually their function is associated with a specific location in the cell. The transport pathways can be between different cell organelles and the cytosol but also the distribution of internalized proteins from the exterior of the cells must be handled. On the other hand, secretory cells produce proteins in the interior which have to be transported to the cell membrane in order to release them to the exterior. In addition to macromolecules being transported, the organelles itself must be moved to their destined position.

Although some of these tasks can be accomplished by undirected passive transport processes like diffusion, in many cases it is necessary to transport objects to a specific position. Moreover, the size of some macromolecules and cell organelles is large, so that diffusive processes are quite slow resulting in large transport times. For the purpose of active transport, proteins are usually packed in *vesicles* (see Sec. 2.1.2). Active transport of organelles and vesicles is performed by motor proteins that attach to *cytoskeletal (intracellular) filaments* and move along them. For this purpose, work obtained by ATP hydrolysis is used to displace the protein-cargo complex steadily in a specific direction determined e.g. by the orientation and polarity of filaments and motor species. There are various kinds of filaments and motor proteins which are described in the following subsections.

Another kind of active transport by non-equilibrium processes is transport through membrane-pores against concentration gradients. However, processes of this kind are not considered in this work, since they do not exhibit traffic behavior.

While the processes involved in gene expression are not associated with the transport of cargo, not only their dynamics, but also their function is similar to collective transport: The protein production rate as well as the cargo-delivery rate of active intracellular transport is determined by the current/flow

[2]There are other subprocesses of gene expression which do not depend on molecular motors that we do not consider here.

[3]In fact the TASEP (with extended particles), commonly denoted the most simple stochastic transport (traffic) process was first developed to model RNA- and protein polymerization [66].

of involved molecular motors. In this view transcription/translation are also "transport" processes.

2.1.1 Molecular motors in gene expression

Both nucleic acids, *DNA (deoxyribonucleic acid)* and *RNA (ribonucleic acid)*, are polymers constituted by sequences of *nucleotides* that can contain the *nucleobases adenine (A)*, *guanine (G)*, *cytosine (C)*, *thymine (T)* (only in DNA) and *uracil (U)* (only in RNA), and genes are determined by the sequence of these bases. Nucleotides are complementary in a way that they fit each other in a distinct manner by hydrogen bonds to form *(base-)pairs*. G does preferentially pair with C, while A can be paired with T or U. The difference of DNA and RNA are on a structural level: Most significant is that DNA is double stranded (in a helical form), consisting of two complementary strands, paired as C-G and A-T, while RNA is usually single stranded. RNA has U instead of T in its sequence. However, T and U, while chemically different, carry the same genetic information, since they never appear together in the same sequence and both are complementary to A. Another structural difference is that nucleotides in RNA contain ribose, while in DNA they contain deoxyribose. This, however, does not affect the information procession.

The processes that transfer the information from DNA to synthesize a protein are performed in two steps: First a gene on DNA is used as template to polymerize a complementary RNA-strand (*transcription*). Some RNA-molecules can perform catalytic functions and do not code proteins (e.g. tRNA, rRNA). They are end-products of gene expression itself. However, particular RNA-molecules, so called *messenger RNA (mRNA)*, serve as template to polymerize proteins (*translation*).

Transcription is mediated by the molecular motor RNA-polymerase that attaches to the *promotor sequence* at the beginning of a gene and opens the DNA double helix. Hence it moves along the DNA in one direction polymerizing RNA with a sequence that is complementary to the DNA sequence. The RNA-polymerase moves step by step from one nucleotide to the next, while to each nucleotide a complementary one, dissolved in the surrounding, attaches. After finding the complementary nucleotide, it is added to the RNA-strand and removed from DNA. When the RNAP reaches the end of the gene, the nucleotide sequence is finished making up a complete mRNA-strand that is complementary to the DNA template.

The process of translation has similar dynamics, while the involved components differ: A molecular motor called *ribosome* attaches to an mRNA-strand, moves along it to synthesize a protein by translating the nucleotide sequence into a amino acid sequence. However this translation cannot be done by simple pairing of complementary parts as it is the case in translation. The relevant units are triples of consecutive nucleotides, so called *codons*. For each codon there is a specific type of *tRNA* which has a *anti-codon* (A codon with the complementary sequence) on one side and a distinct amino acid on the other side[4]. A ribosome moves from one codon to the next. At each codon the ribosome waits until the corresponding tRNA binds and the amino acid of the tRNA is

[4]Since a codon consists of three nucleotides, each one taken out of four possibilities (A,U,G,C), there can be up to 64 different codons. 61 of them code the 20 amino acids (degeneracy) and 3 signal the end of translation.

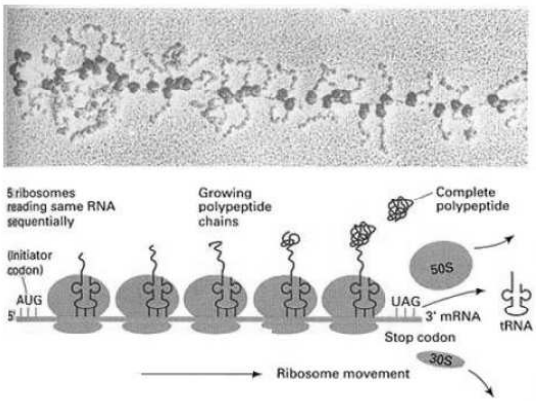

Figure 2.1: Top: Electron-microscopy of ribosomes on an mRNA-strand. One observes highly crowded ribosomes that polymerize proteins simultaneously on a single mRNA-strand. Bottom: schematic illustration of ribosome traffic. Many ribosomes move along mRNA-strands recognizing the complementary amino acids for sequential codons and polymerizing the amino acid chain. Taken from [78].

added to the polymer. This way the mRNA is uniquely translated into a protein chain.

Since the the basic properties of the dynamics are similar we assume that on a coarse grained level transcription and translation can be described by the same models. A simple model will be introduced in Sec. 2.3. The requirement of tRNA for translation gives rise to inhomogeneities in the progress of ribosomes[5]. Each codon needs a specific species of tRNA. Since the concentration of corresponding tRNA can vary between different codons, the reading velocity depends on the codon. Indeed, there are so called "slow codons" which are associated with a low concentration of corresponding tRNA, hence acting as obstacles in translation.

In general there can be many ribosomes/RNAP on a single RNA/DNA-strand. While the function of transcription/translation is not transport of cargo, the system of nucleotide strand and molecular motors has the features (1)-(3) as described in the introduction (Chapter 1) which allow traffic phenomena like jamming: Collective directed movement of particles that inhibit each others movement which makes them capable for the models that will be introduced in Sec. 2.3. Indeed, jamming of ribosomes was observed experimentally [101] (illustrated in Fig. 2.1). While in transport systems the average amount of transported cargo is relevant, here it is the production rate of RNA/proteins. However, both quantities are related to the particle current which we are interested in.

2.1.2 Vesicular trafficking

The main focus will be in the transport of folded proteins. Besides transport between intracellular compartments, there are two main processes where

[5]The complex internal dynamics of ribosomes also give rise to other sources of inhomogeneity [28].

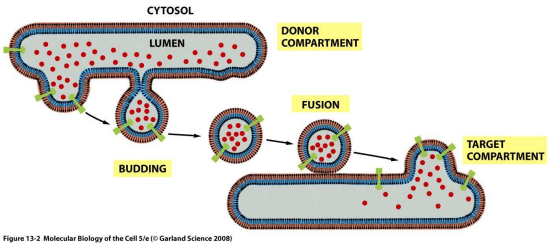

Figure 2.2: Illustration of vesicle budding from and fusion to compartment membranes. The red dots represent proteins in the lumen while pins in the membrane are membrane proteins.[2]

molecules, especially proteins, have to be transported to distinct destinations in the cell. On the *secretory pathway*, proteins that have been synthesized and folded in the interior of the cell (*cytoplasm*) are transported to the cell membrane. Here proteins might be liberated to the exterior or membrane proteins, e.g. receptors, are inserted in the cell membrane. On the *endocytic pathway*, molecules from the exterior or the cell membrane itself are internalized and transported to intracellular compartments or liberated into the cytosol. On the active pathways molecules are transported in vesicles. Vesicles are small (compared to other organelles), usually spherical, compartments that can pack folded proteins and other macromolecules in their lumen or embrace membrane proteins in the vesicle membrane (cf. Fig. 2.2) The membrane of vesicles is equivalent to the cell membrane or the membrane of cell compartments. Vesicles are generated by budding from other intracellular compartments that are enclosed by a bilipid membrane. The process is displayed in Fig. 2.2: Proteins are engulfed in their lumen (red dots) and membrane proteins (pins) are embraced by the vesicle membrane which has a coat that serves as a signature marking the target compartment for the cargo. Vesicles generated this way are hence led to their destination by a combination of passive and active transport processes. If the coat fits the signature of the target compartment, the vesicle membrane fuses with the compartment membrane. Internalized proteins are liberated into the lumen, while membrane proteins become part of the compartment membrane.

Vesicles can also bud from the cell membrane, internalizing membrane proteins and molecules from the exterior (*endocytosis*). On the other hand, vesicles from the cytoplasm can fuse with the cell membrane releasing molecules (*exocytosis*). Note that the exterior of the cell is topologically equivalent to the interior of cellular compartments.

By budding, vesicular transport and fusing, molecules are transported between different intracellular compartments. Fig. 2.3 displays the compartments proteins pass through on this way. Usually, proteins are folded into their final form at the *Endoplasmic Reticulum (ER)* near the cell nucleus. From the ER they first travel to the *Golgi Apparatus* where they are modified and distributed into vesicles that are transported to the cell membrane to fuse and release the proteins. On the endocytic pathway, proteins also pass through other compartments where they are modified.

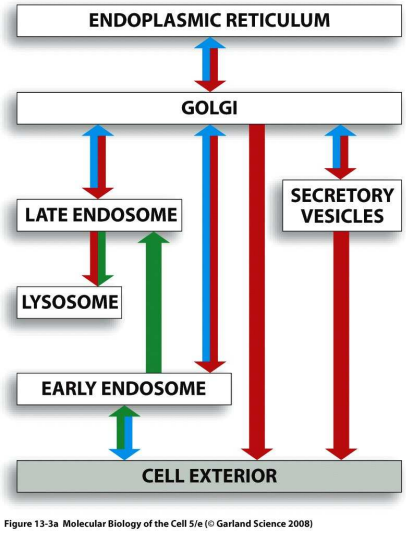

Figure 2.3: Schematic illustration of the secretory and endocytic pathways. The blocks represent cellular compartments, proteins visit on these pathways. Endocytic and secretory pathways are illustrated with green and red arrows respectively, while blue arrows denote retrieval pathways for some molecules.[2]

2.1.3 Dynamics and structure of the cytoskeleton

In cells there are two kinds of filaments that serve as tracks for motor proteins: *actin filaments* and *microtubules*. These filaments, together with *intermediate* filaments, constitute the *cytoskeleton*. The cytoskeleton serves as infrastructure for active vesicle transport as well as stabilizes cell structure and mediates cell motility. As mentioned above, the direction of active vesicle transport by motor proteins is determined by the direction and polarity of filaments. Therefore it is important how filaments are arranged in the cytoplasm. In this subsection the dynamical processes determining the structure of the cytoskeleton are discussed. For the purpose to study transport properties, only actin filaments and microtubules are considered.

Intracellular filaments are polymers which assemble and disassemble continuously. Actin filaments consist of actin monomers that are aligned linearly, forming a helical structure with a period of 37nm (cf. Fig. 2.4). Microtubules however have a more complicated structure. They consist of $\alpha - \beta-$tubulin dimers that form linear *protofilaments*. Thirteen parallel protofilaments, arranged in a cylindrical form with a diameter of about 25nm, form a complete microtubule (cf. Fig. 2.5). Polymerization and depolymerization can in principle occur at both sides of either filament species. However, the actin monomers as well as the tubulin dimers are polarized, exhibiting a *plus-end* and a *minus-end* [6]. This polarity results in different binding rates for filament subunits at the two ends. For both microtubule and actin filaments it is more favorable for subunits to bind at the plus-end.

For dissociation of subunits one has to consider hydrolysis of nucleotides bound to filament subunits. Actin monomers are usually bound to ATP/ADP

[6]The plus-end of actin is also called *barbed end*, while the minus-end is the *pointed end*.

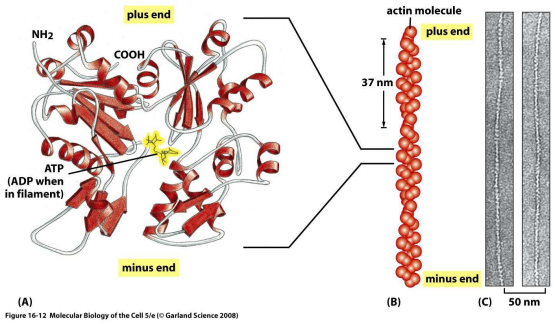

Figure 2.4: Structure of actin filaments and actin monomers. [2]

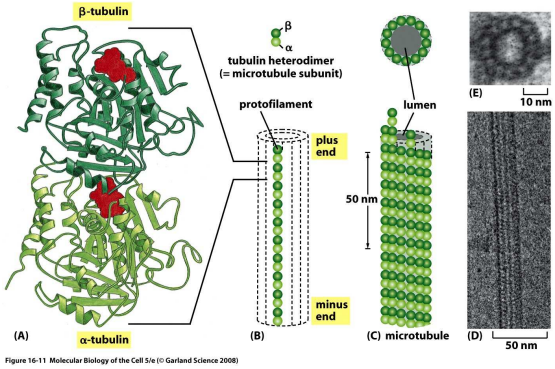

Figure 2.5: Structure of microtubules and $\alpha-\beta-$tubulin dimers. [2]

while tubulin dimers are bound to GTP/GDP (guanosine-tri-/di-phosphate). The basic dynamics is the same for actin filaments and microtubules. Hence for convenience we denote the nucleotides as XTP/XDP, where X represents the nucleosides A and G respectively for corresponding filament types. The dissociation rate of subunits containing XTP is low, while after hydrolysis (dissociation of one phosphate ligand) the dissociation rate of subunits containing XDP is strongly enhanced. Due to the asymmetry of the filaments it is much more favorable for subunits to attach to the plus-end than to the minus-end. Since usually free subunits do not hydrolyze immediately after binding, the nucleotides are in the XTP-state. Therefore the plus-end usually has a cap with XTP units with low dissociation rate. Subunits at the minus-end however have been remaining in the bound state for a longer time so that the probability that they have hydrolyzed to turn into the weakly bound XDP state is enhanced. Therefore the dissociation rate of subunits at the minus-end is much higher than at the plus-end. In summary, there is a net dissociation of subunits at the minus-end and polymerization at the plus-end which results in a process called *treadmilling* that effectively moves the filament in plus-direction. This process is displayed in Fig. 2.6.

Although the process of growing and shrinking of filaments is similar for both actin filaments and microtubules, their network structure and observed dynamics differ significantly. The microtubules are usually arranged in an or-

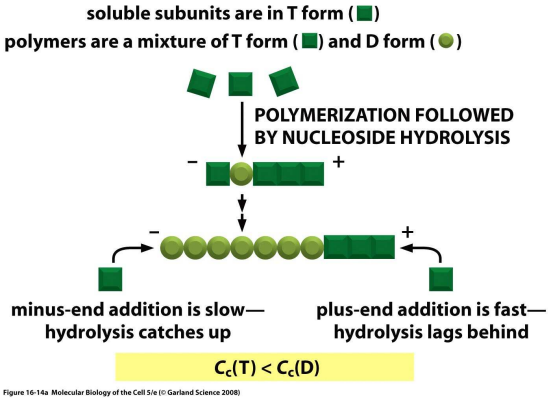

Figure 2.6: Illustration of the treadmilling process that leads to effective growth at the plus-end and shrinking at the minus-end of actin filaments and microtubules. It is driven by preferred binding to plus-end and subsequent hydrolysis of nucleoside triphosphate. [2]

dered fashion. In most cell types of multi-cellular organisms they usually form an aster-like radial structure, while e.g. in neuronal axons they are arranged longitudinally. In contrast, actin filaments often form an undirected network with an internal dendritic structure [7]. The reason for these different structures lies in the mechanisms that nucleate new filaments and inhibit dissociation at the minus-end.

In-vivo, not all actin-ATP complexes can contribute to polymerization. There are other proteins like profilin that can bind to actin monomers, so that they are not able to attach to actin filaments. Therefore the actual concentration of *free* actin monomers which can take part in polymerization is usually much less than the total concentration [16]. Spontaneous nucleation only occurs if the concentration of free monomers exceeds a critical value. Since in living cells corresponding concentrations of free actin monomers are usually much less, nucleation seeds are needed. One nucleation seed for actin filaments is the ARP2/3 protein complex. These complexes are abundant in the cytosol, so that actin filaments can nucleate anywhere in the cytosol with arbitrary initial direction. However, actin filaments are most frequently observed at the cell membrane, forming a quasi-two-dimensional disordered cortical network beneath the membrane [84]. ARP2/3 can also bind to the sides of existing filaments. Hence filaments also nucleate at the sides of filaments with a plus-end at an angle of 70^o to the parent filament (*branching*). In addition ARP2/3 stays bound for some time inhibiting dissociation at the minus-end so that dendritic structures of actin-filaments can form by branching (cf. Fig. 2.7). After some time ARP2/3 unbinds from both filaments, so that filaments shrink at minus-ends performing the treadmilling mechanism described above. While actin filaments are correlated by branching, the global structure of actin networks does not exhibit a preferred direction and orientations of filaments are randomly distributed. In addition to dendritic structures bundles of actin filaments are often encountered. These emerge due to crosslinking by several proteins like villin,

[7] Actually actin filaments mediating cell motility are directed in moving direction of the cell and also contractile bundles of actin are present. However here we only focus on transport features of actin.

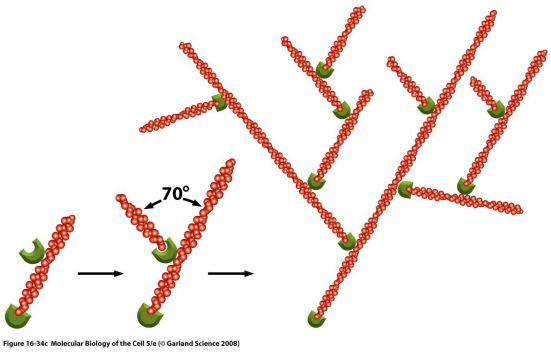

Figure 2.7: Branching of actin filaments. ARP2/3-complexes (sickles) attach at the sides of actin filaments and initialize the growth of new filaments at an angle of 70^o *to the existing one. Since ARP2/3 inhibits dissociation, dendritic structures emerge [2].*

fimbrin and motor proteins (see Sec. 2.1.4). Bundles can act e.g. as contractile elements in muscles or to deform the cell membrane. However structures of this kind usually do not contribute to vesicle transport. Actin networks can also use self-organizing mechanisms to form patterns. In [21] it was shown theoretically that transport of actin filament nuclei (actin-monomers+ARP2/3) in the minus-direction of filaments can organize the network in an aster-like pattern with radially orientated plus-ends.

For microtubules the concentration of $\alpha-\beta-$tubulin dimers is also usually less than the critical density. The nucleation of microtubules is then mediated by ring like complexes consisting of $\gamma-$tubulin. These rings aggregate to more complex bodies, the *microtubule organizing centers (MTOC)* e.g. *centrosomes* in animal cells. $\gamma-$tubulin rings are arranged in the MTOC such that microtubules nucleated there are orientated away from the MTOC [100]. Microtubules grow with their minus-end fixed at the MTOC, forming a radial aster-like structure, since $\gamma-$tubulin rings inhibit dissociation at the minus-end. When plus-ends of the microtubule aster reach the cell membrane they exhibit a force on it that leads to a positioning of the centrosome at the center of the cell near the nucleus. In contrast to actin filaments, minus-ends are liberated only rarely, so that minus-ends usually do not dissociate and treadmilling is not observed. However, one usually observes rapid dissociation of large parts of microtubules at the plus-ends (*catastrophe*) which stops at some point such that they resume growing. Beneath the cap of recently associated GTP-tubulin-dimers, usually most microtubule subunits have hydrolyzed into the weakly bound GDP-state. If due to stochastic fluctuations the cap is dissociated and GDP-dimers are at the plus-end, the microtubule starts to rapidly dissociate until an island of one or more remaining GTP-dimers is at the tip. Then dissociation is stopped and the microtubule can grow again (*rescue*). The process illustrated in Fig. 2.8 displays a possible scenario that causes catastrophe. A stochastic model for this process is e.g. studied in [3]. However, GTP islands are rare. In order to stabilize microtubules and avoid dissociation of large parts of a microtubule, proteins can stabilize microtubules. The CLIP protein, for example, attaches at the tip of a microtubule and stabilizes it by increasing the rescue rate [58].

The structures of microtubule and actin filament networks correspond to

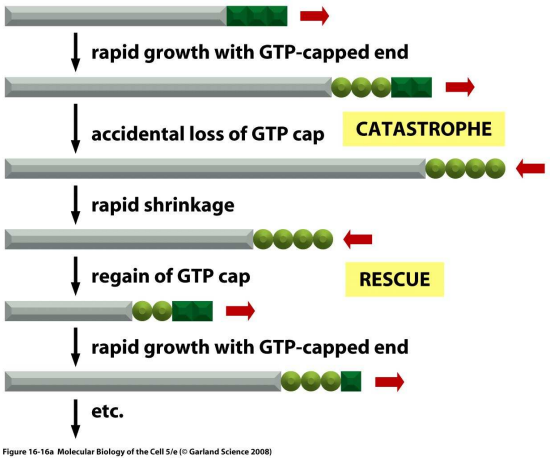

Figure 2.8: Illustration of dynamic instability of microtubules. A growing microtubule usually has a cap of tubulin dimers with GTP that inhibits dissociation. If this cap disappears, the microtubule depolymerizes fast at the plus-end until a island with GTP is reached. [2]

their function in vesicular transport of mammalian cells. The radial arrangement of long microtubules is suited for long range transport of vesicles on the endocytic and secretory pathway. The disordered structure of actin does not appear to be suited for directed transport on large scale, rather a non-directed distribution of vesicles is assumed to be mediated by the actin network. In this point of view the actin network enhances diffusion on large scales. However, results for transport on networks in chapter 4 will indicate that there might be features of transport on actin networks that provide aggregation of vesicles and macromolecules as well as radial bias of transport. This might be relevant in lower developed organisms like yeast or prokaryotes where microtubules do not contribute significantly to directed vesicle transport [45].

2.1.4 Directed movement of motor proteins

Molecular motors bind to cell structures and perform steady directed movement along them, using the energy of cyclic ATP hydrolysis. Examples are ribosomes or RNA-polymerase which bind to the corresponding nucleic acid and move along it to catalyze polymerization. However, here only cytoskeletal motor proteins are considered in order to exemplify the processes.

In general there are three super-classes of cytoskeletal motor proteins: myosin, kinesin and dynein. While myosin is associated with actin filaments, kinesin and dynein bind to microtubules. In figure 2.9 a kinesin motor protein is illustrated schematically. The basic structure of cytoskeletal motor proteins is the same for all three families. A globular *motor domain* that can bind to filaments and ATP, and a tail whose end can bind to cargo i.e. vesicles, organelles or other filaments. The motor domain is polarized and can only bind to filaments with an orientation fitting the filaments polarity. Most of the motor proteins form dimers with two coiled amino acid strands and two motor heads, while e.g. myosin II can even associate with other motors to constitute large thick filaments with the motor heads at the surface. Alternating patterns of

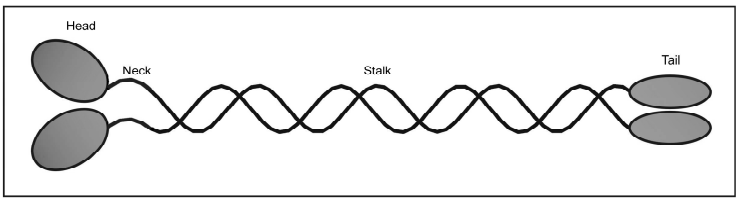

Figure 2.9: Schematic illustration of a kinesin motor protein. The main structure is generic for most motor proteins: they have a tail where cargo (e.g. vesicles) can bind and a motor domain (head) that attaches to filaments and uses the energy from hydrolysis of ATP to perform directed movement by cyclic conformational changes (taken from the homepage of K.J. Böhm).

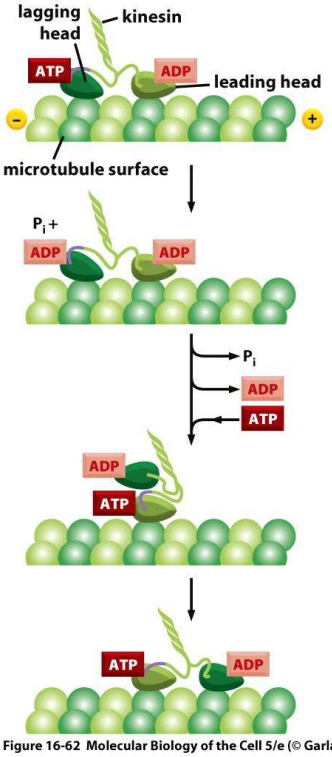

Figure 2.10: Illustration of the step mechanism of kinesin. ATP binds to the rear head of the kinesin. After unbinding of the rear head, the energy obtained by ATP hydrolysis is used for a conformational change which moves the rear head to the front where it binds to the next tubulin dimer in plus-direction of the microtubule. [2]

myosin II and actin filaments make up contractile bundles with a striated appearance. The directed movement of motor heads along actin filaments mediates contraction of these bundles as for example in muscle fibers.

The process that enables directed displacement of motors along filaments is displayed in Fig. 2.10 exemplified by kinesin. Motor proteins bind to a filament with a given polarity that fits the polarity of the motor domain. The rear head binds ATP that is dissolved in the cytosol. ATP hydrolysis, i.e. dissociation of a phosphate, provides energy and triggers a conformational change of the motor domain which releases the rear head and moves it to the front (*power stroke*). Now the latter head can bind to the tubulin dimer in front, hence the motor protein has moved one discrete step to the front direction of the filament. Thus the movement looks similar to "walking" of two-legged creatures. The length of these steps depends on the periodicity of actin filaments (37nm) and microtubule protofilaments (8nm) for respective motor proteins. The direction depends on the polarity of filaments and preferred binding orientation of motor proteins. While kinesin and most myosin species move to the plus-direction of actin filaments and microtubules respectively, dynein and myosin VI move to the minus-ends of filaments.

Also single-headed motor proteins can perform directed movement. In this case a dissipative ratchet mechanism rectifies Brownian motion, driven by an asymmetric binding potential for the motor head (cf. Fig. 2.11) [71, 36]. The motor protein can bind to a microtubule and interchanges between a strongly bound state S and electrostatic bound state W. In state S it is covalently bound to a minimum of the asymmetric potential. By use of energy from ATP hydrolysis, the motor can unbind and the potential becomes flat, though the motor cannot diffuse away from the filaments, due to an electrostatic attractive interaction [74, 36]. However, the motor protein can move freely parallel to the filament and performs Brownian motion along the microtubule. Assuming an asymmetric form of the binding potential like in Fig. 2.11, by rebinding to the filament the motor head accomplishes one step, while the probability that the motor head is at the potential well right of the initial one is higher than to be at the left one. Cyclic repetition of these steps leads to a biased net movement to the right, while left steps are not strictly inhibited.

Using these movement processes motor proteins can steadily move along filaments in their preferred direction carring cargo to their destination. Usually there is not only one molecular motor on a filament. If two motors are next to each other, they might interact by physical or chemical interactions. It is not possible for two motors to bind to the same binding site. On the other hand steric interaction of proteins and cargo objects impede free movement. This inhibition of motion can lead to collective phenomena like jamming transitions which have been observed e.g. for KIF1A-kinesin motors in vitro (cf. Fig. 2.12). This thesis mainly considers these collective phenomena that strongly influence the macroscopic transport properties of the system, while microscopic single component dynamics are only considered on a rather coarse grained scale.

In addition to motor proteins there are other molecules that bind to filaments like *microtubule associated proteins (MAPs)* that control the growth dynamics of microtubules. The presence of these proteins can influence the kinetic properties of motor protein movement, e.g. decreasing the probability that a processive step is accomplished. These inhomogeneities on cytoskeletal filaments influence the transport properties of the intracellular vesicle transport.

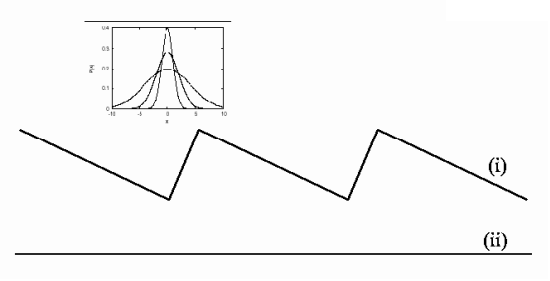

Figure 2.11: Ratchet mechanism driven by switching between a asymmetric and flat binding potential for kinesin class KIF1A. Switching occurs by dissipation of chemical energy. Since the minimum of the binding potential is nearer to the right adjacent potential well, rebinding after diffusion in the weakly bound state to the right adjacent well is larger than to the left one. This leads to a bias of movement if cyclic steps are performed. [71]

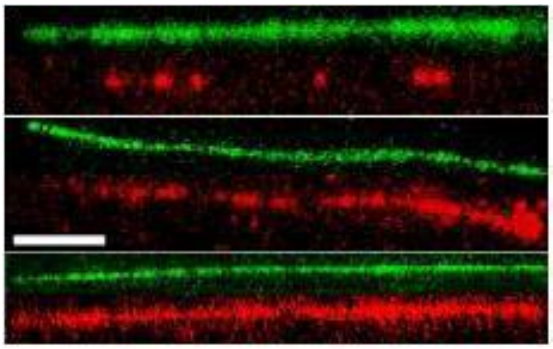

Figure 2.12: Microscopy of fluorescently labeled kinesin motors (red) and microtubule (green). The motor density is increased from the upper to lower pictures. In the middle picture, one observes a long connected stretch of kinesin, indicating the emergence of a jam. This jam coexists with a more dilute region of kinesin. [71]

They not only lower the average velocity of motor proteins but, in combination with mutual blocking, can induce additional jamming, lowering transport performance in cells. For example in neuronal axons of people suffering from Alzheimer's disease the abundant presence of tau proteins binding to microtubules is assumed to inhibit transport of neurotransmitters to the synapse and might therefore be a cause for the deleterious effect of the disease [93]. On the other hand blockages can also be artificially induced in in-vitro systems [22, 88]. The network structure of the cytoskeleton also gives rise to interactions. If two or more filaments are near to each other, e.g. at crosslinks of actin filaments, motor proteins/vesicles travelling on different filaments can mutually impede movement by steric interactions. Filament crossings hence act as defects and might be able to induce jams.

In the following the problem of quantifying the combined effects of inhomogeneities and steric interactions is approached. Therefore we look for systems that serve as models for intracellular transport processes and take into account collective effects, while being simple enough to be treatable by theoretical concepts.

2.2 Stochastic modeling

> "All models are wrong, but some of them are useful"
> George E.P. Box

In order to treat a real system quantitatively, one has to find a *model* for this system. Developing a model usually means to simplify dynamics and structure of the system by neglecting less relevant states and processes. The reasons for simplification of complex processes are manifold:

Lack of knowledge Usually not all individual processes of a real system are known in detail. Especially on the intracellular scale, sophisticated experimental techniques are necessary to identify microscopic processes and the nature of interactions. Even if they were known it would be hopeless to represent such a system in detail.

Applicability of analytical methods From a theoretical point of view it might be interesting to investigate a system by analytical or numerical methods. This, however, is not possible for very complex systems. Actually only simple non-equilibrium systems can be treated analytically yielding accurate results. Although the performance of computers is continuously increasing, it is so far not even possible to study the dynamics of single proteins in atomistic detail if they undergo large conformational changes.

Identification of relevant microscopic mechanisms A thorough identification of the most relevant processes that determine robust properties of the system is crucial for theoretical investigations. This helps to find relations between microscopic processes and macroscopic behavior of complex systems. If the underlying processes of an observed phenomenology are not known due to limited experimental techniques, modeling can help to distinguish between possible scenarios. Comparison of the robust macroscopic phenomenology (e.g. phase diagrams) of models that take into

account different microscopic mechanisms can help to identify relevant and irrelevant mechanisms for the considered phenomenology.

In order to be useful, a model must reproduce at least qualitative properties of the system. In the case of complex systems consisting of a high number of presumably interacting components, one is usually interested in macroscopic properties emerging from microscopic dynamics.

Models (even simple ones) can be used to predict new phenomena that are currently not observed experimentally. For this purpose a model must be tested on experimental data to reproduce the observed results and parameters must be carefully adjusted. Then a model can further predict phenomena e.g. in parameter regimes which are out of reach for current experimental methods.

Usually a first model only captures a part of qualitative phenomena, not to mention the quantitative accuracy. Thus existing models are gradually extended to reproduce more and more the phenomenology of the systems while distinguishing the impact of single aspects of the dynamics.

2.2.1 Developing a stochastic model

One powerful approach of modeling systems consisting of many interacting components is the introduction of stochastic transition rates instead of deterministic dynamics. This way complex subprocesses of single components can be summarized and substituted by a single transition rate that reproduces the dynamical behavior on a coarse-grained scale. This becomes necessary because the nature of interactions and microscopic details is often not known.

Models whose dynamics is given by transition probabilities are a subclass of *stochastic processes* (see e.g. [20]). The state of a system at time t is given by a *configuration vector* $\boldsymbol{\eta} = (\eta_1, \eta_2, ...)$. Time evolution is given by transition rules that determine the probabilities of possible transitions between configurations within a time interval Δt:

$$\boldsymbol{\eta}(t + \Delta t) = \boldsymbol{\eta}' \quad \text{with probability } p_{\eta(t)\to\eta'} = \omega_{\eta(t)\to\eta'}\Delta t \quad \text{for all } \boldsymbol{\eta}' \,. \tag{2.1}$$

where $\omega_{\eta(t)\to\eta'}$ is the *transition rate* which gives the probability per time interval. Usually a system without intrinsic time scale fixing Δt is defined by fixed transition rates, while the transition probabilities depend on the time step chosen in a particular implementation of the model (e.g. in computer simulations; cf. next subsection). In general, transition rates/probabilities can also depend on past states $\eta(t' < t)$, though in this thesis only *Markov processes* are considered where transitions only depend on the present state of the system $\eta(t)$. Markov processes can also be continuous so that infinitesimal time steps $\Delta t \to dt$ have to be considered. In this case individual probabilities per time interval dt vanish while *stochastic integrals* as $\int \omega\, dt$ retain a finite value. Processes of this kind are treated by *Stochastic Calculus*. In this work time-continuous systems will be approximated by discrete times so that we will always deal with time-discrete Markov processes.

Simplification of a complex process by a simple stochastic transition probability/rate can be exemplified by regarding the stepping process of molecular motors if one is interested in the collective behavior of many interacting motors.

First of all, the structure of the system is simplified. All molecular motors presented in Sec. 2.1 (cytoskeletal motor proteins, ribosomes, RNA-polymerase) move along polymers (actin/microtubules, RNA- and DNA-strands), while they can only bind to discrete sites with uniform distance a (monomers). Hence the polymer can be discretized by a one-dimensional chain or lattice of discrete sites. Although the structure of a molecular motor is quite complex, one can represent the motor as a particle at the binding position, by neglecting interactions. Instead of taking into account rates for XTP-hydrolysis (X=A,T,C,G) and the molecular dynamics involved in conformational changes, the displacement of the motor and change of the binding sites is simply modeled by the hopping of the particle to a right adjacent site with a probability p, within a considered time interval Δt [8]. While microscopic biochemical dynamics are difficult to observe experimentally, the rate that a motor goes from one site to the next can be obtained by experimental observation of the velocity v of free motors and corresponds to the hopping rate $p = v/a$. The steric interaction with the constraint that two motors cannot bind to the same place can be implemented in the model by prohibiting double occupation of sites, thus cancelling all hopping events that attempt to do. The model in this paragraph corresponds to the TASEP which will be considered in detail in the following section[9]. While the model does not provide insight into biochemical dynamics, despite its simplifications, it retains large scale collective phenomena emerging due to steric motor-motor interactions, as will be seen in the following section.

If a model in form of a Markov process with certain transition rules (2.1) is developed, it can be studied by analytical and numerical methods. The object containing the full information of a system is the probability distribution of system states at given time t, $P(\boldsymbol{\eta}, t)$, whose time evolution is given by the discrete time *Master equation* [87]:

$$P(\boldsymbol{\eta}, t + \Delta t) = P(\boldsymbol{\eta}, t) + \Delta t \sum_{\eta' \neq \eta} \left[\omega_{\eta' \to \eta} P(\boldsymbol{\eta}', t) - \omega_{\eta \to \eta'} P(\boldsymbol{\eta}, t)\right] \ . \tag{2.2}$$

The terms $\omega_{\eta' \to \eta} P(\eta', t)$ are the probability current from state η' to η. Due to conservation of probability, $\sum_\eta P(\eta, t) = 1$, the Master equation can be seen as the continuity equation for the probability distribution P (cf. Kirchhoff's law).

It can be shown [87] that in ergodic systems a unique stationary state with $P(\boldsymbol{\eta}) := P(\boldsymbol{\eta}, t) = \text{const.}$ is reached after some time. In physical systems without input of external energy, the stationary state is characterized by a balancing of probability currents between any two states η and η'. In this case the stationary state Master equation simplifies to the *detailed balance* condition

$$\omega_{\eta' \to \eta} P(\eta', t) = \omega_{\eta \to \eta'} P(\eta, t) \qquad \text{for all } \eta, \eta' \tag{2.3}$$

which is the characteristic of an *equilibrium state* that obeys time reversal invariance.

In case of active transport however, dynamics are directed and (particle) currents do not vanish. This steady current is achieved by permanent energy

[8] the time interval has to be chosen such that the transition probability is less or equal to one.

[9] In principle a model with extended particles must be considered. However if the system size is rescaled by subtracting the covered total length of particles, it can be mapped on single-site particles.

input (e.g. by ATP-hydrolysis). Therefore detailed balance is violated and stationary states of active transport systems are *non-equilibrium stationary states*. However if only partial aspects of systems are considered, some quantities (e.g. the number of attached particles in case of Langmuir kinetics) obey detailed balance and tools from equilibrium statistical physics can be applied.

There are a number of analytical approaches to solve the Master equation of non-equilibrium systems, though only for a few systems it was successful to obtain the exact form of the stationary state. Most analytical approaches rely on sophisticated approximations, while usually one is only interested in partial aspects of the system that do not rely on the explicit form of the Master equation. Not all these approaches will be discussed in general, but in the following section and in chapter 3 and 4 analytical techniques that are suited to treat particular classes of stochastic systems will be introduced.

Numerical approaches usually can be implemented in a straightforward manner for a larger class of stochastic systems which will be discussed in the following subsection.

2.2.2 Implementation as computer simulation

Stochastic systems can be analyzed by numerical methods e.g. applying computer simulations using pseudo random numbers (*Monte Carlo simulations (MC)*). For the implementation of simulations one has to meet some further conditions for Markov processes:

1. The state of the system must be representable by a finite number of variables, i.e. the configuration vector $\boldsymbol{\eta}$ must be finite-dimensional.

2. Time steps must be discrete. If a continuous system with fixed transition rates ω_i is modeled, one has to take care that $\Delta t < \min(1/\omega_i)$ to guarantee that all probabilities $p_i = \omega_i \Delta t < 1$.

For continuous systems further approximations are necessary in this case. The system state can be implemented by a vector of variables or, using object-oriented programming, by a number of objects which posses internal variables representing their individual state.

The simulation is done by computing the state of the system gradually for consecutive time steps. Assume that the system is in a state $\boldsymbol{\eta}$ at time t and transitions to other states $\boldsymbol{\eta}^i$ with probabilities $p_i = \omega_i \Delta t$ are possible within the next time step. In order to calculate the state at a time step $t+\Delta t$, one first subdivides the interval $[0,1]$ in intervals of length p_i each, i.e. $[0, p_1], [p_1, p_1+p_2], ...$, associating each interval with one of the possible transitions $\boldsymbol{\eta} \to \boldsymbol{\eta}^i$. Now a pseudo random number within $[0,1]$ is generated (see e.g. [94]). Depending on the interval this number falls in, the corresponding transition $\boldsymbol{\eta} \to \boldsymbol{\eta}^i$ will be performed and the state of the system will be updated to $\boldsymbol{\eta}_i$. During the simulation a number of quantities can be computed. Usually one is interested in averages and fluctuations of state variables and derived quantities. The obtained data can then be evaluated and compared with experimental or analytical results.

The updating scheme discussed above is usually denoted *parallel update*, since each entry of $\boldsymbol{\eta}$ is updated at the same time depending on the state of the system at time t. However, in order to implement a continuous-time system

where no intrinsic time-scale is present, it is rather convenient to use *random sequential update* rules to implement it on a discrete-time computer system. In this case not the full system is updated at once, but the system is subdivided in N subunits that mark the interacting components of the system (e.g. particles or sites in lattice systems). N times per time step, a single subunit is chosen randomly and updated following the rules. This way each subunit is chosen *on average* once per time step Δt, while there might be subunits that can be chosen more than once or not at all during an individual time step. In the following sections this kind of updating rule is usually used, if not stated else.

2.3 Driven lattice gases as models for active transport processes

In order to model active transport processes and extract useful results, one has to find a model simple enough to be theoretical treatable while exhibiting most crucial properties of active transport. In recent years *driven lattice gases (DLGs)* have been widely used to model active transport processes like highway traffic [69, 14], pedestrian dynamics [85] and intracellular transport processes [66, 13, 75, 64, 71]. In general, driven lattice gases are stochastic systems in which particles residing on lattice sites perform stochastic dynamics with a bias in moving direction, i.e. a macroscopic particle current is usually present. In addition to their position, particles can be characterized by internal states, that have influence on the dynamics. In most considerations an exclusion principle is applied that does not allow that two particles occupy the same site.

In the last section we have seen that the stepping process of molecular motors can be modeled by hopping of particles in a preferred direction, while steric interactions of motors are taken into account by prohibiting double occupation of sites (exclusion principle). The system performing these processes is known as the *totally asymmetric simple exclusion process (TASEP)* and serves as a paradigmatic model for many active transport processes. Although its dynamics is quite simple, the model exhibits some interesting macroscopic phenomena that are common in transport systems. Indeed, allowing entry and exit of particles at the boundaries, the TASEP exhibits *phase transitions* which are usually not known in one-dimensional equilibrium systems at finite temperatures. On the other hand it is one of the few interacting non-equilibrium systems that can be exactly solved [17, 86].

In this section the TASEP and related models are presented which are used to model active transport on single tracks, especially collective movement of molecular motors on single polymers (filaments or DNA/RNA-strands). In Sec. 2.3.3 some analytical approaches to these systems are introduced which can be applied to extract properties for a given subclass of driven lattice gases. Treating the systems as stochastic processes, in general we denote rates in units of the time steps and choose for simplicity a time step $\Delta t = 1$, hence probabilities and rates have the same values.

2.3.1 The homogeneous TASEP

First of all we consider the homogeneous TASEP with L sites (also referred to as *system size*), where hopping rates are equal for all sites and for all particles. The

In the bulk:

$\tau_i(t)$	$\tau_{i+1}(t)$	$\tau_i(t+\Delta t)$	$\tau_{i+1}(t+\Delta t)$	Probability
0	x	0	x	1
1	1	1	1	1
1	0	0	1	p
1	0	1	0	1-p

On left boundary:

$\tau_1(t)$	$\tau_1(t+\Delta t)$	Probability
0	1	α
0	0	$1-\alpha$
1	X	obey bulk dynamics

On right boundary:

$\tau_L(t)$	$\tau_L(t+\Delta t)$	Probability
0	0	1
1	0	β
1	1	$1-\beta$

Table 2.1: Transition rules for the open TASEP if a site i is chosen by random sequential update rules. x means an arbitrary occupation state. Note that the transition of site i was chosen to depend only on the front site by convention. This way actually the bond $(i, i+1)$ is updated once per time step on average.

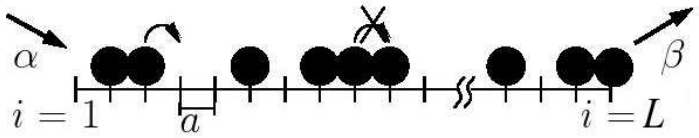

Figure 2.13: Illustration of the stochastic dynamics in the TASEP. Particles may hop to the right adjacent site with probability p if not occupied. Taken from [80].

state of the system is given by the occupation numbers τ_i at the sites $i = 1, ..., L$ aligned in one dimension. The occupation number $\tau_i = 0$ if site i is empty and $\tau_i = 1$ if it is occupied by a particle. At each time step, a particle can hop to the right adjacent site with probability p if this site is empty. If not stated explicitly, for random sequential update, we choose a time step such that $p = 1$. Stochasticity is maintained by the stochastic choice of updated sites. If the target site is occupied, no transition occurs (*exclusion principle*). The system can be implemented with periodic boundary conditions, exhibiting the topology of a ring, or *open boundary conditions* where in addition particles can enter at the left if $\tau_1 = 0$ and they can exit at the right with a rate β (*open* TASEP). At each time step, L times a site i is chosen randomly (random sequential update) and transitions take place in dependence on the occupation of the front site. The transition rules are explicitly given in Table 2.1 and illustrated in Fig. 2.13.

The TASEP exhibits a unique stationary state [17]. Due to the biased dynamics, detailed balance is broken and the stationary state cannot be an equilibrium state. Instead a macroscopic particle *current* remains. The current $J_{i,i+1}$ (also denoted as "flow") is defined as the average net number of particles

crossing a bond between site i and site $i+1$ in the positive direction at each time step. The current marks the performance of a transport system, since it corresponds to the average amount of cargo reaching a given point per time unit. Therefore this quantity is of high interest. In higher dimensional systems the current is defined as the rate of particles crossing a given plane (or other submanifold), e.g. electric charge current. The current can also be expressed in terms of the average velocity of particles $\langle v \rangle$ by $J = \rho \langle v \rangle$, where ρ denotes the *particle density*, which is defined as the average occupation number at a given site: $\rho_i = \langle \tau_i \rangle$. Moreover, the density can be used to express the boundary rates in terms of *boundary reservoirs*. The boundary conditions can also be implemented by assuming virtual sites with fixed densities $\rho_0 = \alpha/p$ at the left boundary and $\rho_{L+1} = (1-\beta)/p$ at the right boundary [60].

Due to the high relevance of the quantities J and ρ, a relation between the two contains much information about the system. Indeed for many driven lattice gases including the TASEP, a unique *current-density relation (CDR)*[10] $J(\rho)$ exists [17] which does not depend explicitly on the considered position in the system and its environment, at least in the continuum limit [11]. The current-density relation of the TASEP is shown in Fig. 2.14. One observes a maximum at half filling of the system marking the optimal density for transport. The CDR can be understood by a simple mean-field argument: since a step from site i to site $i+1$ crossing a bond and contributing to the current $J_{i,i+1}$ occurs with probability p if $\tau_i = 1$ and $\tau_{i+1} = 0$, the current takes the form

$$J_{i,i+1} = p\langle \tau_i (1 - \tau_{i+1}) \rangle \tag{2.4}$$

Applying a mean-field approximation $\langle \tau_i \tau_j \rangle \approx \langle \tau_i \rangle \langle \tau_j \rangle$ and going to the continuum limit $\langle \tau_i \rangle \approx \langle \tau_{i+1} \rangle$ one obtains

$$J(\rho) \approx p\,\rho(1-\rho) \tag{2.5}$$

which depends only on the local density ρ. Actually one can show that this approximation is exact for periodic systems and in the continuum limit also for open systems [17]. A characteristic property of driven systems, where particles cannot be created or annihilated in the bulk is the spatial invariance of the current. This is a consequence of mass conservation.

For open systems where particles can enter at the left end with rate α and exit with rate β, the system exhibits non-trivial behavior under tuning of boundary rates for $p = 1$. As long as $\alpha < \beta$, the current and the density profile far from the boundaries are completely determined by the entry rate α.

$$J = \alpha(1-\alpha); \quad \rho = \alpha, \quad \text{for } \alpha < \beta \tag{2.6}$$

Only within a finite distance from the right boundary there is an exponentially decaying *boundary layer* in the density profile whose shape depends on β. If $\alpha > \beta$, however, particles form a queue[12] and the current as well as the density (except a small boundary layer) are completely determined by the exit rate β

$$J = \beta(1-\beta); \quad \rho = 1-\beta, \quad \text{for } \alpha > \beta \tag{2.7}$$

[10] In traffic literature the CDR is usually called the *fundamental diagram*.

[11] In finite systems shocks and boundary layers can cover a finite length where this relation is not valid.

[12] The density is not exactly one, hence the queue is disrupted by holes.

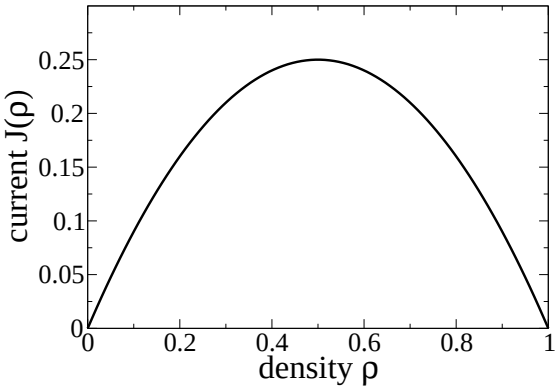

Figure 2.14: Current-density relation (CDR) of the TASEP. One observes a maximum at half filling $\rho = 0.5$. The current grows with increasing density until this point but decreases hence due to particles impeding movement by mutual exclusion interaction.

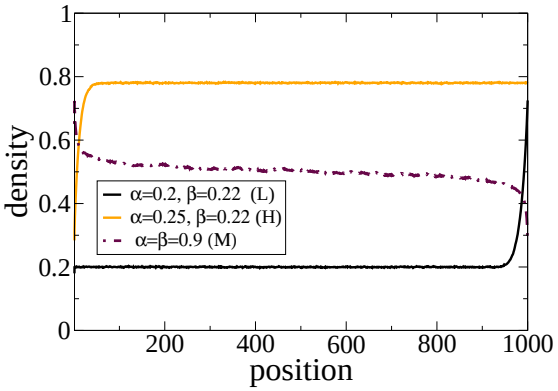

Figure 2.15: Density profiles of the TASEP in the different phases. For $\alpha < \beta$, the density profile is determined by the entry rate α in the L-phase. for $\alpha > \beta$, the density profile is determined by β (H-phase). For $\alpha, \beta > 0.5$, the density profile exhibits long-ranged, non-constant boundary layers (M-phase), while the current $J = 1/4$ is independent of the boundary rates.

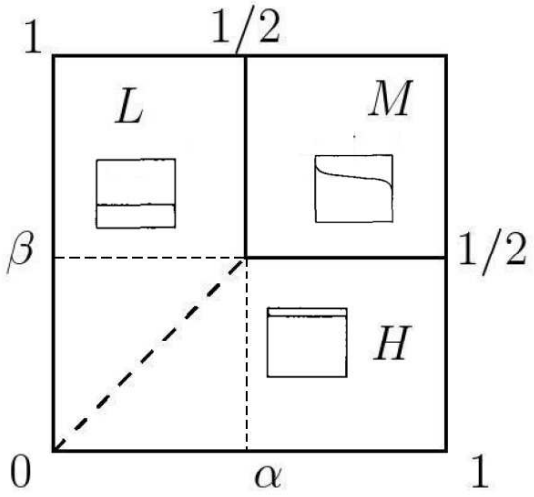

Figure 2.16: Phase diagram of the TASEP for hopping probability $p = 1$. The transition from low- (L) to high density phase (H) (bold dashed line) is of first order with a discontinuity in the density. The transition to the maximum current phase (M) is of second order since no discontinuity emerges. The insets sketch some typical density profiles $\langle\tau\rangle(x)$ in the respective phases. The thin dashed lines mark subphases, where density profiles do not differ in the bulk, but in characteristics of boundary layers [87].

Therefore at the transition point $\alpha = \beta$ the density performs a leap of $1 - 2\beta$. This discontinuity in the dependence on boundary rates is called a *boundary induced phase transition* [60]. The phase for $\alpha < \beta$ is called a low density phase (L), while for $\alpha > \beta$ one refers to a *high density phase (H)*, since the transition from L to H corresponds to a discontinuous increase of the density (see Fig. 2.15). Note that the current does not jump at this point. Besides these two phases there is a third phase for $\alpha > 0.5$ and $\beta > 0.5$, where the current is completely independent of boundary rates taking the value $J = 1/4$. In this case the current is limited by the exclusion of particles in the bulk. Long range (algebraic) boundary layers emerge, leading to an spatially varying density profile [87]. Since the current cannot exceed this value by tuning the boundary rates, the phase is called *maximum current phase (M)*. The phase diagram of the TASEP in dependence on entry and exit rate is shown in Fig. 2.16.

A crucial feature of the TASEP is the *particle-hole symmetry*: Performing the particle-hole symmetry operation

$$\tau_i \leftrightarrow 1 - \tau_i, \;\; \alpha \leftrightarrow \beta, \;\; i \leftrightarrow L - i \tag{2.8}$$

does not change system properties. This yields some restrictions on macroscopic quantities, e.g. the phase diagram must be symmetric to the diagonal in the $\alpha - \beta-$phase diagram and the CDR must be symmetric to the vertical line at $\rho = 0.5$.

Analytical treatment of the TASEP is not restricted to mean-field techniques. In fact the TASEP is one of the few interacting non-equilibrium systems that can be solved exactly, as was shown in the works [17, 86, 26] for random sequential

update and in [82] for other update rules. In [17] e.g. the TASEP with random sequential update and hopping probability $p = 1$ was solved applying a *Matrix-Product-Ansatz* (which is not discussed in detail here) yielding a "partition function" for a system of size L

$$\mathcal{Z}(\alpha, \beta, L) = \sum_{\{\tau_i=0,1\}} \mathcal{P}(\{\tau_i\}) = \sum_{j=1}^{L} \frac{j(2L-1-j)!}{L!(L-j)!} \frac{(1/\beta)^{j+1} - (1/\alpha)^{j+1}}{(1/\beta) - (1/\alpha)} \ . \quad (2.9)$$

Here $\mathcal{P}(\{\tau_i\})$ is the unnormalized probability of finding the stationary system in a configuration $\{\tau_i\}$. The current can be obtained by $\mathcal{Z}$ yielding

$$J_0(\alpha, \beta, L) = \frac{\mathcal{Z}(\alpha, \beta, L-1)}{\mathcal{Z}(\alpha, \beta, L)} \ . \quad (2.10)$$

As we will see in the following chapter this exact solution is even useful to develop an approximation scheme for the TASEP with inhomogeneous hopping rates.

2.3.2 Extended models

The phases of the TASEP indeed represent some qualitative features of transport systems with particles on narrow tracks that cannot overlap, e.g. vehicles on roads or molecular motors on polymers like intracellular filaments and nucleic acids. If only few carriers are on a track, there is free flow and the flow can be controlled by the input of carriers. However, if the input exceeds the number of carriers leaving the track a traffic jam emerges, which corresponds to the transition to the high density phase in the TASEP. Thus the TASEP, though quite simple, captures qualitative features of real active transport systems. Nonetheless, if one is interested in more detailed properties, one has to extend the model (e.g. in [69] for highway traffic). Actually in in-vitro experiments with a high number of motor proteins (kinesin KIF1A) Okada and Hirokawa observed domains on microtubules where motor proteins are crowded, exhibiting a high density, while in other domains they are dilute [74] (cf. Fig. 2.12).

In these images one observes that high and low density domain coexist on the *same track*. In the TASEP with open boundary conditions, however, high- and low density domains respectively always extend over the whole system. Phase coexistence is not observed in the TASEP.

Actually a crucial feature of intracellular motor-protein transport is missing in the TASEP: Motor proteins can attach and detach to cytoskeletal filaments at any site (*Langmuir kinetics (LK)*). In order to capture this feature, the TASEP was extended by introducing a bulk reservoir that allows attachment and detachment of particles with rate ω_a and ω_d respectively (TASEP-LK [75, 27]). This can be implemented effectively by allowing creation of particles at randomly chosen sites with rate ω_a if a site is empty and annihilation of a particle with rate ω_d .

The time evolution of sites $j, j+1$ of the TASEP-LK can be written in terms of transition rates ($1\hat{=}$ occupied, $0\hat{=}$ empty):

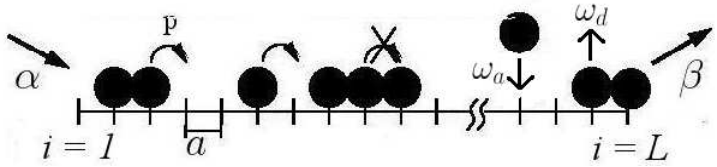

Figure 2.17: Illustration of the dynamics in the TASEP with Langmuir kinetics. In addition to TASEP rules, particles can be created with rate ω_a (attachment) and annihilated with rate ω_d (detachment). (edited from Fig. 2.13)

For $1 < j < L$:

$$\begin{array}{lll} \text{Hopping :} & 10 \to 01 & \text{with rate } p \\ \text{Attachment :} & 0 \to 1 & \text{with rate } \omega_a \\ \text{Detachment :} & 1 \to 0 & \text{with rate } \omega_d \end{array} \tag{2.11}$$

for $j = 1$:

$$\begin{array}{lll} \text{Hopping :} & 10 \to 01 & \text{with rate } p \\ \text{Entry :} & 0 \to 1 & \text{with rate } \alpha \\ \text{Detachment :} & 1 \to 0 & \text{with rate } \omega_d \end{array} \tag{2.12}$$

and for $j = L$:

$$\begin{array}{lll} \text{Attachment :} & 0 \to 1 & \text{with rate } \omega_a \\ \text{Exit :} & 1 \to 0 & \text{with rate } \beta \end{array} \tag{2.13}$$

Other transitions are prohibited. We can write the time evolution of the density $\rho_j = \langle \tau_j \rangle$ as

$$\begin{aligned} \frac{d\rho_j}{dt}(t) &= p\langle \tau_{j-1}(t)(1-\tau_j(t))\rangle - p\langle \tau_j(t)(1-\tau_{j+1}(t))\rangle \\ &+ \omega_a(1-\rho_j(t)) - \omega_d \rho_j(t) \end{aligned} \tag{2.14}$$

in the bulk and

$$\begin{aligned} \frac{d\rho_1}{dt}(t) &= -p\langle \tau_1(t)(1-\tau_2(t))\rangle \\ &+ \alpha(1-\rho_1(t)) - \omega_d \rho_1(t) \end{aligned} \tag{2.15}$$

$$\begin{aligned} \frac{d\rho_L}{dt}(t) &= p\langle \tau_{L-1}(t)(1-\tau_L(t))\rangle \\ &- \beta\rho_L(t) + \omega_a(1-\rho_L(t)) \end{aligned} \tag{2.16}$$

at the left and right boundary, respectively. The dynamics of the system with bulk rates is also illustrated in Fig. 2.17. Note that for $\omega_a = \omega_d = 0$ the TASEP is reproduced. Thus the TASEP-LK is a generalization of the TASEP.

Due to these new rules new phenomena arise, which are also shown in Fig. 2.18 and 2.19:

1. In contrast to the TASEP, the current is not spatially constant and depends on the position in the system. The same is valid for the density even far from the boundaries.

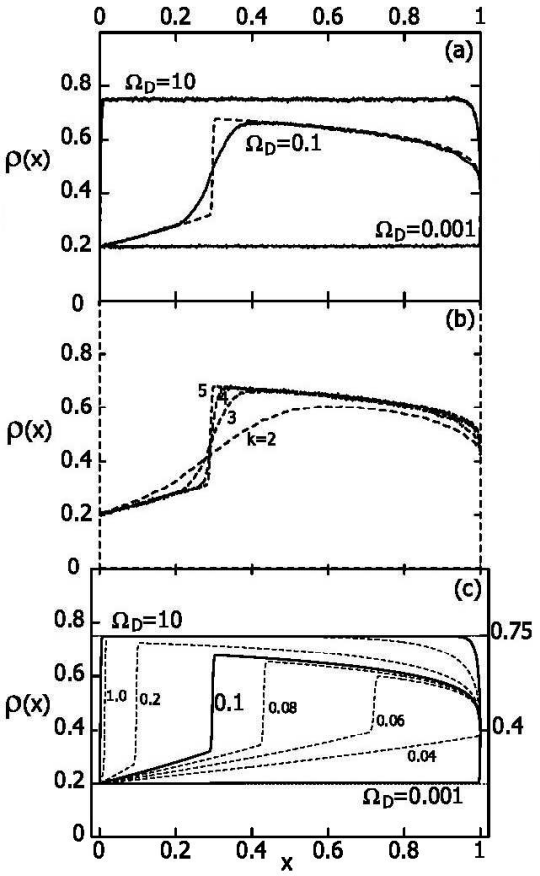

Figure 2.18: Some typical density profiles of the TASEP with LK for different relations $K = \Omega_a/\Omega_d$, $\Omega_{a,d} = \omega_{a,d}L$ [75]: (a) Density profiles obtained by numerical simulations (continuous lines) and by mean-field approximation (dashed line with $\alpha = 0.2$, $\beta = 0.6$ and $K = 3$, from (2.28)). (b) Density profiles exhibiting a shock from numerical simulations for different system sizes. One observes that for increasing system size this slope becomes steeper, indicating a discontinuity in the continuum limit ($L = 10^k$, $k = 2, 3, 4, 5$, α, β and K like in (a) and $\Omega_d = 0.1$. (c) Density profiles by mean-field approximation. α, β, K like in (a). The horizontal line at $\rho = 0.75$ is the Langmuir equilibrium $\rho_{LK} = \Omega_a/(\Omega_a + \Omega_d$ for $K = 3$. Taken from [75].

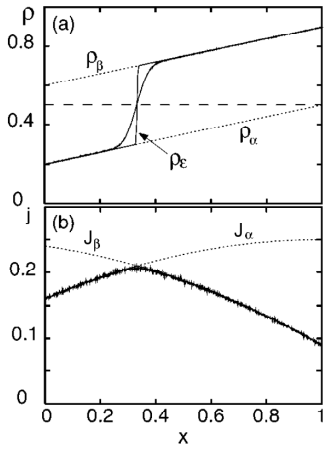

Figure 2.19: Comparison of current and density profile in the presence of a shock. One observes that the current is spatially varying and a kink is present at the position of the shock. The current profile can be constructed by two profiles determined by the boundary conditions that intersect at the shock position, as done in [27]. The mechanism of selecting global current profiles will be discussed in Sec. 2.3.3 and generalized to disordered systems in Sec. 3.3. Taken from [76].

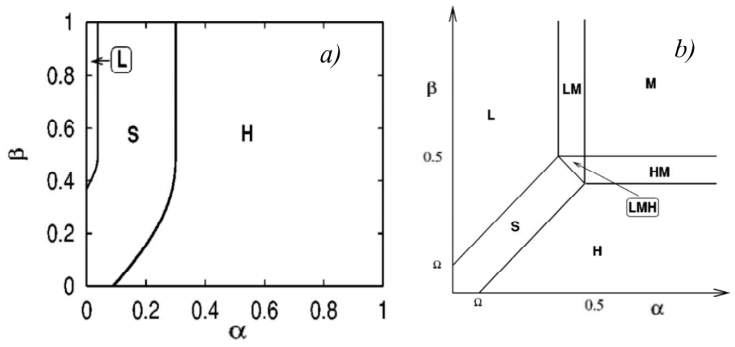

Figure 2.20: Phase diagrams in the TASEP-LK for ($\Omega_{a,d} = \omega_{a,d} L$, $K = \Omega_a/\Omega_d$) (a) $\Omega_d = 0.1$, $K = 3$: The diagram for $K < 1$ can be obtained by the particle-hole symmetry operation, together with $K \to 1/K$, $\alpha \to \beta$, $\beta \to \alpha$. For large K the low density phase vanishes as does the high density phase for low K. (b) $\Omega_d = 0.1$, $K = 1$: New subphases where a maximum-current and other phases coexist (LM,HM,LMH) emerge. Taken from [27].

2. There are parameter regimes where a high- and a low density domain coexist. They separated by a domain wall which manifests as a steep slope in the density profile. The slope increases for increasing system size. This domain wall is called a *shock* and it appears to be stationary in the TASEP-LK. The finite width of this domain wall is due to fluctuations of the shock [27, 49].

The emergence of phase coexistence corresponds to a new phase which is usually called *shock phase (S)* [27]. The phase diagram of the TASEP-LK is shown in Fig. 2.20. One observes that the S-phase is situated between L- and H-phase, the transitions between S- and H/L-phase are now of second order. For decreasing ω_a and ω_d the S-phase becomes smaller, fading into the L-H-transition line of the TASEP for $\omega_a = \omega_d = 0$. The phenomena emerging due to attachment and detachment of particles are explained by the equation of continuity in Sec. 2.3.3.

It can be shown [27, 81] that a mean-field treatment yields results for the density profiles which are exact in the continuum limit. In mean-field approximation, the time development of the the local densities can be written by

$$\frac{d}{dt}\rho_i = \rho_{i-1}(1-\rho_i) - \rho_i(1-\rho_{i+1}) + \omega_a(1-\rho_i) - \omega_d\rho_i \tag{2.17}$$

in the bulk and

$$\frac{d}{dt}\rho_1 = \alpha(1-\rho_1) - \rho_1(1-\rho_2) \tag{2.18}$$

$$\frac{d}{dt}\rho_L = \rho_{L-1}(1-\rho_L) - \beta\rho_L \tag{2.19}$$

at the boundaries. In the following section an analytical method will be introduced, that allows to find mean-field solutions for the density profiles for given boundary conditions in the continuum limit.

A more detailed model for intracellular transport is the NOSC model (named according to the authors of [71] where it was introduced). This model is tailored to describe transport by single-headed KIF1A kinesin motors. Those motors use the ratchet mechanism described in sec 2.1.4 to rectify thermal fluctuations. The NOSC model is also a driven lattice gas with exclusion interaction (no double occupancy allowed), but in addition accounts for internal chemical states of motors. Particles are allowed to be in two states, a strongly bound state 1 and a weakly bound state 2. In state 1, particles cannot move, but can change to the weakly bound state 2 with rate ω_h. This corresponds to hydrolysis of ATP which allows motors to unbind. In state 2 particles can perform a random walk along the filament, as KIF1A motors perform Brownian motion along the filament (see Sec. 2.1.4). At some point motors rebind to turn into the strongly bound state, while due to the asymmetric potential, binding to a site in front of the potential is much more favorable than binding to back site. In the model this is implemented by introducing rates ω_s for turning into state 1 at the current site, and ω_f to rebind but in addition hopping one site to the front, if the respective site is empty. In its original version, the NOSC model also includes Langmuir kinetics, i.e. particles can attach and detach (only) in state 1.

In the NOSC model movement depends explicitly on the internal particles state (only particles in the state 2 can move), while transition between states

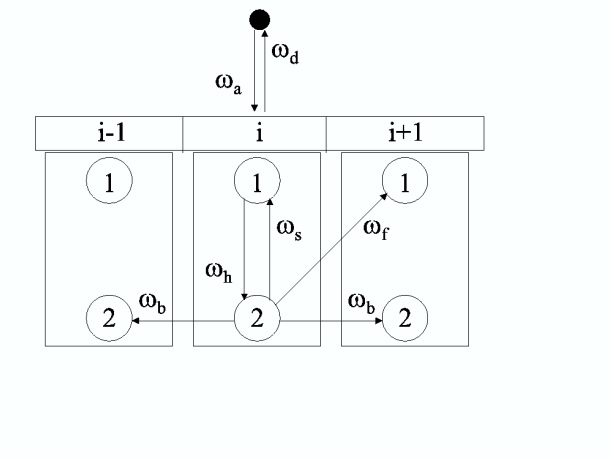

Figure 2.21: Illustration of the dynamics in the NOSC model. Particle dynamics depend on internal states of the particles, representing chemical states of motor proteins. In addition the rebinding probability depends on occupation of the front site, which marks an additional interaction to exclusion. Taken from [36]

also depends on the occupation of adjacent sites, since the total return rate to state 1 is decreased if the front state is occupied (ω_s if front site is occupied vs. $\omega_s + \omega_f$ if front site is not occupied). Hence particle-particle interaction is not merely restricted to exclusion of particles. The dynamics of the model is illustrated in Fig. 2.21, while the explicit transition rules at sites $j, j+1$ are:

in the bulk:

$$\begin{array}{lll} \text{Attachment:} & 0 \to 1 & \text{with rate } \omega_a \\ \text{Detachment:} & 1 \to 0 & \text{with rate } \omega_d \\ \text{Hydrolysis:} & 1 \to 2 & \text{with rate } \omega_h \\ \text{Rebind at site j:} & 2 \to 1 & \text{with rate } \omega_s \\ \text{Rebind at site j+1:} & 20 \to 01 & \text{with rate } \omega_f \\ \text{Random Walk:} & 20 \to 02 & \text{with rate } \omega_b \\ & 02 \to 20 & \text{with rate } \omega_b \end{array} \tag{2.20}$$

in addition on left boundary:

$$\text{Entry:} \quad 0 \to 1 \quad \text{with rate } \alpha \neq \omega_a \tag{2.21}$$

in addition on right boundary:

$$\text{Exit:} \quad 1 \to 0 \quad \text{with rate } \beta \neq \omega_d \tag{2.22}$$

random walk step to the front and rebinding to front not possible

2.3.3 Analytical approach in the continuum limit

One general property of particle conserving systems is that the particle current obeys the equation of continuity. Thus in a discrete system for any closed region

V the current obeys in the stationary state ($\partial\rho/\partial t = 0$) the relation

$$\sum_{<i,j>\in\partial V} J_{i,j} = 0 \tag{2.23}$$

where $< i, j >\in \partial V$ denotes bonds crossing the boundary of the volume V.

In one-dimensional driven lattice gases that allow exchange of particles with bulk reservoirs this corresponds to

$$J_i - J_{i-1} = s_i \tag{2.24}$$

where for convenience we denoted $J_i := J_{i,i+1}$ and the term s_i summarizes the net flux of particles in the bulk from the bulk reservoir at site i. In case of the TASEP-LK the bulk reservoir flux takes the form $s_i = \omega_a(1 - \tau_i) - \omega_d\tau_i$, while in other systems (e.g. the model in [83]), s might also depend on the occupation of neighboring sites. The continuity equation implies an interesting feature: for systems that conserve particles in the bulk, the current is always spatially constant, while if particles can be exchanged with some reservoir like in the TASEP-LK, the current might vary throughout the system.

Investigating transport systems one is often interested in systems which are large compared to its microscopic components. Therefore we consider the system in the continuum limit where the number of sites $L \to \infty$, while the lattice constant $a \to 0$ such that the total system size $L\,a$ remains constant. We introduce the continuous variable $x = \frac{i-1}{L-1}$ that denotes the relative position in the system between the left boundary at $x = 0$ and the right boundary at $x = 1$. Usually the lattice constant is not explicitly a system parameter, but the limit can be performed by rescaling other parameters that depend on the lattice spacing. Performing a Taylor expansion, one can write:

$$J_{i+1} = J_i + \frac{\partial J}{\partial x}\frac{1}{L} + O\left(\frac{1}{L^2}\right) \tag{2.25}$$

Inserting (2.25) into (2.24) yields the ordinary differential equation (ODE)

$$\frac{\partial J(x)}{\partial x} = L\,s(x) =: S(x) \tag{2.26}$$

In order to keep the crucial features of attachment and detachment, parameters have to be rescaled, so that the global source term $S(x)$ remains finite in the continuum limit. This can be achieved e.g. for the TASEP-LK by postulating that $\Omega_a := \omega_a\,L$ and $\Omega_d := \omega_d\,L$ stay constant in the continuum limit. Then also the global source term $S(x) = \Omega_a(1-\rho(x)) - \Omega_d\rho(x)$ stays constant and the ODE (2.26) is well defined. Note that in this case, the local quantities ω_a, ω_d and s vanish in the continuum limit.

If a unique current-density relation $J(\rho)$ exists in the continuum limit and the source term depends only on the density as well, the chain rule can be applied to yield the differential equation for the density profile [81]

$$\frac{\partial\rho}{\partial x} = S(\rho)/J'(\rho) \quad . \tag{2.27}$$

If the explicit forms of $J(\rho)$ and $S(\rho)$ are known, the differential equation can be solved for a given initial condition. Usually $S(\rho)$ is a monotonically decreasing function if attachment and detachment do not depend on adjacent sites.

Including interactions, however, S can increase with ρ. In this case the system might even be non-ergodic in the continuum limit (see e.g. [83]).

The problem is that usually there is more than one initial condition for the current or density profile, although the ODE is of first order. In an open system the boundary rates fix the density at the boundaries, hence at least two initial conditions are present. Each of the boundary conditions provides a completely determined solution to (2.26) or (2.27). In contrast to the physically realized profiles (*global solution*), we call solutions to individual boundary conditions *local solutions*. The global profiles must be selected from the local solutions by other criteria. In the case of the TASEP-LK the current and density profiles are spatially varying due to the finite in- and outflow of particles in the bulk. In mean-field treatment, $J(\rho) = \rho(1-\rho)$ and $S(\rho) = \Omega_a(1-\rho) - \Omega_d\rho$ and implicit formulas for the density profiles can be obtained by solving (2.27). For $\Omega_a \neq \Omega_d$ one obtains for respective boundary conditions α and β [27]:

$$\begin{aligned} x &= \frac{2(\rho_\alpha - \alpha) + \frac{K-1}{K+1}\ln\left(\frac{K-(K+1)\rho_\alpha}{K-(K+1)\alpha}\right)}{\Omega_d(1+K)} \\ 1-x &= \frac{2(1-\beta-\rho_\beta) + \frac{K-1}{K+1}\ln\left(\frac{K-(K+1)(1-\beta)}{K-(K+1)\rho_\beta}\right)}{\Omega_d(1+K)} \quad . \end{aligned} \tag{2.28}$$

The formulas can be evaluated for $\rho_{\alpha,\beta}$ to obtain the density profiles. For $\Omega_a = \Omega_d =: \Omega$ the solution is even linear to yield

$$\rho_\alpha(x) = \alpha + \Omega x \text{ and } \rho_\beta(x) = (1-\beta) + (x-1)\Omega \tag{2.29}$$

In general more than one local solution can be realized at the same time, though spatially separated and connected by a discontinuity (in the continuum limit) in the density profile called *shock* (see for example Fig. 2.18). In finite systems a shock fluctuates around its mean position, hence there is no strict discontinuity in the density profile [27, 49]. However, it can be identified by scaling the system size, if the slope becomes steeper with increasing system size. The stationary (global) current and density profiles hence result from the condition that shocks are stationary. The dynamics of shocks in driven lattice gases is discussed in a number of works (e.g. [55, 81], reviewed in [87]). Denoting the density and the current left of the shock as ρ_- and J_- respectively, while right of the shock as ρ_+ and J_+, the velocity of a discontinuity $\Delta\rho = \rho_+ - \rho_-$ results to:

$$v_s = \frac{J_+ - J_-}{\rho_+ - \rho_-} \qquad [87] \tag{2.30}$$

Since this relation is valid for any difference of the density $\Delta\rho$, the limit $\Delta\rho \to 0$ can be performed yielding the *collective velocity*

$$v_c = \lim_{\Delta\rho\to 0} \frac{J_+ - J_-}{\Delta\rho} = J'(\rho) \tag{2.31}$$

which is just the slope of the current-density relation. The collective velocity represents the velocity of perturbations $d\rho$ to stationary density profiles given by solutions of (2.27). Initial conditions, like the boundary rates which fix the density, correspond to such a perturbation, thus a local solution of a respective boundary condition can only propagate into the bulk if the collective velocity

points away from the boundary [87]. I.e. the local solutions of the left boundary condition $J_\alpha \,/\, \rho_\alpha$ can only represent physical profiles if $v_c(\rho_\alpha(x=0)) > 0$ while the local solution of the right boundary condition $J_\beta \,/\, \rho_\beta$ only propagates into the bulk for $v_c(\rho_\beta(x=1)) < 0$. For the TASEP ($p=1$) $\rho_\alpha = \alpha$ and $\rho_\beta = 1-\beta$. Since the current-density relation has a single maximum at $\rho = 0.5$, these conditions are fullfilled for $\alpha < 0.5$ and $\beta < 0.5$ respectively. Hence for $\alpha, \beta > 0.5$ none of the boundary solutions is taken in the bulk, instead the perturbations form long range boundary layers that connect to a more complicated density profile [87]. In this case, the maximum current takes the maximum value $J = \alpha_{max}(1-\alpha_{max}) = 1/4$. It can be shown [55] that for any connection of the boundary solutions by a shock for $\alpha < \beta$ (either $\alpha < 0.5$ or $\beta < 0.5$), the shock velocity is positive, such that shocks move to the right boundary, form a boundary layer suppressing the influence of β. In the opposite case, shocks with $v_s < 0$ move to the left boundary suppressing the influence of α. These three cases, characterized by the influence of boundaries that is distinguished by shock- and perturbation dynamics (bulk current profile only depending either on α (L-phase) or β (H-phase), or neither of them (M-phase)), constitute the phase diagram of the TASEP.

Since the local source term $s(\rho)$ vanishes in the continuum limit, the current profile must be continuous for $L \to \infty$. Therefore an equilibrium position x_s for shocks with shock velocity $v_s(x_s) = 0$ can only exist at some point if local solutions for the current profile of the boundary conditions are equal there. The current profiles are always flat for particle conserving systems, therefore this is only the case if both are identical. In this case however $v_s = 0$ everywhere in the system and the equilibrium position is indifferent. A stable equilibrium position allowing a stationary shock only establishes if $v_s(x < x_s) > 0$ and $v_s(x > x_s) < 0$ which can only result from intersecting non-constant profiles that are only present in systems that allow bulk in-/outflow of particles. Langmuir-kinetics therefore appear to be a crucial property to enable the formation of stationary shocks similar to the phase separation observed in the in-vitro experiments [74] with kinesin KIF1A and microtubules.

The global current- and density profile are hence determined by connecting boundary solutions by shocks at intersection points of the local current profiles. The shock fluctuations in finite systems smear out these discontinuities [27, 49], as can be seen in Fig. 2.18. It was analytically approved that a single stable upward shock ($\rho_+ > \rho_-$) can emerge in ergodic systems if local boundary solutions intersect and if following conditions are given [81, 35]:

1. Particle-particle interactions have a finite distance
2. The global bulk influx of particles S is finite in the continuum limit
3. The current-density-relation $J(\rho)$ has a single maximum
4. $S(\rho)$ is a monotonically decreasing function

The existence of a unique current-density relation and source function $S(\rho)$ is assured if conditions (1)-(2) are satisfied [35]. Moreover in this case the CDR is the same as in the corresponding particle conserving system, since the local source term s vanishes in the continuum limit. The TASEP-LK for example complies with the criteria, hence the hydrodynamic approach can be used to determine current and density profiles in dependence on system parameters

[27], using the CDR of the ordinary particle conserving TASEP. The procedure to determine the global density and current profile is exemplified in Fig. 2.19. In driven lattice gases fullfilling (1)-(4), the behavior of the shock can be used to distinguish the phases of the system. Like in the TASEP a L-phase establishes if shocks are driven to the right boundary, while the system is in a H-phase if shocks are at the right end, manifesting as boundary layers. Since the non-constance of the solutions to (2.27) allows stationary shocks in the bulk for Langmuir kinetics, this marks another phase, the shock phase (S), exhibiting phase coexistence. If boundary rates are large enough to suppress propagation of the solutions into the bulk, the system settles in a M-phase[13].

The criteria can also be applied for systems where particles may exhibit more than one internal state. One example is the NOSC model [71, 36]) where particles can be in two possible states. Here pure analytical methods cannot be applied since an exact form of the current-density relation is not known, but insertion of numerical results of the CDR in (2.26) together with shock dynamics allows the determination of the phase diagram [35] in a semi-analytical way. Since the generic properties of the shock dynamics are the same for all systems fullfilling the criteria above, the topological structure of the phase diagrams is the same for all systems of this class, irrespective on the details of the dynamics. Therefore these properties should be present also in more complex real transport systems.

In section 3.3 the hydrodynamic approach introduced here is generalized to driven lattice gases including defects with lowered hopping rate.

2.3.4 The effect of defects in the TASEP

Real transport systems usually are not homogeneous. Different species of carriers can be present that travel by different velocities. The structure of the track itself might also be inhomogeneous, for example spatially varying lane number on highways or different codons in gene translation. For modeling these systems, inhomogeneous driven lattice gases exhibiting transition rates that spatially vary can be used. Usually inhomogeneity is realized by introducing *defects*. These are sites/objects whose transition rates vary (usually lower) from usual ones[14]. In this subsection we summarize results of studies on inhomogeneous derivatives of the TASEP. In general two kinds of inhomogeneities can be considered:

particle-associated defects Hopping rates may vary between different particles.

site-associated defects Hopping rates p_j are fixed on given sites j, but are spatially varying.

Special interest is given to systems where defects are randomly distributed and the probability that a site/particle has a given transition rate is a fixed system parameter. These systems are denoted particle-/site-wise *disordered*.

While the TASEP with particle-wise disorder can be solved exactly [62], the sitewise disordered TASEP is not fully understood, not to mention disordered

[13]Since the current is not constant in the presence of LK, it is not called maximum current phase. However, like in the TASEP without LK, the current profile is independent of the boundary conditions and the corresponding phase is called *Meissner phase* [75].

[14]Of course what are the "usual" transition rates has to be defined. In some cases defects can even make up the main part of the system.

driven lattice gases in general. However, in recent years, a number of works have approached the TASEP with site-wise defects by numerical methods and analytical approximations.

Computer simulations have shown that even a single defect, i.e. a site with lowered hopping probability $q < p$, can have a global effect on the stationary state of the TASEP with periodic boundary conditions [46, 47]. For low densities the system behaves similar to the homogeneous system and only a small density peak indicates the presence of a defect. The current is not affected by the defect in this regime. However, if a critical density ρ^* is exceeded, a high density domain left of the defect emerges. This transition can also be observed in the open TASEP: Kolomeisky [56] investigated the TASEP with open boundary conditions in the presence of a single defect site deep in the bulk. Like in the periodic case, phase separation is observed if boundary rates (corresponding to the bulk density in respective phases) exceed a critical value (cf. Fig. 2.22). Providing $\alpha < \beta$, for α less than the critical value α^*, the dependence of the current on α is the same as in the homogeneous system, while above α^* there is a plateau which is not observed in the homogeneous system (Fig. 2.23). The plateau value which we will call *transport capacity* J^*, analogue to traffic engineering, is uniquely connected with the critical entry rate α^* by the ordinary CDR of the TASEP: $J^* = \alpha^*(1 - \alpha^*)$ (since $\rho = \alpha$ in the L-phase). Due to particle-hole symmetry[15], this is analogue in the high density phase with $\beta < \alpha$ if β is tuned. Hence J^* marks the maximum current that can be achieved by tuning the boundary rates:

$$J^* = \max_{\alpha,\beta} J(\alpha, \beta) \ . \tag{2.32}$$

In generic transport systems the transport capacity is the maximum current that can be achieved by tuning external (controlable) parameters, for a given fixed structure of the track. The transport capacity is a crucial quantity since it marks the optimal performance of a single-track transport system. Our analytical considerations on single-track disordered systems in the next chapter will therefore be mainly focused on this quantity to extract relevant results.

In [56] analytical results for transport capacity and phase transitions in the single-defect TASEP were obtained by a mean-field approach. It neglects correlations on the slow bond (hopping rate $q < p$) by dividing the system into two homogeneous ones, coupled at the defect site. This approach yields an approximation of the transport capacity $J^*_{\mathrm{MF}} = q/(1+q)^2$.

The investigations have been generalized to systems with a single stretch of many consecutive defects, called *bottleneck*, or two spatially separated defect sites [12, 19]. It has been shown that the problem of finding the transport capacity in such a system can be approximately transferred to an eigenvalue problem by exactly solving the Master equation of a finite segment around the bottleneck (*finite segment mean-field theory (FSMFT)* [12] . This way analytical approximations can be obtained that systematically increase in accuracy by increasing the segment size. However, solving that eigenvalue problem can result in enormous computational effort for larger segments, which limits the applicability of the method. Therefore the development of an approach that

[15] In fact if the defect is not in the middle of the system, the systems does not strictly obey particle-hole symmetry. However the symmetry operation only changes the position of the defect which does not affect the current.

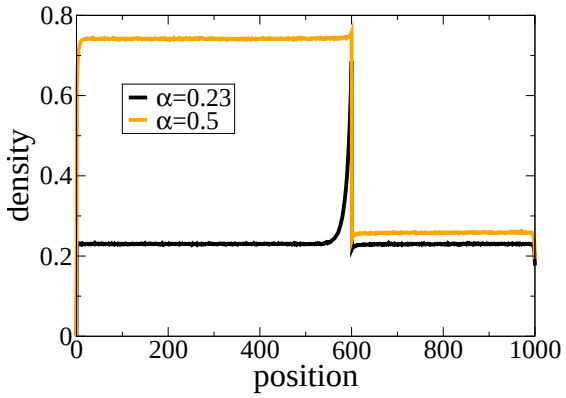

Figure 2.22: Density profiles for different entry rates in the open TASEP with a single defect. For entry rates below a critical value only a narrow peak appears, while for entry rates above that value, a high density domain left of the defect emerges [47].

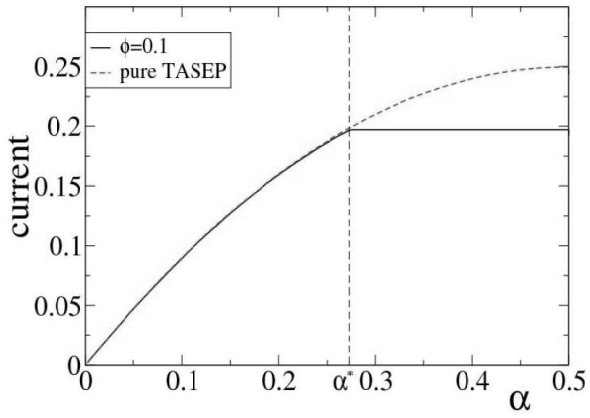

Figure 2.23: Current in dependence on the entry rate α for high exit rate in the disordered TASEP. One observes that the current is almost the same as in the homogeneous system below a critical rate α^*. If α^* is exceeded there is a plateau, in contrast to the homogeneous system. At this point also phase separation occurs (see Fig. 2.22). Since $\rho = \alpha$ in the low density phase and due to particle-hole symmetry, the left branch of the CDR is analogous.

can treat larger bottlenecks within reasonable computation time appears to be a favorable task. In Sec. 3.1 a technique solving that problem will be developed.

As argued in the last subsection, no stationary shocks can emerge in open particle conserving systems. Thus the individual high-/low density domains always extend from the defect to the boundary, while they are separated by a strict discontinuity at the defect. Note that this discontinuity at the defect is no shock, since it is also present in small systems. In contrast a shock always has a finite width in finite systems and only becomes a discontinuity in the continuum limit.

In many systems, defects are distributed in a random manner. For example in intracellular transport, macromolecules that bind randomly to filaments can disturb motor protein movement; on the other hand vesicles/motor proteins that encounter at intersections of filament networks can hinder each other. In these cases, the distinct distribution of defects is not known, while the density of defects might be controlable, e.g. by fixing the concentration of transport inhibiting macromolecules. In general, site-wise disorder can be implemented by allowing a wide range of hopping rates. The spectrum of hopping rates might be discrete [97] or continuous [42]. In this work we are mainly interested in binary disorder allowing two values for hopping rates. Hence we only consider this case in the following. Sites with fast hopping rate p are called *non-defect sites* while sites with slow hopping rates $q < p$ are referred to as *defect sites*. In this case the distribution of defects is determined by the *defect density* ϕ that denotes the probability that a given site j is a defect site, i.e.

$$p_j = \begin{cases} q & \text{with prob. } \phi \\ p & \text{with prob. } 1-\phi \end{cases} . \tag{2.33}$$

The effects of finite defect density in a periodic system have been studied in [97, 96, 61, 29], mainly numerically. Like in the single defect system there is a density regime below a critical value ρ^* and above $1-\rho^*$ where the density profile is globally homogeneous [97, 96] and a regime for $\rho^* < \rho < 1-\rho^*$ where the system is separated in a macroscopic high- and low density domain (Fig. 2.24 for open TASEP), while the current at ρ^* cannot be exceeded. While high and low density domains are rather flat on a coarse grained view, they exhibit narrow (microscopic) peaks and dents at defect sites, but these become infinitesimal small in the continuum limit. Considering the partially ASEP where disorder is realized by inhomogeneous hopping bias, a vanishing-current regime was found which shows two distinct densities, but with a current that vanishes asymptotically for ($L \to \infty$) [96]. It was found that the largest stretch of slow bonds acts as current limiting segment. For the same system, Juhász et al. [50] introduced an effective potential and determined trapping times in potential wells to investigate the vanishing of the current in a finite-size scaling.

The focus of most previous investigations on the site-wise disordered TASEP was on individual realizations of defect distributions while statistical properties of defect ensembles were rarely considered. Numerical investigations on ensembles have been made in [24], where the influence of defects on the phase transition between low- and high-density phase of the randomly disordered TASEP with open boundary conditions was studied. It was shown that the position of this phase transition is sensitively sample-dependent, even for large systems. In this thesis defect statistics are taken into account and an analytical approach

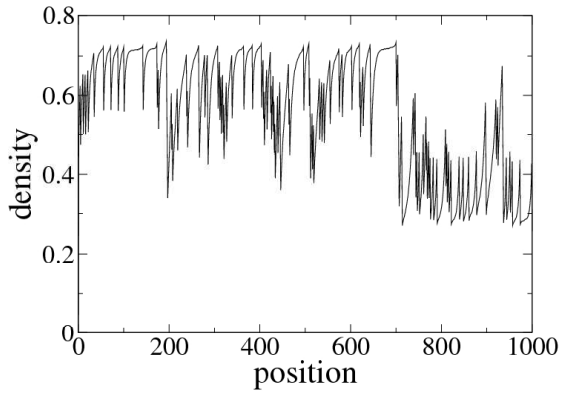

Figure 2.24: Density profile of the disordered (open) TASEP in the phase separated regime. One observes a high density domain left and a low density domain right of some defect. The domains itself are interspersed by peaks and dents at defect sites.

is developed to determine expectation values for transport capacities and critical rates (e.g. phase transitions) in disordered driven lattice gases. Krug [61] conjectured that also the maximum current is sample-dependent and is mainly determined by the longest stretch of consecutive defect sites. In particular he stated that $J^* = J^*(l)+\mathcal{O}(1/l)$, where l is the length of the longest stretch. This observation will be the starting point for our analytical studies on disordered driven lattice gases.

2.4 Networks

Many complex systems exhibit a network structure. If there is no spatial structure and only the topological properties are important, network systems are expressed as *graphs*, i.e. nodes connected by edges/links. A link denotes a (directed) relation between two nodes i and j. In this case the network structure can be represented by an adjacency matrix A whose entries A_{ij} denote the number of links going from node i to node j. One can assign a weight to node i by e.g. counting the number of out-going links $K_i^{out} = \sum_j A_{ij}$ (*out-degree*) or in-going links $K_i^{in} = \sum_j A_{ji}$ (*in-degree*). In *undirected networks*, characterized by a symmetric adjacency matrix $A^T = A$, both degrees are equal: $K_i = K_i^{in} = K_i^{out}$ [1].

Graphs can also be implemented dynamically. Links and nodes can be included, removed or rewired in time evolution. This can also be implemented as a stochastic (Markov-) process (random graphs, e.g. [25]) producing different degree distributions. On the other hand, nodes and links can possess internal states that evolve with time (*automata*). The time evolution of a node is determined by the states on adjacent nodes. The dynamics can be deterministic or stochastic[16]. Examples for deterministic automata are neuronal networks: the state of a node i, representing a neuron (active/inactive) depends on the nodes

[16]In a mathematical strict meaning only deterministic dynamics are denoted as automata, while in many physics works (and here) this term is also applied for stochastically evolving systems.

pointing on it; i.e. if the number of active nodes connected to node i exceeds a threshold value, the node becomes active itself.

Particle transport systems can also exhibit network structure. An example for stochastic dynamics is random walk of particles on a network[17]. In this case the states of the nodes correspond to the number of particles on a node. At each time step a particle randomly chooses an adjacent node hopping on it with a given probability. In undirected regular networks (e.g. regular square- or triangular lattices), particles perform diffusive dynamics ending in a homogeneous stationary state.

The homogeneous distribution, however, changes, if the structure of the network is not regular. Noh and Rieger have shown [73] that in the case of an undirected inhomogeneous network, i.e. with a non-uniform distribution of node degrees, the particle distribution for random walk dynamics is inhomogeneous. If all links are undirected and there may be only single connections between nodes, the particle density on any node is proportional to its degree i.e.

$$\rho_i = K_i/\mathcal{N} \tag{2.34}$$

where the normalization factor $\mathcal{N} = \sum_i K_i$ is the total number of links. It is easy to show that this is also valid for directed networks (also allowing nodes connected by several links) as long as $K_i^{in} = K_i^{out}$ for all i. If any particle can move within one time interval τ from one node to an adjacent node via a link, the master equation yields

$$\rho_i(t+\tau) = \sum_j \frac{A_{ji}}{K_j^{out}} \rho_j(t) \tag{2.35}$$

[18]

Inserting (2.34) and applying $K_i = K_i^{in} = K_i^{out}$, one obtains

$$\rho_i(t+\tau) = \sum_j \frac{A_{ji}}{K_j^{out}} \frac{K_j^{out}}{\mathcal{N}} = \frac{\overbrace{\sum_j A_{ji}}^{=K_i}}{\mathcal{N}} = \rho_i(t) \tag{2.36}$$

therefore (2.34) is a stationary state also for this network structure.

Obviously the network structure has high influence on particle dynamics. This becomes even more striking if particle-particle interaction is included. In [72] it was shown that inclusion of a zero-range interaction (i.e. only particles that are on the same node interact) is present, a condensation transition can occur if the network structure is inhomogeneous.

For transport networks in real space not only the topological properties that are fully described by the adjacency matrix, are important, but also spatial (metric) properties like spatial distances of adjacent nodes. If particles do not interact, distances between nodes determine travel times of particles. For interacting particles the spatial properties of networks become even more relevant, since interactions usually depend on particle distances. Active transport of particles on a spatial square network embedded in a diffusive environment was investigated in [53]. In this model, particles are allowed to diffuse freely between

[17] In fact driven lattice gases also represent networks where nodes, i.e. sites have exactly one out- and in-going link to one site respectively.

[18] The outflow term cancels since it is exactly $\rho_i(t)$.

meshes, but can also attach to the active transport tracks that constitute the network and perform directed movement along them. Investigation of dynamical properties revealed that movement is directed on short time scales, while it is diffusive on larger time scales though with enhanced diffusion constant compared to pure diffusion. A corresponding network with steric interactions, but particles restricted to tracks, was studied in [15] (CS-model), modeling city traffic. In contrast to another model for street networks [6], there the spatio-temporal distances are taken into account, while street intersections act as nodes and the streets itself connect these nodes. The authors applied single track dynamics for parts between intersections basing on the NaSch-model [69]. At intersections, particles/cars interact, since two cars from different streets may not be on an intersection at the same time. In that work the interaction was mediated by traffic lights. For critical frequencies of traffic light switching the interaction at crossing can induce jamming queues that may lead to a large frozen particle/car cluster (gridlock).

We have seen in the last sections that intracellular transport on single filaments can be modelled by driven lattice gases. However usually the filaments, especially actin, form a rather irregular network structure. Since vesicles exhibit mutual steric interaction, we can expect effects like in the CS model. Therefore the phenomenology of transport on spatial inhomogeneous networks with steric interactions appears to be biologically relevant. Such systems will be investigated in chapter 4.

Chapter 3

Modeling of transport on inhomogeneous single filaments

Before complex transport networks are considered, we focus on active transport by molecular motors on single tracks. As argued in the last chapter, driven lattice gases can serve as simple models for active transport, yielding a number of collective phenomena known from empirical observations. The models considered here are in particular the TASEP (with and without LK) and the NOSC model, which is suited for distinct species of molecular motors. However, it will be shown that the main results are generic for a large class of driven lattice gases, hence yielding robust features that are believed to be encountered also in real systems. While the corresponding homogeneous systems (also called *pure*) are extensively studied and analytical results are abundant (at least for the TASEP/-LK), there are many open questions for their inhomogeneous counterparts. One example of inhomogeneity are varying codons on mRNA whose corresponding tRNA concentrations hence vary, resulting in different dwell times of ribosomes. A special feature arises in intracellular transport of motor proteins, where the presence of macromolecules on filaments can impede the movement of motor proteins (see Sec. 2.1.4 and [93, 22, 88]): Assuming that there is no binding preference of these molecules, one can suppose that these defects are *randomly distributed* along filaments. Hence statistical properties of defect ensembles appear to be relevant.

In this chapter a framework is developed that helps to find approximations for the transport capacity and phase diagrams in driven lattice gases with *binary site-wise disorder*, i.e. systems that contain fast (non-defect) and slow (defect) sites with the two transition rates p and $q < p$ respectively. The slow sites correspond to binding sites on filaments that are e.g. covered by a single species of MAP or they can be crosslinks with other filaments where other motors/vesicles can cross. In gene translation a codon species with significantly lowered tRNA abundance, can also act as a defect [1]. The central motif of this chapter is the

[1] In gene translation, there are usually more than one species of defects due to the high number of different codons. However, if one species of codons is much slower than others, the assumption of binary disorder also applies.

observation that the transport capacity in the disordered TASEP appears to be mainly determined by the longest *bottleneck*. A bottleneck is meant as a stretch of consecutive defects. This idea leads to the *single bottleneck approximation (SBA)* which will be developed in Sec. 3.2. In order to get access to analytical quantitative results in Sec. 3.1 an analytical approach for a computation of the transport capacity in the TASEP with a single bottleneck is elaborated. As a first step towards many-defect systems the influence of a second bottleneck in the system is analyzed numerically. Finally, in Sec. 3.3 a local minimum principle is derived which, together with a local generalization of the SBA, yields transport capacities and phase diagram structures of disordered driven lattice gases with Langmuir kinetics that mimic the behavior of vesicle transport on single inhomogeneous filaments.

The results of this chapter are published in [38] (Sec. 3.1), [39] (Sec. 3.2) and [40] (Sec. 3.3).

3.1 Phase diagram and edge effects of the TASEP with a single bottleneck

As was shown in some previous works [96, 61], the longest stretch of consecutive defect sites plays a crucial role for critical dynamics of the disordered TASEP. Since these stretches of defects appear to be the most relevant units for our considerations, they are treated individually, denoting them as *bottlenecks*. Hence a bottleneck of length l is a consecutive stretch of l defects. In this section an (semi-) analytical approach to determine properties of the TASEP with a single bottleneck will be derived. The main quantity of interest will be the *transport capacity* which is defined as the maximum current that can be achieved by tuning boundary rates. The model not only serves as a building block of the subsequent disorder theory, but has biological relevance itself: It was observed that clusters of slow codons, that correspond to bottlenecks, are quite abundant on mRNA [77, 52].

The present investigation generalizes previous works on the TASEP with defects in several aspects. Especially the dependence of the current on the length l of the bottleneck and its position is systematically studied. Previous works already have studied defect distributions of finite length. Chou et al. [12] have developed a method to find the current in the TASEP with a single bottleneck of length l, by an exact solution of a finite segment of length $l' > l$ that contains the bottleneck. The method corresponds to the search of an eigenvector of a $2^{l'} \times 2^{l'}$-matrix. For larger bottlenecks the computational effort may be extremely high. In order to treat larger bottlenecks, a method that is faster in computation is needed. For this purpose an analytical approach to calculate the current and critical boundary rates is developed, called the *interacting subsystem approximation (ISA)*. This approach leads to the problem of finding a specific root, constrained by physical requirements, of a polynomial which has a degree of order $l+1$ and can be computed analytically (up to $l = 3$) or numerically quickly for higher degrees. ISA also allows us to treat the effect of bottlenecks near the boundaries (*edge effect*, observed by Dong et al. [19]) for defects *near the boundaries* analytically and generalize it to longer bottlenecks. This has its biological counterpart in the observation that slow codons are often

found at or near the initiation site of translation on mRNA [95, 28].

Providing a first step towards systems with many bottlenecks/defects, a system exhibiting two bottlenecks of varying lengths and separation, generalizing the corresponding results of [19] for two single defects, is studied numerically. Therefore also the case that one of the bottlenecks is near the boundaries is investigated. The results will motivate a concept of *effective boundary rates* that encompasses the effect of boundary-near bottlenecks. The results for single bottlenecks and bottleneck-bottleneck interactions will provide the basis for an extensive study of finite defect densities, i.e. a macroscopic number of slow bonds which will be developed in the subsequent section. Here previous investigations for periodic [97, 96, 61] and open systems [42, 57, 24, 63, 50, 29] have revealed surprising results. For the open system, for example, it has been found that the position of the phase transitions is sensitively sample-dependent even for large systems [24].

3.1.1 The interacting subsystem approximation

We consider a TASEP consisting of L sites which can either be empty or occupied by one particle (see Sec. 2.3.1). Throughout this section we are mainly interested in the stationary state in the limit $L \to \infty$. The hopping rates at given sites j can take two values $p_j = 1$ on non-defect sites and $p_j = q < 1$ on defect sites. One also refers to defect *bonds* $(j, j+1)$ associated with hopping rates $p_{j,j+1} := p_j$ which is sometimes more appropriate, since hopping events consider both neighboring sites. Open boundary conditions are applied, so at the boundary sites $j = 1$ and $j = L$ particles can be inserted and removed, with entry rate α and exit rate β respectively. We use random-sequential update corresponding to continuous-time dynamics.

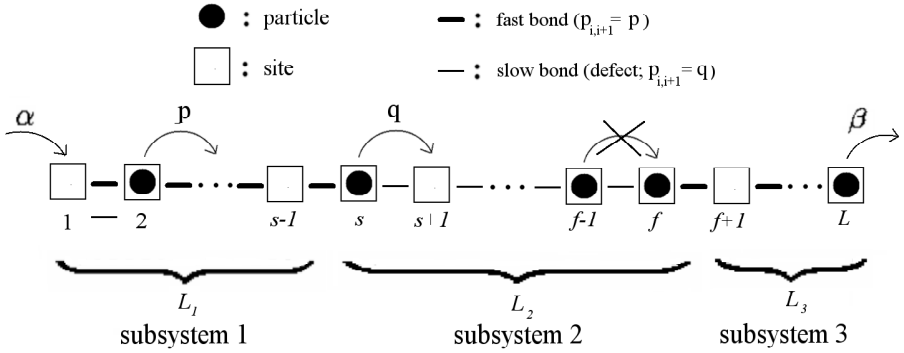

Figure 3.1: Illustration of the TASEP with a bottleneck of length l. The defect bonds/sites are characterized by a hopping rate $q < 1$, whereas at non-defect bonds/sites, the hopping rate is $p = 1$. The system is virtually divided into three subsystems with virtual entry/exit rates corresponding to the mean occupation/vacancy on the adjacent sites.

In this section the effect of a single bottleneck of length l with hopping rate $p_j = q$ (Fig. 3.1) is studied. All other sites are fast sites with hopping rate $p_j = 1$.

In order to determine relevant quantities like the current and critical boundary rates, the problem is approached by virtually dividing the system into three interacting subsystems (Fig. 3.1): A system of L_1 sites with hopping rate $p_j = 1$ at the left end of the chain, a section of length $L_2 = l + 1$ containing the bottleneck with l slow sites (hopping rate q) extending from site $s = L_1 + 1$ to site $L_1 + l = L_1 + L_2 - 1$ plus an extra fast site $f = L_1 + L_2$ at the right end, and finally another homogeneous system of length L_3 with hopping rates $p_j = 1$. Note that subsystem 2, which contains the bottleneck, starts and ends with a fast bond. This symmetry of the subsystem will be more convenient for our investigations.

The main idea of the approach is to use the exact solution for the stationary state of the homogeneous TASEP with random-sequential dynamics [17, 86]. This solution applies to all three pure subsystems as defined above. The interactions between these subsystems are described by suitably chosen boundary rates. We neglect correlations at the sites connecting the subsystems. Denoting the occupation number $\tau_j = 0, 1$ of site j, this explicitly means that we assume

$$\langle \tau_j (1 - \tau_{j+1}) \rangle \approx \rho_j (1 - \rho_{j+1}) \qquad \text{for } j = s - 1, f \tag{3.1}$$

where $\rho_j := \langle \tau_j \rangle$ is the average local density at site j. This approach is similar in spirit to that of Kolomeisky [56] for the case of a single defect ($l = 1$). In that work the two parts of the system left and right of the defect were treated individually in the continuum limit; both subsystems can adopt the phases of the homogeneous TASEP. Here the phases of the subsystem are denoted by lower case letters: low density (l), high density (h), and maximum current (m). In contrast to [56] where correlations on the slow bond are neglected, here the bottleneck will also be treated as a pure system (of reduced hopping rate) so that the most relevant correlations induced by it are taken into account. The three subsystems L_i are coupled by virtual boundary rates α_i, β_i. Note that all these rates are associated with fast bonds. In the following this approach will be called *interacting subsystem approximation (ISA)* to distinguish it from the usual mean-field approach which neglects *all* correlations.

The rate equations at the sites connecting the subsystems are then given by

$$\frac{d}{dt}\langle \tau_{s-1} \rangle = \langle \tau_{s-2}(1 - \tau_{s-1}) \rangle - \beta_1 \langle \tau_{s-1} \rangle \,, \tag{3.2}$$

$$\frac{d}{dt}\langle \tau_s \rangle = \alpha_2 (1 - \langle \tau_s \rangle) - q \langle \tau_s (1 - \tau_{s+1}) \rangle \,, \tag{3.3}$$

and

$$\frac{d}{dt}\langle \tau_f \rangle = q \langle \tau_{f-1}(1 - \tau_f) \rangle - \beta_2 \langle \tau_f \rangle \,, \tag{3.4}$$

$$\frac{d}{dt}\langle \tau_{f+1} \rangle = \alpha_3 (1 - \langle \tau_{f+1} \rangle) - \langle \tau_{f+1}(1 - \tau_{f+2}) \rangle \,, \tag{3.5}$$

with the virtual boundary rates

$$\alpha_2 = \rho_{s-1} \,, \qquad \alpha_3 = \rho_f \,, \qquad \beta_1 = 1 - \rho_s \,, \qquad \beta_2 = 1 - \rho_{f+1} \,, \tag{3.6}$$

in terms of the average local density ρ_j. For completeness, we also define $\alpha_1 := \alpha$ and $\beta_3 := \beta$. Note that the mean-field factorization of expectation values only

applies to the sites at the boundaries of the subsystems. All correlations within the subsystems are taken into account.

By analytical continuation of the exact "partition function" of the TASEP (2.9), the singularity at $\alpha = \beta$ can be removed by taking the limit $\alpha \to \beta$ which yields

$$\mathcal{Z}(\alpha, L) := \lim_{\beta \to \alpha} \mathcal{Z}(\alpha, \beta, L) = \sum_{j=1}^{L} \frac{j(2L-1-j)!}{L!(L-j)!}(j+1)\left(\frac{1}{\alpha}\right)^j . \tag{3.7}$$

The corresponding results for the TASEP with hopping rate $p \neq 1$ can be obtained by rescaling the time step $\Delta t \to \Delta t/p$ corresponding to rescaled boundary rates $\alpha \to \alpha/p$, $\beta \to \beta/p$ (see also sec. 2.3.1). Thus the partition function in a homogeneous TASEP with hopping rate p is

$$\mathcal{Z}_p(\alpha, \beta, L) = \mathcal{Z}\left(\frac{\alpha}{p}, \frac{\beta}{p}, L\right) . \tag{3.8}$$

This result will be used in the following for different values of L, depending on the length of the subsystems.

For hopping rates $p \neq 1$ the exact form of the current can be extracted from (2.10) by inserting (3.8). However, the rescaling of the time step must be compensated if the original time interval Δt is used. Hence

$$J_p(\alpha, \beta, L) = p\frac{\mathcal{Z}(\alpha/p, \beta/p, L-1)}{\mathcal{Z}(\alpha/p, \beta/p, L)} \tag{3.9}$$

Conservation of current then yields the central equations of the ISA for $p = 1$, $q < 1$

$$J_0(\alpha_1, \beta_1, L_1) = J_q(\alpha_2, \beta_2, L_2) = J_0(\alpha_3, \beta_3, L_3) \tag{3.10}$$

which express the fact that the current in the stationary state is the same in all three interacting subsystems. Note that (3.8) and (2.10) were used to express the current in the bottleneck (subsystem 2) by the result J_0 for a homogeneous system.

Inserting (2.9),(2.10) and (3.9) in (3.10) one obtains a set of two algebraic equations with six variables. In principle one can solve these equations, if four of the variables are known or more equations are given that determine variables.

3.1.2 One bottleneck far from the boundaries

First the case where the bottleneck is *far from the boundaries* is studied. So we assume that L_1 and L_3 are large. From the latter condition it is expected that the topology of the phase diagram is the same as that of a system with a single defect ($l = 1$). We can therefore follow [56] and classify the phases by the phases of the pure subsystems 1 and 3 whose lengths are $\mathcal{O}(L)$. We denote the phases of the subsystems in analogy to the homogeneous TASEP but using lower case letters, i.e. low density phase l, high density phase h and maximum current phase m.

Though at first glance one could expect nine possible phases corresponding to all possible combinations of three phases l,h,m that can be realized in the

pure subsystems 1 and 3, it was argued in [56] that only the combinations l-l, h-h and h-l can exist. The l-l-phase corresponds to a global *low density phase (L)*, while h-h corresponds to a *high density phase (H)*. In both cases, only around the bottleneck there are local deviations from the density profile of the homogeneous system. In the h-l-phase, phase separation emerges which cannot be observed in the pure system. The current in the h-phase is independent of the entry rate, while in the l-phase it is independent of the exit rate. Thus in a phase separated h-l-phase, the current is independent of both boundary conditions and takes a maximum value (see below). Although it is sometimes called a *maximum current phase (M)* as in the homogeneous system, its properties differ from the maximum current phase in the homogeneous system not only by the occurrence of phase separation, but also by the absence of algebraic boundary layers. Therefore we prefer the terminology *bottleneck phase* (B) to emphasize that the current is limited by the bottleneck and not by bulk exclusion. Furthermore, the transition to this phase corresponds to a transition of subsystem 1 from l to h and vice versa respectively, which is accompanied by a discontinuity of the mean density $\langle\rho\rangle = L^{-1}\sum_j \rho_j$. According to this, it can be classified as a first order transition in contrast to the pure system where the transition to the maximum current phase is of second order.

Although the system with a bottleneck is not exactly invariant under the particle-hole symmetry operation (2.8), this transformation only changes the position of the bottleneck, but still leaves it far from the boundary. Thus the particle-hole transformation leaves the phases of the subsystems unchanged, since it only changes their sizes, but they stay $\mathcal{O}(L)$. Therefore, we can conclude that the phase diagram must be symmetric with respect to the line $\alpha = \beta$. This symmetry constraint yields that the transition line between high and low density phase must be at $\alpha = \beta$.

We now want to determine the critical entry rate α^* at the transition from the L-phase to the B-phase for fixed β in terms of the analytical ISA approach introduced in the last subsection. It corresponds to the transition of (the pure) subsystem 1 from low to high density phase which occurs at $\alpha_1 = \beta_1 =: \alpha^*$. Furthermore we know that at this point $J = \alpha_1(1-\alpha_1)$. Subsystem 3 still remains in the low density phase. Therefore we also have $J = \alpha_3(1-\alpha_3)$. Since the current must be the same as in subsystem 1 and α_3 must be smaller than $1/2$, we conclude $\alpha_3 = \alpha^*$. From the definition of the virtual boundary rates (3.2), (3.6) one obtains by a simple transformation

$$\beta_2 = J/\rho_f = J/\alpha^* = 1-\alpha^*\,, \tag{3.11}$$

$$\alpha_2 = J/(1-\rho_s) = J/\beta_1 = J/\alpha^* = 1-\alpha^*\,, \tag{3.12}$$

where the first equality in each equation can be found e.g. in [17]. From the exact solution of the pure TASEP (2.10), (2.9) and the conservation of current (3.10), it follows

$$\begin{aligned} & J_q\,(1-\alpha^*, 1-\alpha^*, l+1) = \alpha^*(1-\alpha^*) \\ \Longleftrightarrow \qquad & \alpha^*(1-\alpha^*)\mathcal{Z}((1-\alpha^*)/q, l+1) = q\,\mathcal{Z}((1-\alpha^*)/q, l)\,, \end{aligned} \tag{3.13}$$

where $\mathcal{Z}(1-\alpha, l+1)$ is the limit defined in (3.7) and $\mathcal{Z}(1-\alpha, l+1) \neq 0$ for $0 \leq \alpha \leq 1$.

Eq. (3.13) is essentially a polynomial in $1/\alpha^*$ (or α^*, respectively) and can be solved numerically (or analytically for small values of l). The requirement

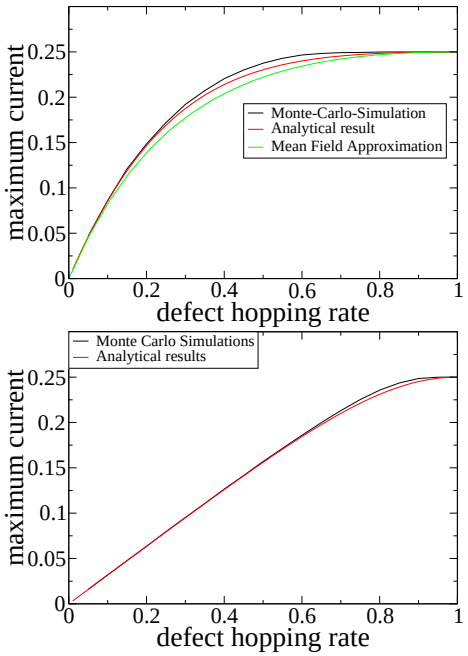

Figure 3.2: Maximum current (transport capacity) in a system with a bottleneck far from the boundaries in dependence on the slow hopping rate q. It is determined by Monte Carlo simulations for $\alpha = \beta = 0.5$ and by solving the ISA equation (3.13) for a bottleneck of length $l = 1$ (top) and $l = 6$ (bottom). For comparison the mean-field approximation $J^*_{\mathrm{MF}} = \frac{q}{(1+q)^2}$ [56] for $l = 1$ is included.

that a physical relevant solution for α^* has to be in the interval $[0, \frac{1}{2}]$ gives a unique solution $\alpha^*(q, l)$ for the transition point to the B-phase. In general, the solution depends on the length l of the bottleneck and the slow hopping rate q. For $l = 1$, for example, equation (3.7) can be inserted in (3.13) and transformed into

$$2{\alpha^*}^2 - (2 + 3q)\alpha^* + 2q = 0\,. \tag{3.14}$$

Hence, the relevant solution is

$$\alpha^*(l^* = 1) = \frac{2 + 3q}{4} - \sqrt{\frac{(2 + 3q)^2}{16} - q}\,. \tag{3.15}$$

Explicitly, for the value $q = 0.6$ used in most simulations, one obtains $a^* = \frac{2}{5}$ by evaluating (3.15).

The current at the transition point corresponds to the maximum current J^* in the B-phase which can be interpreted as the transport capacity of the system. From (3.13) we can see that

$$J^*(q, l) = \alpha^*(q, l)(1 - \alpha^*(q, l))\,, \tag{3.16}$$

which yields $J^*(0.6, 1) = \frac{6}{25} = 0.24$ for $q = 0.6$ taking the solution (3.15).

In Fig. 3.2 the dependence of $J^*(q, l)$ on the slow hopping rate q (for fixed l) was plotted, obtained by (3.16) and these analytical ISA-results were compared with results from Monte Carlo (MC) simulations for different bottleneck

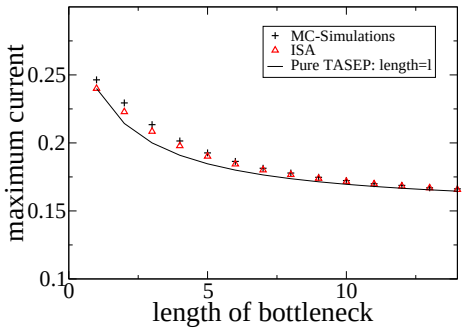

Figure 3.3: Maximum current in dependence on the bottleneck size for $q = 0.6$. Monte Carlo simulations are compared with ISA results. The solid line is the current in a homogeneous TASEP with $L = l + 1$, $\alpha = \beta = 1$ and hopping rate $q = 0.6$.

lengths. For a single defect site ($l = 1$) the analytical results obtained by (3.15) and (3.16) were compared with the results obtained by pure mean-field approximation $J^*_{\mathrm{MF}} = \frac{q}{(1+q)^2}$ [56]. Obviously also for $l = 1$ the results obtained by (3.16) are more accurate than mean-field results, while for longer bottlenecks, to our knowledge, no proper mean-field approximations are known. Note that our approximation takes into account correlations on the slow bonds, only correlations on sites adjacent to the bottleneck are neglected.

Fig. 3.3 shows the maximum current in dependence on the bottleneck length l. Here MC-simulations are compared with the results obtained by (3.16). The ISA results systematically underestimate the real current. The deviation is maximal for small l, but it does not exceed 3%. For larger bottlenecks, the agreement improves. We also note that $q = 0.6$ was chosen, since for this value the observed deviations have been found to be largest. In addition the exact current of a small homogeneous TASEP with system size $L = l + 1$ and $\alpha = \beta = 1$ was plotted. It seems that the asymptotics of the current in a finite pure system for large l are the same as for the bottleneck.

In Fig. 3.4, top, the dependence of the mean density $\langle\rho\rangle = \frac{1}{L}\sum_{i=1}^{L}\rho_i$ and the current J on the entry rate α is plotted for fixed β. In order to compute these quantities, the method introduced in [24] was used that allows to calculate the current and densities for an arbitrary set of values of α in one simulation. One observes a steep increase of the mean density for the same value of α where the maximum current plateau begins. This seems to coincide with the value of α^* obtained by ISA quite well. The slope increases with system size indicating a discontinuity in the thermodynamic limit corresponding to a first order phase transition, in contrast to the transition to the M-phase in the pure TASEP. The plots also show that at the transition point and in the whole B-phase, the current is maximal.

As was argued above, the phase diagram must be symmetric with respect to the diagonal $\alpha = \beta$ which yields $\beta^* = \alpha^*$. With this information the phase diagram of the TASEP with one bottleneck far from the boundaries can be sketched as displayed in Fig. 3.4, right. Its topology is the same as the one for a single defect far from the boundaries [56], while longer bottlenecks have a

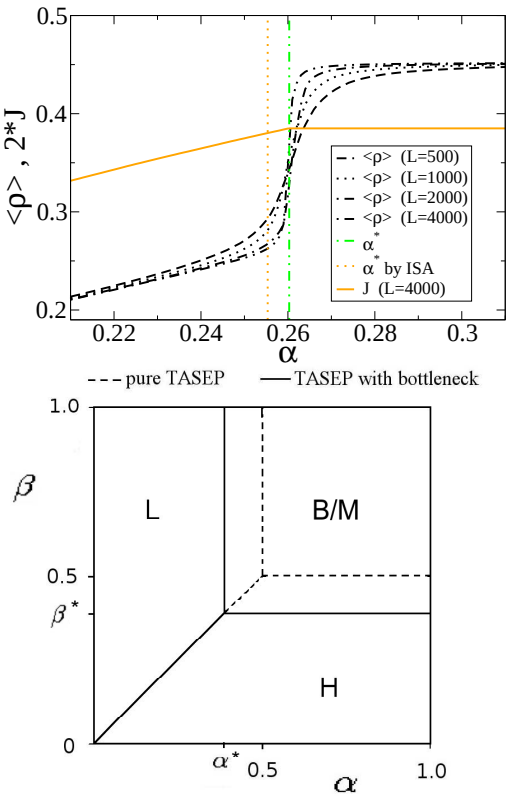

Figure 3.4: Top: Mean density $\langle\rho\rangle$ and current J as function of α. The slope of $\langle\rho\rangle(\alpha)$ becomes steeper for larger systems indicating a discontinuity in the thermodynamic limit. The vertical lines show the steepest point of $\langle\rho\rangle(\alpha)$ identified as the phase transition α^* compared with the ISA results from (3.13).
Bottom: Schematic phase diagram of the TASEP with one bottleneck far from the boundaries. It looks similar to the phase diagram of the pure TASEP while the transition lines to the maximum current (bottleneck-) phase is shifted to be at α^* and β^*. The mean density is discontinuous at these points.

larger B-phase than single defects. It looks similar to the phase diagram of the pure TASEP but here all phase transitions are of first order in contrast to the TASEP, and the characteristics of the M-phase and B-phase are different.

Another procedure to compute the transport capacity for a finite bottleneck is the *finite segment mean-field theory (FSMFT)* introduced in [12]. In this approach, a segment of l' sites including the bottleneck of length $l < l'$ is considered. Currents can then be obtained from the eigenvector of the zero-eigenvalue of the $2^{l'} \times 2^{l'}$-transition matrix of this segment [12]. The advantage of this method is that the accuracy can be systematically increased by expanding the size l' of the segment. It can also treat arbitrary combinations of hopping rates inside the segment. However, due to the exponentially increasing size of the transition matrix one is currently restricted to small segment lengths. In contrast, the ISA-method, though not asymptotically exact, relies on finding *one specific* root of a polynomial equation of a maximal degree $l + 2$. This makes it possible to compute the transport capacity for systems with large bottlenecks

of several hundred sites rather easily. This advantage becomes relevant for disordered systems with finite defect site density where bottlenecks of arbitrary length can occur. For example the computation of the maximum current of a system with 500 consecutive defect sites can be made in less than one second on a standard[2] PC to obtain $J^*_{\mathrm{ISA}}(l = 500) = 0.15045$ for $q = 0.6$. Although this agrees nicely with the value from MC simulations, $J^*_{\mathrm{MC}} = 0.15049$, it is clearly different from the asymptotic value $J^*_\infty = q/4 = 0.15$ for $l \to \infty$ [61, 97, 12].

3.1.3 Edge effects: One bottleneck near a boundary

Next we consider a system with a bottleneck near the left boundary, i.e. now both $L_1 = s - 1$ and $L_2 = l + 1$ are of order $\mathcal{O}(1)$ for $L \to \infty$. The case of a bottleneck at distance d from the right boundary, i.e. the last slow site is at site $L - d - 1$, has not to be considered separately since the results can be deduced using the particle hole-symmetry operation that also exchanges subsystem 1 and 3. Since there is only one macroscopic subsystem, namely subsystem 3, the classification of phases is slightly different than in Sec. 3.1.2. Now the phase of the system with bottleneck is basically identically to that of subsystem 3. Phase separation can no longer occur since the size of subsystem 1 is microscopic. The entry rate α_3 of subsystem 3, defined in ISA (see (3.2)-(3.5)), can thus be treated as an *effective entry rate* $\alpha_{\mathrm{eff}} := \alpha_3 \neq \alpha$ for the *bulk* of the system which is a homogeneous TASEP. The phase of the full system corresponds to the phase of subsystem 3 which are denoted by L', H' or M.

For $L_1 \geq 2$, the system can be divided into three subsystems in the same manner as in Fig. 3.1 . First we consider a system in the low-density phase L'. Hence the current is given by

$$J = \alpha_{\mathrm{eff}}(1 - \alpha_{\mathrm{eff}})\,. \tag{3.17}$$

In the steady state the entry and exit rates of a pure TASEP with L sites are $\alpha = \frac{J}{1-\rho_1}$ and $\beta = \frac{J}{\rho_L}$ [17]. The currents in subsystems 1 and 2 have to be identical and thus, as in (3.10),

$$J_0(\alpha, 1 - \rho_s, L_1) \quad = \quad J_q\left(\frac{J}{(1-\rho_s)}, \frac{J}{\rho_f}, L_2\right)\,, \tag{3.18}$$

where J_0 and J_p are the exact currents in a pure system given by (2.10) and (3.9), while ρ_s and ρ_f are defined in the same manner as in Sec. 3.1.2. Since subsystem 3 is assumed to be in the low density phase, the density profile is flat at its left end, i.e. the density is independent of the position if ISA is applied. Hence we have $\alpha_{\mathrm{eff}} = \rho_f = \rho_{f+1}$ and can take $J = \rho_f(1 - \rho_f)$ in Eq. (3.18). Furthermore the currents in subsystem 1 and subsystem 3 have to be the same which leads to

$$J_0(\alpha, 1 - \rho_s, L_1) = \rho_f(1 - \rho_f)\,. \tag{3.19}$$

Now we have two ISA-equations, (3.18) and (3.19), as well as the two variables ρ_s and $\rho_f = \alpha_{\mathrm{eff}}$. For given α, L_1 and bottleneck length l these equations can be solved to obtain the effective entry rate α_{eff}, while the resulting current can be obtained from (3.17).

[2] AMD Athlon 3000 MHz (2007)

For $s = 2$, i.e. $L_1 = 1$ that procedure does not work in the same way because the current in a system of size $L = 1$ is not defined as one can see in (2.10). But even in this case, we still have $\alpha = J/(1 - \rho_1)$ which is valid by definition of the boundary rates. After inserting $J = \rho_f(1 - \rho_f)$, this equation together with (3.19) again gives a solvable set of two equations with the two variables ρ_s and ρ_f.

For $s = 1$ ($L_1 = 0$) subsystem 1 does not exist and we have only the two subsystems 2 and 3. Subsystem 2 comprises the sites $\{1, \ldots, L_2\}$ and subsystem 3 $\{L_2 + 1, \ldots, L\}$ which includes the bulk of the system. This problem can however be solved, by inserting

$$\alpha_2 = \alpha\,, \qquad \beta_2 = \frac{J}{1 - \rho_f}\,, \qquad \alpha_3 = \rho_f\,. \tag{3.20}$$

Analogous to (3.10) we hence obtain the equation

$$J_q\left(\alpha, \frac{J}{(1 - \rho_f)}, L_2\right) = \rho_f(1 - \rho_f)\,, \tag{3.21}$$

with $J = \rho_f(1 - \rho_f)$. This equation can be solved for the variable $\rho_f = \alpha_{\text{eff}}$ thus we obtain the effective entry rate and by (3.17) the corresponding current.

Because of the particle-hole symmetry (2.8) these results can be transferred for β_{eff} in the high-density phase. The effective exit rate for the bulk β_{eff} can then be determined using (3.17)-(3.21). Note that in the low-density phase, β has no influence on the bulk of the system, only in a small region near the boundaries. The same is valid in a high-density phase for α.

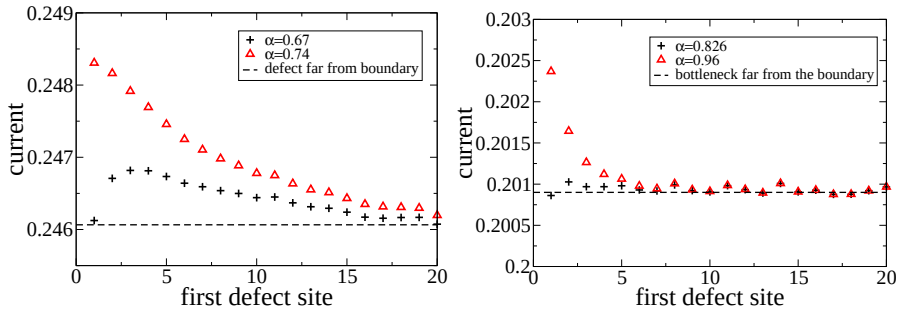

Figure 3.5: Current in a system with a single defect site (left) and a bottleneck of length $l = 4$ (right) near the left boundary in dependence on its position, for high entry rates. The exit rate is $\beta = 1.0$. The system size is $L = 500$ while the number of iterations is 40000000, $q = 0.6$. The entry rates have been chosen in order to optimally display the mixed and the positive edge effect. In the system with the longer bottleneck (right), the mixed edge effect is almost not visible even for optimized parameters. Note that the magnitude is much smaller than in Fig. 3.6.

Edge effect: discussion

In Fig. 3.5 and 3.6 the current is plotted in dependence on the position of the first defect site for different values of α while $\beta = 1$. One observes that

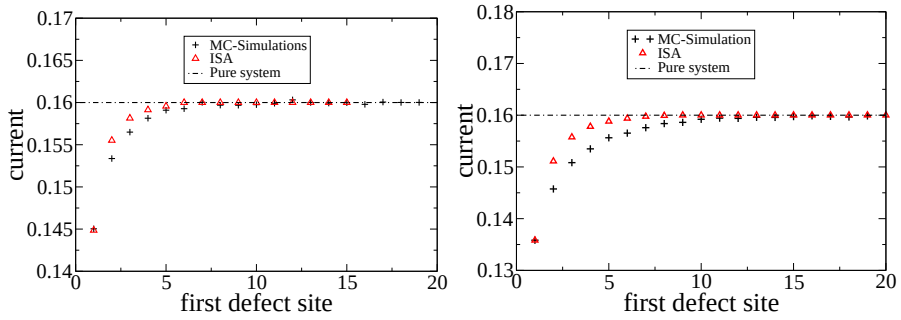

Figure 3.6: Current in a system with a bottleneck near the boundaries in dependence on the position of the first defect site, for low entry rates. The exit rate is $\beta = 1 - \alpha$, system size $L = 500$ and number of time steps $= 2000000$ for bottleneck length $l = 1$, $q = 0.6$, and $\alpha = 0.2$ (left), bottleneck length $l = 4$, $q = 0.6$ and $\alpha = 0.2$ (right). The scale for the current has been chosen in order to emphasize the form of the deviations.

the position of the bottleneck has a significant influence on the current. This is called the *edge effect*, first observed in [19]. In that work only an increase of the current was observed if defects approach the boundary (*positive edge effect*) which can be seen in Fig. 3.5. In addition, ISA predicts a decrease of the current for low entry rates. This *negative edge effect* is confirmed by computer simulations (Fig. 3.6). There is also a region of entry rates, where the dependence of the current on the bottleneck position is non-monotonic (*mixed edge effect*, see Fig. 3.5)! Simulations for different system sizes indicate that this non-monotonic behavior is not a finite-size effect. Nonetheless, as we can also see in the figures, the magnitude of the positive and the mixed edge effect is much smaller than the one of the negative edge effect. The ISA results obtained from the equations in the last subsection confirm the existence of negative and positive edge effect, while the mixed one is not. This indicates that the mixed edge effect is caused by correlations at the edge of the bottleneck. In Fig. 3.6 the analytical results are plotted for comparison. They are not displayed in Fig. 3.5 since the deviations due to correlations are larger than the positive/mixed edge effect itself. In appendix A it is shown that the negative edge effect is predominant in regimes where the current depends significantly on the boundary rates.

Moreover, we see that the current does not attain a plateau value. Instead it seems to approach asymptotically the value $J = 0.25$ (Fig. 3.7). This is confirmed by simulations, where the current is calculated for the very high value $\alpha = 100$ that yields an effective entry rate of $\alpha_{\text{eff}} \approx 0.5$. As was argued above, there is no macroscopic phase separation, either, if the distance of the bottleneck from the boundary is microscopic, so we can state that for a bottleneck near the boundary only the high and low density phase can occur.

Though strictly speaking there is no B-phase if the bottleneck is near a boundary, the system still exhibits a kind of *crossover*. While there is neither a plateau region nor a sharp kink in the dependence of the current on the entry rate (see Fig. 3.7), for higher entry rates this dependence is rather weak. For a bottleneck far from the boundaries we actually have sharp phase transitions,

so we can say that by approaching the bottleneck to the boundary, the phase transition to the B-phase is "softened" into a crossover.

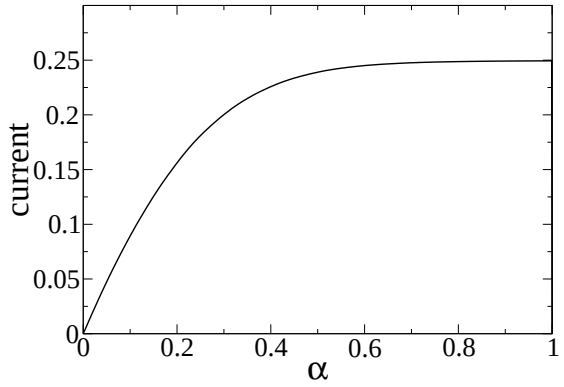

Figure 3.7: Current in dependence on the entry rate α for $\beta = 1$ and a defect at site $j = 3$. Results are obtained by MC simulations. There is no plateau.

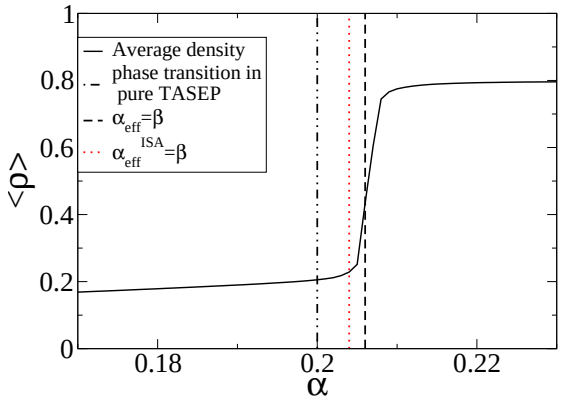

Figure 3.8: Average density in dependence on the entry rate for $\beta = 0.2$ and a defect at site 3. The transition to the high density phase is shifted to larger α compared to the pure system.

The transition from low density phase to the high density phase occurs for $\beta = \alpha_{\text{eff}}$. This is confirmed in Fig. 3.8 where the average density is plotted in dependence on α. The jump in the average density marks the transition point, which matches quite good the value of α_{eff}. One observes that the transition point is shifted to higher values of α compared to the transition in the pure system $\alpha = \beta$. In this diagram, α_{eff} was obtained by the formula $\alpha_{\text{eff}} = \frac{J}{1-\rho_{f+1}}$. The value calculated by solving the ISA equations (3.18) and (3.19) is a little less, but it still yields the correct sign of the shift of the transition point.

Fig. 3.9 shows the dependence of α_{eff} on α. Since $\beta = \alpha_{\text{eff}}$ is the transition line between high and low density phase, the diagram simultaneously displays

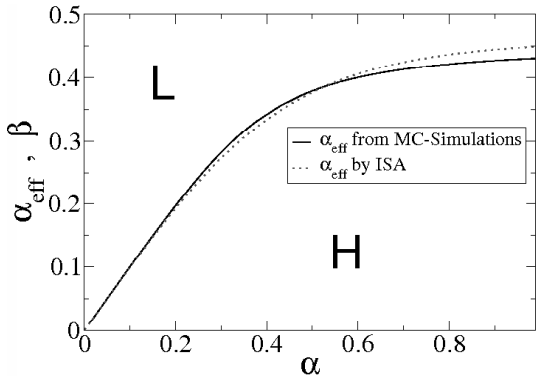

Figure 3.9: Effective entry rate in dependence on α. Interpreting the y-axis as the beta range, this corresponds to the phase diagram with the graph being the transition line between H-phase (below) and L-phase (above).

the phase diagram, interpreting the y-axis as the β-range. As we see, the phase transition line calculated in ISA is in good agreement with numerical results.

3.1.4 Two bottlenecks

The next step towards disordered systems is the investigation of a system with two bottlenecks. This will tell us something about the importance of "interactions" between the bottlenecks. We distinguish two cases: First we consider situations where both bottlenecks are in the bulk of the system, i.e. far away from the boundaries. Then edge effects are studied in more detail by allowing one bottleneck to be close to one of the boundaries. Unfortunately, the analytic ISA approach cannot be used for generic bottleneck lengths since the equations would be underdetermined. In fact, Foulaadvand et al. have applied ISA for two single defects with a spacing in between [30]. However, for longer bottlenecks, we have to rely on simulation results.

Two bottlenecks far from the boundaries

Systems with two bottlenecks of length l_1 and l_2 were simulated, with d fast sites in between. We focus on the maximum current phase and determine the current $J^*(l_1, l_2)$. In Fig. 3.10, $J^*(l_1, l_2)$ is plotted as function of the distance d between the bottlenecks for different values of l_1 and l_2. One observes that if the lengths of the two bottlenecks differ with $l_1 > l_2$, $J^*(l_1, l_2)$ tends to converge to $J^*(l_1)$, which is the value obtained in a system with only the longer bottleneck. The convergence is faster for a larger difference $l_1 - l_2$ of the bottleneck lengths. In this case for a distance of about 5-10 lattice sites, the maximum current is almost the same as for a system with only the longer of the two bottlenecks. Of course for $d \to 0$ the bottlenecks merge, thus we have only one bottleneck and $J_2^*(l_1, l_2, 0) = J^*(l_1 + l_2)$. If both bottlenecks have equal size, $d \to \infty$ converges to the maximum current of a single bottleneck which generalizes results of [19] to the case $l_1 = l_2 > 1$. In general, one can say that $J^* \approx J^*(\max[l_1, l_2])$, if the

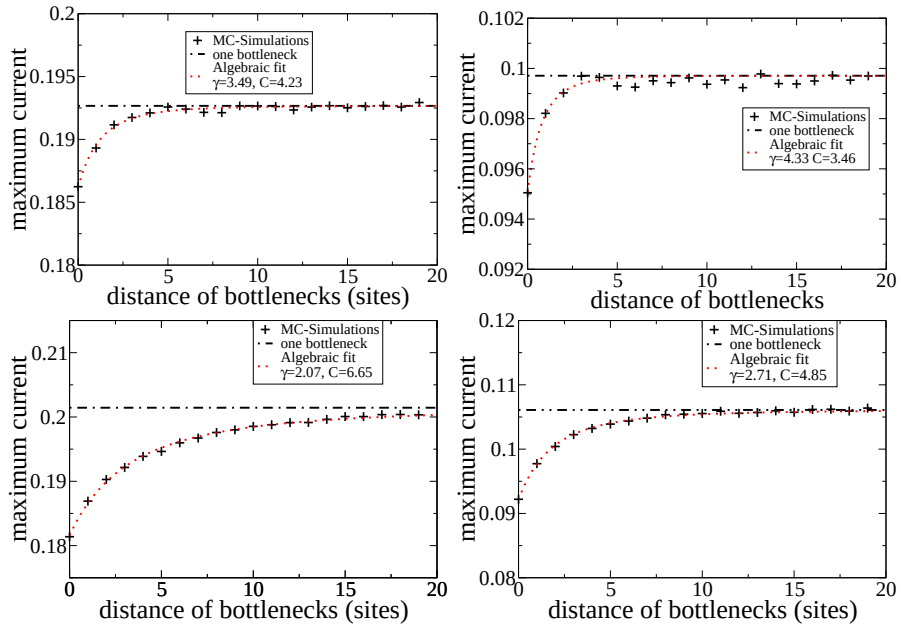

Figure 3.10: Maximum current (transport capacity) in a system with two bottlenecks of length l_1 (the first one) and l_2 (the second one) far from the boundaries in dependence on the distance of the two bottlenecks. The current is determined by MC simulations for $\alpha = \beta = 0.5$. In each graph an algebraic fit of the form $f(d) = J^*(l_1) - (d+C)^{-\gamma}$ with fit parameters C and γ is included. $J^*(l_1)$ is obtained from the MC simulations in Sec. 3.1.2. One observes that the maximum current converges to the maximum current of a system with a single bottleneck, i.e. the longer one. The parameters are $l_1 = 5$, $l_2 = 1$, $q = 0.6$ (top left), $l_1 = 5$, $l_2 = 1$, $q = 0.3$ (top right) $l_1 = 4$, $l_2 = 3$, $q = 0.6$ (bottom left), and $l_1 = 4$, $l_2 = 3$, $q = 0.3$ (bottom right).

bottlenecks are far from each other.

Two bottlenecks: Edge effects

Next a system with two bottlenecks was simulated where one is near the boundary and one is far away. We concentrate on the case, where the bulk bottleneck is larger than the one close to the boundary.

In Fig. 3.11, the dependence of the current on the distance of the first bottleneck is plotted. For comparison the results for a single bottleneck near the boundary from section 3.1.3 are included. One observes no significant difference between the two datasets. This observation indicates that *bottlenecks far from the boundary do not have any influence on the current*, as long as the current is below the maximum current allowed by that bottleneck.

In Fig. 3.12, however, we see the maximum current in a system with a bottleneck of length l far from the boundaries and a defect at site 3. Again, one does not see a significant difference: *a small bottleneck near the boundary has no influence on the transport capacity.*

In agreement with observations already made in [12], our results motivate the view of a local influence of bottlenecks that yields the possibility to generalize concepts of the TASEP with a single bottleneck to systems with many bottle-

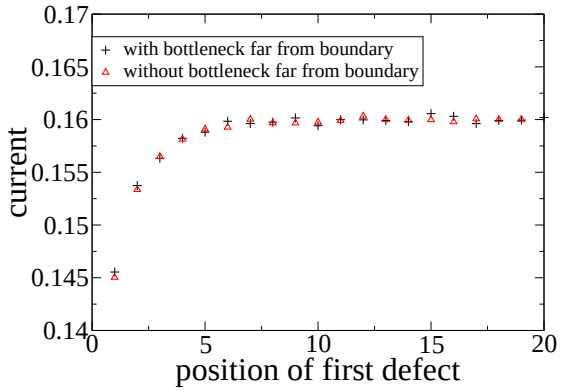

Figure 3.11: Dependence of the current on the position of the first defect for $\alpha = 0.2$ and $\beta = 1.0$. Comparison of a system with only one defect and a system with an additional bottleneck ($l = 5$) far from the boundaries.

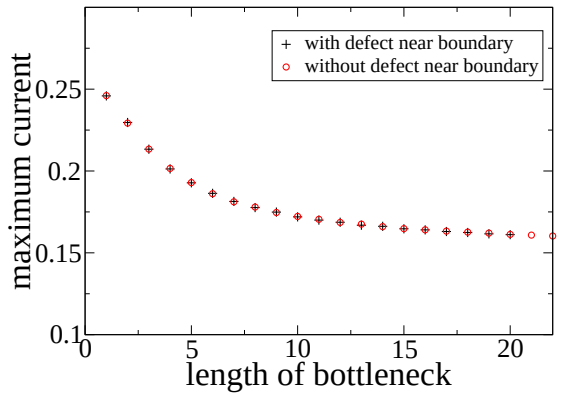

Figure 3.12: Maximum current in dependence on the bottleneck length for $q = 0.6$. The addition of a defect near the boundaries at site $d = 3$ does not alter the maximum current.

necks. Only bottlenecks near the boundaries have influence on the current if it is below the transport capacity. One can therefore propose that the influence of boundary defects can be taken into account by effective boundary rates in the same manner as for a single bottleneck near the boundaries. That means that below the maximum current the system can be described as a pure TASEP, but with effective boundary rates $\alpha_{\text{eff}}, \beta_{\text{eff}}$ depending on the configuration of bottlenecks near the boundaries instead of the pure ones.

We have seen that, except for small edge effects, the transport capacity is mainly determined by one bottleneck i.e. the longer one of the two, as long as bottlenecks are far from each other. In the following section this observation will be generalized to disordered driven lattice gases with many bottlenecks, in particular systems exhibiting random disorder. Therefore the analytical results of single bottleneck systems considered in this section can be used for the calculation of transport capacities in many-defect systems. In addition the concept of effective boundary rates will be generalized to disordered systems and refined by statistical methods.

3.2 Single bottleneck approximation for disordered driven lattice gases

In [61] it was conjectured that in randomly disordered systems (see Sec. 2.3.4) the maximum current depends on the individual configuration of defects and is mainly determined by the longest bottleneck. In the last section this was shown to be correct, at least for two bottlenecks which are not too close to each other. These observations lead to the *Single Bottleneck Approximation (SBA)* assuming that all but the longest bottleneck can be approximately neglected for determination of the transport capacity. This approximation will be supported in this section by numerical and analytical arguments.

For applications to real systems, macroscopic parameters and quantities are most relevant. Macroscopic quantities like the transport capacity can depend on the microscopic structure of the system which can differ for different defect samples. We are mainly interested in determining statistical properties, e.g. probability distributions and expectation values, of relevant quantities taking an ensemble of systems rather than looking at single samples. We therefor consider in this section a large ensemble of individual finite but large systems, while the individual values of these quantities might vary for different samples.

The objective of this section is to understand the phase diagrams of driven lattice gases and give quantitative approximations for the expectation values of critical parameter values and the transport capacity. We therefore check the validity of the conjectured SBA and the concept of effective boundary rates on individual samples not only in the disordered TASEP, but also in a more complex model with internal states (NOSC model without Langmuir kinetics [71, 36], see Sec. 2.3.2), which is a model for intracellular transport with KIF1A motor proteins. In the NOSC model there is no explicit hopping rate, but we allow inhomogeneity of the forward-rebinding rate ω_f, which marks a parameter controlling the average velocity of single particles. Like for the TASEP we allow fast rates ω_f^{fast} and slow rates ω_f^{slow} associated with the bonds/sites referring to sites with slow rates as defect sites. The transport capacity can be defined in

the same way as for the TASEP by $J^* = \max_{\alpha,\beta} J(\alpha, \beta)$, with the corresponding boundary rates (see 2.3.2).

With the help of extreme value statistics these principles will be used to derive approximations for expectation values of the transport capacity and critical values for phase transitions (Sec. 3.2.2). After checking the accuracy of the SBA, in Sec. 3.2.3 the relevance of various possible corrections is discussed, e.g. by edge effects or effective interactions between the bottlenecks. A perturbative expansion of the transport capacity is shown to yield a criterion for applicability of the SBA to various driven lattice gases, and simultaneously gives an approximation for effective boundary rates. Using the relation between effective and real boundary rates together with SBA helps to quantify the effect of disorder on the phase diagram, which is investigated in Sec. 3.2.4 in detail.

We consider *binary disorder* as introduced in Sec. 2.3.4. One system parameter determining the average speed of particles is assumed to be inhomogeneous with the two possible values p and $q < p$ that are randomly distributed with defect density ϕ by

$$p_j = \begin{cases} q & \text{with prob. } \phi \\ p & \text{with prob. } 1-\phi \end{cases} . \tag{3.22}$$

In the case of the TASEP, p is the hopping rate, while a distribution of this kind can also be exhibited by generic parameters controlling the speed of particles (e.g. the forward rebinding rate ω_f in the NOSC model). In the TASEP, the time scale Δt is chosen such that the hopping probability $p\Delta t = 1$.

For large system size, the investigation is usually simplified by performing a continuum limit. Since crucial properties, like the bottleneck lengths in a disordered system, might depend on the system size we have to specify this limit more carefully. We define a *weak continuum limit* where terms of $\mathcal{O}(1/L)$ are neglected while terms of $\mathcal{O}(1/\ln L)$ are kept, and a *strong continuum limit* where even terms of $\mathcal{O}(1/\ln L)$ are neglected. Here we are rather interested in "finite but large" systems by considering the weak continuum limit that retains some dependence on the system size. This is motivated by the facts that (a) the maximum current decreases with increasing bottleneck length and (b) the length of the longest bottleneck grows logarithmically in L [61]. Besides the macroscopic structure of the stationary state, like in the last section, we will mainly focus on the determination of transport capacity and phase transitions.

3.2.1 Single Bottleneck Approximation

The claim that the longest stretch of consecutive defects determines the transport capacity is plausible if one assumes a local character of the bottlenecks by characterizing them by an individual transport capacity $J_j^*(l)$ depending on the length l and (possibly) position j. In the stationary state the total current is constant in space and is restricted by all bottleneck capacities, i.e. it cannot exceed the minimum of all $J_j^*(l)$. Since the transport capacity is decreasing monotonically with bottleneck size as was shown in the last section, the minimum of $J_i^*(l)$ corresponds to the transport capacity $J^*(l^*)$ of the longest bottleneck which consists of l^* consecutive defects. Smaller bottlenecks do not contribute much as long as they are not too close to the longest one. This motivates the *Single Bottleneck Approximation (SBA)*:

> The transport capacity J^* of a disordered system is approximated by the one in a single bottleneck system, $J^*_{SBA}(l^*)$ with a bottleneck length l^* corresponding to the maximum length of bottlenecks in the disordered system, i.e. $J^* \approx J^*_{SBA}(\max_i[l_i])$.

Indeed experimental results on protein production rates in translation with slow codons support this assumption. It was shown that the protein production rate is significantly lower if slow codons are clustered, forming long bottlenecks, than in the case that they are distributed separately [99].

The SBA reduces the problem of a many-defect system to the much simpler one of a single bottleneck in a system. In particular for the TASEP, we can rely on the analytical results obtained in the last section for single bottleneck systems.

One could conjecture that the SBA also works for generic driven lattice gases, especially for low defect density ϕ, where the average distance between defects is large and their interactions can be neglected. As an example it will be tested not only for the TASEP, but also for the disordered NOSC model in the limit of vanishing Langmuir kinetics. In both systems the average velocity of the particles is dependent on one or more transition rates. In the TASEP the hopping rate p is such a parameter, while in the NOSC model the forward-rebinding rate ω_f is a parameter controlling the average velocity.

First we consider a fixed realization of disorder with small defect density ϕ. In this case we have a system with dilute distributed bottlenecks of different lengths. The SBA will be tested for the disordered TASEP and the NOSC model. For this purpose, systems with different disorder samples were simulated and the results for the transport capacity J^* were compared with numerical and analytical results of systems with single bottlenecks in Tables 3.1 and 3.2. For each sample the longest bottleneck l^* was identified and the SBA transport capacity $J^*_{\mathrm{SBA}}(l^*)$ in a single-bottleneck system with just one bottleneck of size l^* was calculated. One observes a quite good agreement, although the SBA seems to overestimate the transport capacity systematically. This is not surprising since effective interactions of the bottlenecks lead to an additional decrease of the current. According to the results in the last section we expect that the main effect comes from bottlenecks near the longest one, leading to a reduction of the transport capacity compared to bottlenecks far from the longest one. To illustrate this effect, the distance of the nearest bottleneck was included in Table 3.1. Since it is more probable to find a bottleneck close to the longest one for larger defect density ϕ, the results tend to be less accurate with increasing ϕ.

Surprisingly it seems that the values $J^{*\mathrm{ISA}}_{\mathrm{SBA}}$ obtained by the semi-analytical ISA method are more accurate than the numerical ones ($J^{*\mathrm{MC}}_{\mathrm{SBA}}$) of the single-bottleneck system. This is because ISA usually underestimates the value of $J^*(l)$ in the TASEP with one bottleneck, while SBA overestimates the current. Hence errors cancel at least partially.

3.2.2 Probability distributions and expectation values in SBA

As we have seen, the transport capacity depends quite strongly on the particular sample of the defect distribution, i.e. the size of the longest bottleneck. Usually

L	ϕ	l^*	distance	length	J^*_{MC}	$J^{*\mathrm{MC}}_{\mathrm{SBA}}$	$J^{*\mathrm{ISA}}_{\mathrm{SBA}}$
1000	0.05	2	2	1	0.2174	0.2294	0.2229
1000	0.1	3	12	1	0.2080	0.2131	0.2080
1000	0.2	3	2	2	0.1963	0.2131	0.2080
3000	0.1	3	4	1	0.2048	0.2131	0.2084
3000	0.2	5	5	1	0.1866	0.1925	0.1901

Table 3.1: Comparison of Monte Carlo simulation results (MC) and SBA results for the transport capacity J^* in the disordered TASEP with different system sizes L and defect densities ϕ. The transport capacity J^*_{MC} was obtained by Monte Carlo simulations for $\alpha = \beta = 0.5$ (column 6) for fixed slow hopping rate $q = 0.6$. This is compared with MC results ($J^{*\mathrm{MC}}_{\mathrm{SBA}}$, column 7) and the results obtained by ISA, by applying SBA ($J^{*\mathrm{ISA}}_{\mathrm{SBA}}$, column 8) for a single-bottleneck system with one bottleneck in the bulk whose length is the same as the longest bottleneck in the simulated disordered TASEP (column 3). Columns 4 and 5 give the distance and length of the bottleneck next to the longest one.

L	ϕ	l^*	distance	length	J^*_{MC}	$J^{*\mathrm{MC}}_{\mathrm{SBA}}$
1000	0.05	2	4	1	0.07923	0.08179
1000	0.1	3	2	1	0.07451	0.07643
1000	0.2	6	3	1	0.06659	0.06717
3000	0.1	4	6	1	0.07205	0.07213
3000	0.2	6	3	1	0.06677	0.06717

Table 3.2: Same as in Table 3.1, but for the NOSC model without Langmuir kinetics (see Sec. 2.3.2). The forward hopping rate is inhomogeneous with $\omega_f^{\mathrm{fast}}\Delta t = 0.58$ and $\omega_f^{\mathrm{slow}}\Delta t = 0.32$. The other parameters are fixed: $\omega_h\Delta t = 0.8$, $\omega_s\Delta t = 0.22$, $\omega_b = 0$.

in real systems the exact distribution of defect sites is not known, particularly the size and position of the longest defect cannot be identified. Then a statistical treatment, i.e. considering an ensemble of systems with fixed defect density, but varying distributions of defects, is more appropriate. It allows to determine expectation values for quantities like currents and effective boundary rates (see Sec. 3.2.4). This is especially relevant for applications e.g. to intracellular transport. Each cell consists of a large number of filaments that serve as tracks for motor proteins, and often randomly distributed defects play an important role [51]. Therefore of interest are ensembles rather than the properties of individual filaments in this context.

In this section the expectation value of the transport capacity $J^*(q, \phi, L)$ will be approximated for fixed defect density ϕ and finite but large system size L. In the last subsection it was shown that for small ϕ the capacity depends approximately on the size of the longest defect. Therefore first the expectation value for the size of the longest bottleneck is determined in such a system.

We now consider a given sample with defect density ϕ and system size L. The k-th bottleneck has length l_k and in the following two consecutive fast sites $j, j+1$ will be interpreted as a bottleneck of length $l = 0$ located at site j. This implies that the number N_b of bottlenecks is equal to the number N_f of fast sites, since each bottleneck is followed by exactly one fast site [3]. The bottleneck length l is a random variable with distribution

$$P_\phi(l) = \phi^l(1-\phi)\,. \tag{3.23}$$

[3] We neglect the possible exception at the right boundary.

Since on average the fraction of fast sites is $(1-\phi)$, the mean number of fast sites is $\langle N_f \rangle = (1-\phi)L$. The length of the longest bottleneck is $l^* = \max\{l_k | k = 1, ..., N_f\}$. The statistics of the maximum of identically independently distributed random values is governed by extreme value statistics (see e.g. [91]). It says that for a continuous probability distribution $P(l)$ that decays exponentially or faster for $l \to \infty$, the probability density of l^* being the maximum value of N independently distributed random values is for large N asymptotically described by the *Gumbel distribution* [91]

$$G(u) = e^{-u} e^{-e^{-u}} \tag{3.24}$$

where $u = u(l^*)$ is a rescaled and shifted function of l^* depending on the details of the probability distribution $P(l)$.

However, since in our case the probability distribution is discrete we need to be careful. Therefore here, following the derivation used in [91] for continuous distributions, the probability distribution of the maximal bottleneck length is explicitly derived in order to control errors made by approximations. This will also provide an explicit expression for $u(l^*)$.

The probability of a bottleneck being shorter than l' is

$$P_<(l') \;=\; \sum_{l=0}^{l'-1} P_\phi(l) = 1 - \phi^{l'} \,. \tag{3.25}$$

Since the l_k are independently distributed, we have the probability that all l_k are smaller than l':

$$\begin{aligned} H_<(l') \;&:=\; P_<(l')^{N_f} = \exp\left(N_f \ln(1-\phi^{l'})\right) \\ &=\; \exp\left((1-\phi)L \ln(1-\phi^{l'}))\right) \,. \end{aligned} \tag{3.26}$$

For large L this probability is significantly larger than zero only for $\phi \ll 1$ and we can use the approximation $\ln(1-\phi^{l'}) \approx -\phi^{l'}$, thus

$$H_<(l') \approx \exp(-\phi^{l'}(1-\phi)L) \,. \tag{3.27}$$

As was shown in [91], the error of this correction is $\mathcal{O}(1/L^2)$ for exponential $P(l)$. Thus finite-size corrections can be neglected in the weak continuum limit.

The probability that *all* values are smaller than l' is equal to the probability that the maximum l^* is smaller than l',

$$H_<(l') = \sum_{l^*=0}^{l'-1} \mathcal{P}(l^*) \,. \tag{3.28}$$

$\mathcal{P}(l^*)$ is the probability that the longest bottleneck has length l^* which is explicitly given by

$$\mathcal{P}(l^*) \;=\; H_<(l^*+1) - H_<(l^*) \tag{3.29}$$

$$\begin{aligned} &=\; H'_<(l^* + \frac{1}{2}) + \mathcal{O}\left((\Delta l^*)^3\right) \\ &\approx\; -L(1-\phi)\phi^{l^*+\frac{1}{2}} \ln\phi \exp\left(-\phi^{l^*+\frac{1}{2}}(1-\phi)L\right) \\ &=\; -\ln\phi \, e^{-u} e^{-e^{-u}} = -\ln\phi \, G(u) \end{aligned} \tag{3.30}$$

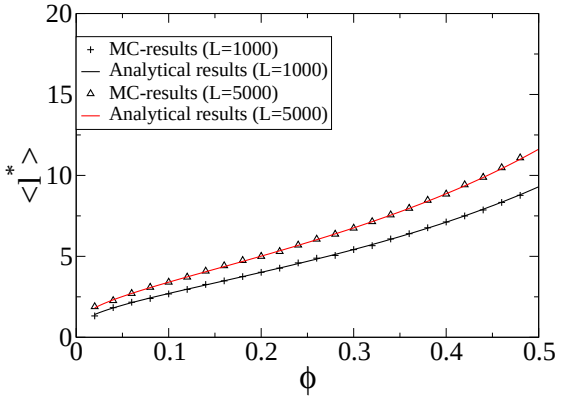

Figure 3.13: Comparison of analytical results (3.33) and MC simulations for the average longest bottleneck in dependence on ϕ (1000 samples).

where $G(u)$ is the Gumbel distribution (3.24) and we have introduced the function

$$u(l^*) = -\left(l^* + \frac{1}{2}\right)\ln\phi - \ln(1-\phi) - \ln L\,. \tag{3.31}$$

The expectation value of the Gumbel distribution is known to be $\langle u\rangle = \gamma_e$ [34], where $\gamma_e = 0.5772$ is the Euler-Mascheroni constant. Using (3.31) we have

$$\gamma_e = \langle u\rangle = -\ln\phi\,\langle l^*\rangle - \frac{1}{2}\ln\phi - \ln(1-\phi) - \ln L\;, \tag{3.32}$$

which can be solved for $\langle l^*\rangle$ to obtain

$$\langle l^*\rangle = \frac{\ln L + \ln(1-\phi) + \gamma_e}{\ln(1/\phi)} - \frac{1}{2}\,. \tag{3.33}$$

The dependence of the average longest bottleneck on ϕ is plotted in Fig. 3.13 which shows a good agreement between simulation results and Eq. (3.33). $\langle l^*\rangle$ diverges for infinite systems, as expected. However, it grows only of order $\mathcal{O}(\ln L)$, so that we have to keep this term in finite but large systems.

The variance of the Gumbel distribution $G(u)$ is $\sigma^2(u) = \frac{\pi^2}{6}$ [34]. Since $\sigma^2(l^*) = (\frac{du}{dl^*})^{-2}\sigma^2(u)$ (linear transformation) this yields the variance

$$\sigma^2(l^*) = \frac{\pi^2}{6\ln^2(1/\phi)} \tag{3.34}$$

of the longest bottleneck distribution $\mathcal{P}(l^*)$ so that $\sigma^2(l^*)$ does not depend on the system size, as can also be seen in Fig. 3.14.

If one approximates the transport capacity $J^*(\phi)$ for small ϕ by the corresponding current J^*_{SBA} of a system with one bottleneck, the expectation value is given by $\langle J^*(\phi)\rangle = \sum_{l^*=0}^{\infty} J^*_{\mathrm{SBA}}(l^*)\,\mathcal{P}(l^*)$. Due to the approximation by a continuous function, the norm $\sum_{l^*=0}^{\infty}\mathcal{P}(l^*) \neq 1$ can significantly deviate from

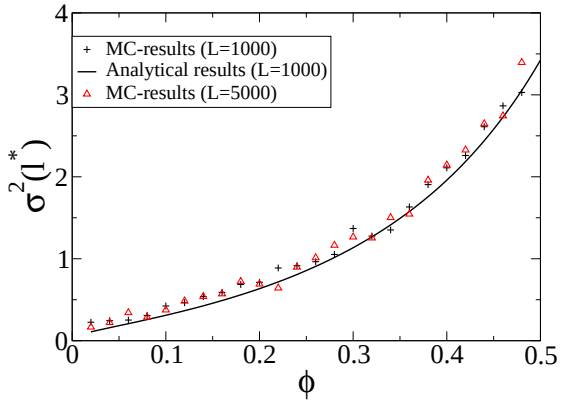

Figure 3.14: Comparison of analytical results (3.34) and MC simulations for the variance of the longest bottleneck in dependence on ϕ.

one. In order to reduce this error the result is divided by $\sum_{l^*=0}^{\infty} \mathcal{P}(l^*)$

$$\langle J^*_{\mathrm{SBA}} \rangle(\phi) = \frac{\sum_{l^*=0}^{\infty} J^*_{\mathrm{SBA}}(l^*)\, \mathcal{P}(l^*)}{\sum_{l^*=0}^{\infty} \mathcal{P}(l^*)} \,. \tag{3.35}$$

One can now either take numerical values for $J^*(l^*)$ or (semi-) analytical ones from ISA. Since $\mathcal{P}(l^*)$ decays fast around $\langle l^* \rangle$ it is sufficient to take into account only few terms in (3.35) in the vicinity of $\langle l^* \rangle$.

Since the asymptotic behavior of the transport capacity in the TASEP is $J^*(l^*) = q/4 + \mathcal{O}(1/l^*)$, [61], we can state by using (3.35) that $J^*(\phi, L) = \frac{q}{4} + \mathcal{O}\left(\frac{\ln(1/\phi)}{\ln L}\right)$ in the disordered TASEP. The variance $\sigma^2(l^*)$ is independent of the system size, thus the variance of the transport capacity $\sigma^2(J^*) = \mathcal{O}\left(\left(\frac{dJ^*}{dl^*}\right)^2 \sigma^2(l^*)\right) = \mathcal{O}\left(\frac{1}{(\ln L)^2}\right)$ vanishes logarithmically in the thermodynamic limit $L \to \infty$.

In order to display the generic character of the SBA, results for the transport capacity are not only shown for the TASEP but also for the disordered NOSC model without Langmuir kinetics (Tables 3.3 and 3.4). One observes a good agreement in both systems while the errors are of the same magnitude as for individual samples. This indicates that the probability distribution function for the longest bottlenecks is an appropriate approximation.

3.2.3 Corrections to SBA

In the following, corrections to the SBA are considered and the quality of this approximation as well as the range of its validity is checked by statistical considerations.

In principle, corrections to the transport capacity could come from the following effects:

- The longest bottleneck (length $l^* = \max\{l_1, l_2, \cdots\}$) is located near the boundary, not in the bulk as assumed in SBA. Since the probability that a

L	ϕ	no. of samples	$\langle J^* \rangle_{\mathrm{MC}}$	$\langle J^*_{\mathrm{SBA}} \rangle_{\mathrm{MC}}$	σ^2
500	0.1	200	0.2099	0.2244	3.2×10^{-5}
1000	0.2	100	0.1918	0.2024	1.7×10^{-5}
3000	0.1	100	0.2018	0.2110	2.5×10^{-5}
3000	0.2	50	0.1866	0.1960	1.1×10^{-5}

Table 3.3: Comparison of disorder averages in MC results and SBA results for the expectation value of the transport capacity. The defect hopping rate is $q = 0.6$. Column 4 shows the numerical results from MC simulations of the disordered TASEP. Column 5 displays results by SBA using the probability distribution (3.30) and column 6 shows the variance of the current obtained in the simulations.

L	ϕ	no. of samples	$\langle J^* \rangle_{\mathrm{MC}}$	$\langle J^*_{\mathrm{SBA}} \rangle_{\mathrm{MC}}$	σ^2
500	0.1	200	0.07495	0.08010	5.9×10^{-5}
1000	0.2	100	0.06852	0.07258	5.8×10^{-5}
3000	0.1	100	0.07438	0.075553	1.0×10^{-4}
3000	0.2	50	0.06852	0.07258	9.1×10^{-5}

Table 3.4: Same as in Table 3.3 but for the NOSC model without Langmuir kinetics. The forward hopping rate is inhomogeneous with $\omega_f^{\mathrm{fast}} \Delta t = 0.58$ and $\omega_f^{\mathrm{slow}} \Delta t = 0.32$. The other parameters are fixed: $\omega_h \Delta t = 0.8$, $\omega_s \Delta t = 0.22$, $\omega_b = 0$.

bottleneck at a given site is smaller than l is $P_<(l) = 1-\phi^l$ (see (3.25)), the probability of finding the first longest bottleneck[4] of length l at distance x from a boundary is $P(x) = (1-\phi^l)^x \phi^l$. Therefore the average distance of the longest bottleneck can be approximated as

$$\begin{aligned} \langle x \rangle &\approx \int_0^\infty x(1-\phi^{\langle l^* \rangle})^x \phi^{\langle l^* \rangle}\, dx = \frac{\phi^{\langle l^* \rangle}}{(\ln(1-\phi^{\langle l^* \rangle}))^2} \\ &\approx \phi^{-\langle l^* \rangle} = \phi^{1/2} L(1-\phi) e^{\gamma_e} = \mathcal{O}(L) \end{aligned} \tag{3.36}$$

where the longest bottleneck was approximated by its expectation value (3.33). That means for large systems the longest bottleneck is, on average, far from the boundaries. However, we see that for *finite* systems and small defect densities $\phi \ll 1$, $\langle x \rangle$ is becoming small, such that the boundaries might affect the transport capacity.

- Other smaller bottlenecks near the boundary can be treated by introducing effective boundary rates (see Sec. 3.2.4).

- Corrections from other bulk defects, i.e. "defect-defect interactions". Candidates for the leading contribution from this type of correction would be a) other bottlenecks of length $l_i \leq l^*$, which are near each other and sum up to induce a lower transport capacity. b) bottlenecks (of arbitrary length) located in the neighborhood of the longest one. The effect in a) would be maximal if two bottlenecks are separated only by a single non-defect site and their lengths adds up to be larger than l^*, $l_1 + l_2 > l^*$. In fig 3.15 the transport capacity of such a configuration with $l_1 + l_2 = 6$ is plotted and compared with a single bottleneck of length $l^* = 5$. The x-axis gives the position of the separating non-defect size, i.e. l_1. One

[4]There can be more than just one longest bottleneck.

observes that indeed configurations with $l_1, l_2 < l^*$ can add up to induce a transport capacity lower than $J(l^*)$. However the configurations with the most significant effect are those with $l_1 = 5$ or $l_2 = 5$, i.e. a bottleneck of length l^* with a single defect next to it. However latter configurations belong to the class in (b), which are therefore assumed to be more relevant. In the following paragraphs the influence of these corrections is quantified.

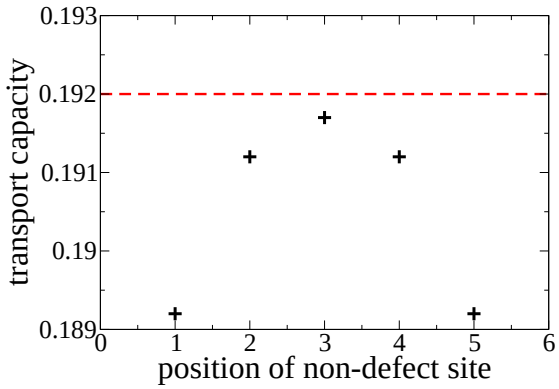

Figure 3.15: Configurations of two bottlenecks,lengths l_1 and l_2 separated only by a single non-defect site compared to a single one with length $l^* = 5$. $l_1 + l_2 = l^* + 1 = 6$.

In order to estimate the corrections due to defects near the longest one, we consider sub-ensembles of systems whose defect configurations are restricted to have a longest bottleneck of length l^*, while the defect distribution is not restricted by other constraints. Defect density ϕ and slow hopping rate q are considered to be fixed. For this ensemble the average transport capacity is given by

$$\langle J^* \rangle(\phi, L, l^*) = {\sum_{\mathbf{x}}}' J^*_{l^*}(\mathbf{x}) P_\phi(\mathbf{x}) \tag{3.37}$$

where $\mathbf{x} = (x_1, \ldots, x_N)$ denotes a defect configuration with defects at sites x_j. ${\sum}'$ means that the sum is restricted to such configurations for which the longest bottleneck has length l^* (and therefore $N \geq l^*$). $P_\phi(\mathbf{x})$ is the probability to find the configuration $\mathbf{x}$.

Denoting the transport capacity in SBA by J_{SBA} we have

$$\langle J^* \rangle(\phi, L, l^*) = J^*_{SBA}(l^*) + {\sum_{\mathbf{x}}}' \Delta J^*_{l^*}(\mathbf{x}) P_\phi(\mathbf{x}) \tag{3.38}$$

with $\Delta J^*_{l^*}(\mathbf{x}) = J^*_{l^*}(\mathbf{x}) - J^*_{SBA}(l^*)$. The expectation value for the corrections to SBA is then

$$\langle \Delta J^* \rangle(\phi, L, l^*) = {\sum_{\mathbf{x}}}' \Delta J^*_{l^*}(\mathbf{x}) P_\phi(\mathbf{x}) = \sum_{N^*} {\sum_{\mathbf{x}_{N^*}}}' \Delta J^*_{l^*}(\mathbf{x}_{N^*}) P_\phi(\mathbf{x}_{N^*}), \tag{3.39}$$

where $N^* = N - l^*$ is the number of defects besides at least one bottleneck of length l^*, and $\mathbf{x}_{N^*}$ denotes the positions of these defects.

We now want to treat corrections of other defects in terms of perturbations in small defect density ϕ. Since $P_\phi(\mathbf{x}_N) = \phi^N(1-\phi)^{L-N} = \mathcal{O}(\phi^N)$, the leading correction in $\mathcal{O}(\phi)$ comes from configurations with one additional defect besides the longest bottleneck:

$$\langle \Delta J^* \rangle(\phi, L, l^*) \approx {\sum_{x_1}}' \Delta J^*_{l^*}(x_1) P_\phi(x_1) = \left({\sum_{x_1}}' \Delta J^*_{l^*}(x_1) \right) P_\phi(x_1)\,, \tag{3.40}$$

where we have used that $P_\phi(x_1)$ does not explicitly depend on x_1 (all allowed defect positions are equally probable).

As long as the longest bottleneck is far from the boundaries, which can be assumed for large systems, the transport capacity does not depend explicitly on its position. Hence, instead of x_1 we can also use the relative position d of the additional defect to the longest bottleneck to characterize the configuration. If the defect is right of the longest bottleneck, we have $d > 0$, else $d < 0$. A necessary condition that SBA works is that the leading order correction yields a finite value for $L \to \infty$:

$$\sum_{d=-\infty}^{\infty}{}' \Delta J^*_{l^*}(d) < \infty \tag{3.41}$$

This condition is fullfilled if the "bottleneck-bottleneck interaction" $\Delta J^*_{l^*}(d)$ decays faster than $|d|^{-1}$ for large $|d|$, which is a restriction on the interaction strength of defects. The function ΔJ^* is a property of a system with two bottlenecks and can be obtained numerically by varying the distance of bottlenecks. That is exactly what was checked in Sec. 3.1 where the algebraic fits in Fig. 3.10 show numerically that in the TASEP this function indeed decays faster than $|d|^{-\gamma}$ with an exponent $\gamma > 2$, such that (3.41) is fullfilled for the TASEP.

We can further quantify the contribution of the first defect near the longest bottleneck as $P_\phi(x_1) = \phi(1-\phi)^{L-1} = \phi + \mathcal{O}(\phi^2)$. Since we have to take into account defects to the right and the left of the longest bottleneck, we obtain in leading order

$$\langle J^* \rangle(\phi, l^*) = J^*_{SBA}(l^*) + \left[{\sum_{d}}' \Delta J^*_{l^*}(d) \right] \phi + \mathcal{O}(\phi^2)\,, \tag{3.42}$$

where contributions with a defect on an adjacent site of the bottleneck (i.e. $d = 1$ and $d = -1$) do not appear in the sum, since they belong to longer bottlenecks. Note that this approximation does not explicitly depend on L.

This first order expansion for fixed l^* should work for small ϕ if (3.41) is fullfilled and the longest bottleneck is unique. However, in general the sum over all configurations $\mathbf{x}$ in (3.37) does not exclude other bottlenecks of length l^*. If there is more than one longest bottleneck (degeneracy), one has to be sure that other equivalent bottlenecks do not contribute stronger to the transport capacity, since in this case one would expand around the wrong reference configuration. Assuming that $\Delta J(d)$ is decreasing with d, in first order, this would be the case if another longest bottleneck has a neighboring defect with distance $d' < d$. Hence configurations containing such a bottleneck have to be skipped, which can lead to deviations in (3.42). The probability for a configuration exhibiting a bottleneck with $d' < d$ is given by $P^n[d' < d] = 1 - P^n[\mathrm{all\,d' \geq d}] = 1 - ((1-\phi)^{\mathrm{d}})^{\mathrm{n}-1}$,

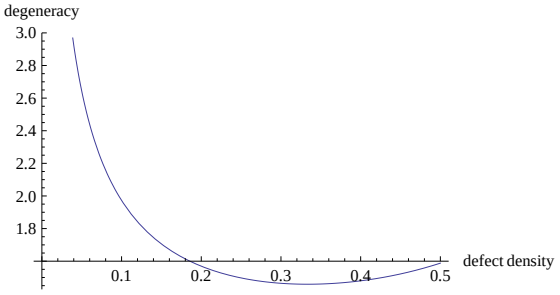

Figure 3.16: Expected degeneracy $\langle n \rangle$ of the longest bottleneck, approximating its length l^* by the mean value $\langle l^* \rangle$. Degeneracy becomes relevant below $\phi \approx 0.1$.

where n denotes the degeneracy, i.e. the number of bottlenecks with $l = l^*$. For small $d(n-1)\phi$ one can approximate $P^n[\text{all d}' \geq \text{d}] \approx 1 - \text{d(n} - 1)\phi$, hence $P^n[d' < d] \approx d(n-1)\phi$ and deviations of this kind can be neglected if $d(n-1)\phi \ll 1$. For large d the probability of corrections is higher, however in this regime the contributions $\Delta J(d)$ are neglectable. Hence the size of deviations is determined by the degeneracy n and defect density ϕ. The degree of degeneracy for a given bottleneck of length l^* is given by the number of bottlenecks with length l^*, following a Poisson distribution with expectation value $\langle n(l^*) \rangle = \phi^{l^*}(1-\phi)L(1-\phi) \approx \phi^{l^*} L$. Approximating l^* by its mean value (3.33), we have $n \sim 1/(\sqrt{\phi}(1-\phi)e^{\gamma_e})$. For $\phi > 0.1$, $n \sim 1$, as can be seen in Fig. 3.16, and deviations to our expansion can be neglected. For smaller ϕ the degeneracy increases significantly, since configurations with small l^* mix into the ensemble. For $l^* = 1$, for example, $n = \phi L$. While this degeneracy indeed also vanishes for $\phi \to 0$, for finite but small ϕ and large L, n can become a high number such that deviations characterized by $P^n[d' < d]$ become considerable.

Unfortunately currently no generic analytical results for $\Delta J^*_{l^*}(d)$ are available. For $l^* = 1$, i.e. a single defect, Foulaadvand et al. [30] applied ISA to obtain analytical results, while this approach does not apply for longer bottlenecks. Therefore one has to rely on the results of MC simulations to test the considerations made in this section. Systems with one bottleneck at a position far from the boundaries (> 200 sites) together with one single defect were simulated for several bottleneck lengths l^* and defect position d relative to the bottleneck to obtain $J^*_{l^*}(d)$. The interaction function is then obtained as $\Delta J^*_{l^*}(d) = J^*_{l^*}(d) - J^*_{l^*}$, where $J^*_{l^*}$ is the transport capacity of a single bottleneck. Since $\Delta J^*_{l^*}(d)$ should decay fast with increasing $|d|$ (see also last section), it is sufficient to take into account only defects within a finite distance to the bottleneck[5]. In order to obtain the expectation value $\langle J^* \rangle(\phi)$ for arbitrary configurations, one has to average over l^* in the same manner as in eq. (3.35).

In Fig. 3.17 average values of the transport capacity obtained by MC simulations are shown in dependence on the defect density as well for the disordered TASEP and the NOSC model. Each data point has been obtained by simulating 100 samples. For comparison the results in SBA and the leading order corrections obtained by (3.42) are included. We see that while already the SBA appears to be a good approximation, the accuracy of the corrections over a

[5]In our computations systems from $d = -d_{\max}, ..., +d_{\max}$ with $d_{\max} = 20$ were simulated. The relative error due to this cut-off is $\Delta < d_{max}^{-\gamma+1}$, while for the TASEP usually $\gamma < 3$.

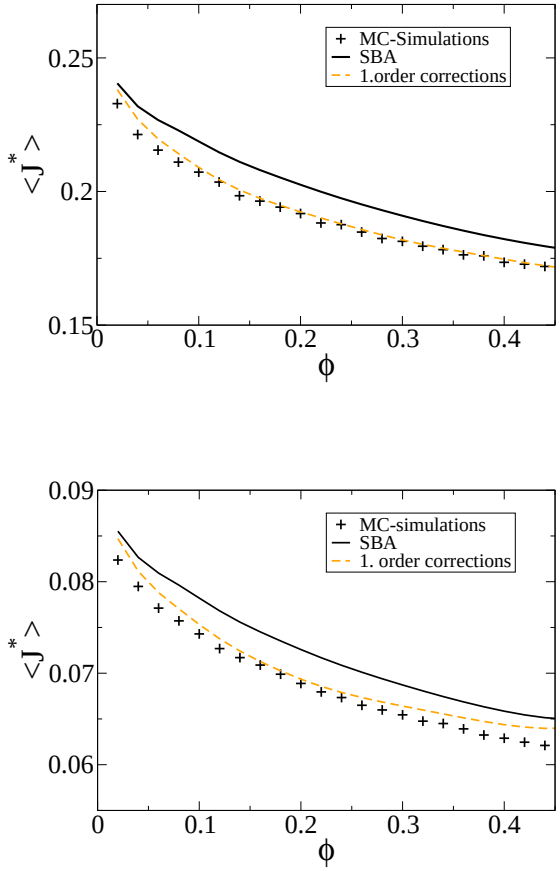

Figure 3.17: First order corrections to SBA as function of the defect density ϕ for the disordered TASEP (top) and the disordered NOSC model (bottom) using the probability distribution (3.29) for averaging over l^*. The slow hopping rates are $q = 0.6$ in the TASEP and $\omega_f^{\text{slow}} \Delta t = 0.32$ in the NOSC model. The system size is $L = 1000$ in each case.

wide range of defect densities is striking. It comes as a surprise that in the TASEP for larger defect densities the leading order correction, which takes into account only one additional defect, is extremely accurate. This is not expected since for larger ϕ there is a higher probability of having more than one defect in the vicinity of the longest bottleneck. However, these results indicate that the position of other defects beyond the first one do not significantly contribute to the transport capacity. Furthermore we see that the deviation of the SBA approaches a rather constant value for larger ϕ, despite the factor ϕ in (3.42). This indicates that for larger bottlenecks, the influence of single defects on the transport capacity is weaker than for small bottlenecks, which is consistent with results from the last section.

However one observes deviations from the first order corrections for small defect densities. In this regime defect configurations with many bottlenecks of length l^* mix into the ensemble leading to degeneracy effects that contribute

significant deviations to the first order expansion as was argued above.

For periodic boundary conditions the results are almost the same exhibiting no significant discrepancies compared to Fig. 3.17, therefore the boundary effects stated at the beginning of this subsection can be assumed to be neglectable[6].

3.2.4 The phase diagram of disordered driven lattice gases

The phase diagrams of driven lattice gases that have exactly one maximum all have the same topology. This is based on a maximum current principle and shock dynamics [87, 81, 35]. The class of DLGs meeting this condition includes many weakly interacting lattice gases, e.g. the TASEP and the NOSC model [71, 36]. If disorder is included, some conceptual problems with the expression *phase diagram* arise. Usually a *phase transition* is identified by a non-analytic behavior of a macroscopic quantity. In driven lattice gases these can be discontinuities in the density (first order transitions) or kinks in the dependence of the current on the system parameters (second order transition). Strictly speaking these transitions only occur in infinite systems, since non-analyticities are only present in the *thermodynamic limit*. In disordered systems, however, there is no unique way of taking the limit $L \to \infty$ since this cannot be done with a fixed defect sample and, as we have seen, macroscopic quantities like the transport capacity may be sample-dependent. Indeed, the process of taking the thermodynamic limit has to be specified, since it is ambiguous how the "new" defect sites by increasing L are included. Enaud et al. [24], e.g. discussed two possibilities of defining a limit $L \to \infty$ and showed that if this limit is taken by including sites at the boundaries there actually is no unique phase transition *point* if exit rate β is fixed and α is varied.

For infinite systems, according to equation (3.33), the length of the maximum bottleneck is infinite and thus the transport capacity would be the same as the one of a pure system with hopping rate q, $J^* = q/4$. In this work, however, the focus is on "finite but large systems" and we are considering ensembles, not individual samples. Since the longest bottleneck increases as $\mathcal{O}(\ln L)$, the transport capacity approaches its asymptotic value only logarithmically: $J^*(L) = q/4 + \mathcal{O}(1/\ln L)$ (see also [61]). For finite but large systems we have to take into account terms of the order $\mathcal{O}(1/\ln L)$. Hence in this view, we want to consider an explicit dependence on the system size and cannot take the thermodynamic limit to obtain phase transitions.

In Sec. 3.1 it was shown that if a single bottleneck is near a boundary, phase separation cannot occur. Then the character of phase transitions is different, since the current is not limited by the bottleneck anymore but by the bulk exclusion like in the pure system. In this case the phase transition is of second order. On the other hand, if the bottleneck is far from the boundaries at a distance $d = \mathcal{O}(L)$ there is not only a sharp kink, but also macroscopic phase separation occurs accompanied by a steep increase of the average density, indicating a first order transition. This corresponds to the phase separating transition that can already be observed for single defects [46].

In Sec. 3.2.3 we have seen that the average distance of the longest bottleneck from the boundaries is $\mathcal{O}(L)$. Hence on average we have a sharp transition for large L. Therefore we call this a phase transition for finite but large systems at

[6] They are not explicitly plotted since no deviations are visible

the critical point α^* where the current reaches J^*, although this point depends on the system size.

Effective boundary rates

The investigations of the last section in a TASEP with one and two bottlenecks far from the boundaries (distance $\mathcal{O}(L)$) showed that the transport capacity only depends on the longer bottleneck, while outside of the bottleneck phase (B) the current only depends on the position of a bottleneck that is near a boundary. The negative edge effect, predominant in that regime (see Appendix A), is considerable for bottlenecks not more than ~ 20 sites away from the boundaries and leads to a lowered current in the non-bottleneck phases. The concept of *effective boundary rates* that was introduced to take into account this effect, rescales boundary rates virtually while the bulk of the system is treated like a pure one. Enaud et al. [24] considered defect ensembles in the disordered TASEP numerically and showed that the phase transition between L and H can be described by retuning boundary rates. This indicates that the concept of effective boundary rates can also be applied for the disordered TASEP, i.e. for many defects.

Taking into account defects near the boundary, we can write the current in the generic form $J(\alpha) = \alpha(1-\alpha) + \Delta J_\alpha(\mathbf{x})$. Here α is the entry rate in the low density phase. However due to particle-hole symmetry[7] we can transfer this result to β and the high density phase. The defect configuration $\mathbf{x} = (x_1, x_2, ...)$ is defined in the same manner as in Sec. 3.2.3. Indeed, taking the expectation value we can proceed analog as in the last section to obtain the average corrections in leading order

$$\langle \Delta J_\alpha \rangle(\phi) \approx \phi \left[\sum_{d_1} \Delta J_\alpha(d_1) \right] \tag{3.43}$$

where d_1 is the position of the first defect and $\Delta J_\alpha(d_1) = J_\alpha(d_1) - \alpha(1-\alpha)$. Thus the corrections by defects near the boundaries are of the same magnitude as the corrections to SBA, while the "defect-boundary interaction" $\Delta J_\alpha(d_1)$ is in general not the same as the "defect-defect interaction" $\Delta J_{l^*}(d_1)$.

Fig. 3.18 shows that results obtained by (3.43) yield an accurate approximation for the expectation value of the current for low entry rates, though for larger ϕ they appear to slightly overestimate the pure numerical values.

The expectation value of the effective entry rate can then be obtained if the current-density relation of the pure system $J(\rho)$ is known.

If the relations $\alpha_{\text{eff}}(\alpha)$, $\beta_{\text{eff}}(\beta)$ and their inverses $\alpha^{-1}(\alpha_{\text{eff}})$ and $\beta^{-1}(\beta_{\text{eff}})$ are known as well as the transport capacity J^*, we are in principle able to map the problem of determining the phase diagram of a disordered system on a pure system with a known dependence of the current on the boundary rates $J(\alpha, \beta)$:

1. If the system current $J(\alpha_{\text{eff}}, \beta_{\text{eff}}) < J^*$ the system globally has the same properties as the pure one if one replaces the real boundary rates by the effective ones.

[7] Note that for individual defect samples, particle-hole symmetry is broken, but for large ensembles it is restored.

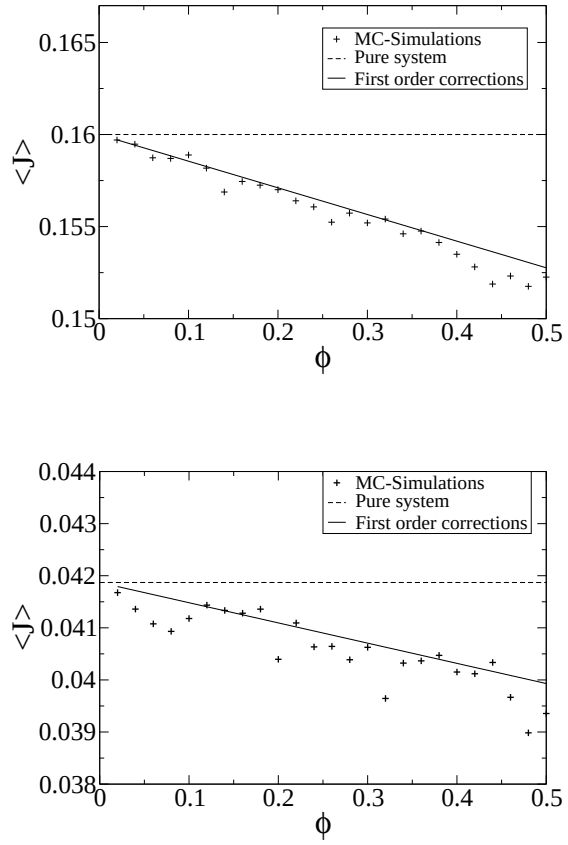

Figure 3.18: Disorder average of the current in dependence on the defect density in the disordered TASEP with $q = 0.6$, $\alpha = 0.2$ (top) and the disordered particle-conserving NOSC model with $\omega_f^{\text{slow}}\Delta t = 0.32$ (bottom). MC simulations are compared with leading order corrections to the pure current obtained by (3.43). Entry rates are chosen to be small enough so that $J < J^*$.

2. At the points in the $\alpha-\beta$-space where $J(\alpha_{\text{eff}}, \beta_{\text{eff}}) = J^*$, a phase transition to a bottleneck phase occurs in which the current is independent of the boundary rates and maximal.

In particular in the TASEP the expectation value of the effective boundary rates can be determined

$$\langle \alpha_{\text{eff}} \rangle = \left\langle \frac{1}{2} - \sqrt{\frac{1}{4} - J_\alpha} \right\rangle = \frac{1}{2} - \sqrt{\frac{1}{4} - \langle J_\alpha \rangle} + \mathcal{O}(\sigma^2) \qquad [8] \ . \tag{3.44}$$

There is a phase transition from low density to high density phase for $\alpha_{\text{eff}}(\alpha') = \beta_{\text{eff}}(\beta') \Leftrightarrow \alpha' = \alpha_{\text{eff}}^{-1}(\beta_{\text{eff}}(\beta))$ which in general is not on the diagonal $\alpha = \beta$. Nonetheless , due to particle-hole symmetry we have on average

[8] Though σ merely decays logarithmically, considering only boundary effects that are not dependent on system size, we can take the strong continuum limit where $\mathcal{O}(1/\ln L)$ vanishes.

$\langle J_\alpha \rangle = \langle J_\beta \rangle$ that leads to $\alpha' = \beta'$ on average. The transition to the phase separated bottleneck phase is determined by $\alpha^*(1-\alpha^*) = J^*$ or $\beta^*(1-\beta^*) = J^*$. Unfortunately, we are not able to determine the functions $\alpha_{\text{eff}}(\alpha), \beta_{\text{eff}}$ explicitly, since for each α, β we need to obtain a set of functions $\Delta J_{\alpha,\beta}$ which requires much computational effort, as long as no analytical results are available. Nonetheless, the concept of effective boundary rates can be used to extract some qualitative properties of the phase diagram, though obtaining quantitative results is difficult.

However, since corrections of the SBA are of the same order as corrections to the boundary rates, we can approximate $\alpha_{\text{eff}} \approx \alpha$ and $\beta_{\text{eff}} \approx \beta$ in order to find α^* and β^*. In Fig. 3.19 the current and the average density is plotted in dependence on the entry rate α. One observes a steep increase in the average density at the point where the plateau begins. Thus this transition can be characterized as a first order phase transition, like in the single bottleneck system.

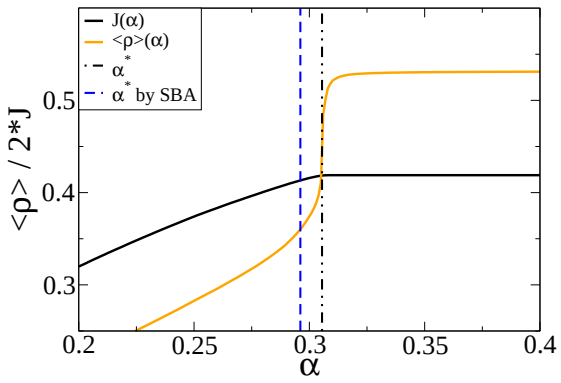

Figure 3.19: Mean density $\langle\rho\rangle$ and current J in dependence of α for fixed $\beta = 0.9$, $q = 0.6$ and $\phi = 0.05$ obtained by MC simulation of a system with $L = 2000$ and fixed defect sample. One observes a steep increase at the same point where the current reaches the plateau.

Fig. 3.20 displays a sketch of the phase diagram of an individual defect sample in the disordered TASEP. The transition line between H and L is distorted compared to the homogeneous case and single bottleneck systems, since for individual defect samples the effect of boundary near defects on effective boundary rates can be different at the left or right boundary. Taking the disorder average, the transitions are again on the diagonal line $\alpha = \beta$. Similar to the TASEP with a single bottleneck, phase separation, induced by the longest bottleneck is observed (see e.g. [96]).

While for more complex systems the exact form of the current-density relation is in general not known, we can assume that the concept of effective boundary rates should in principle also work for other disordered driven lattice gases as long as the edge effect is not too large, i.e. the term on the right hand side of (3.43) converges. Hence the single bottleneck approximation together with the concept of effective boundary rates provides an approach to obtain crucial features like transport capacity and structure of the phase diagram of a generic class of disordered driven lattice gases.

Until now it was assumed that no particles can enter or exit the system

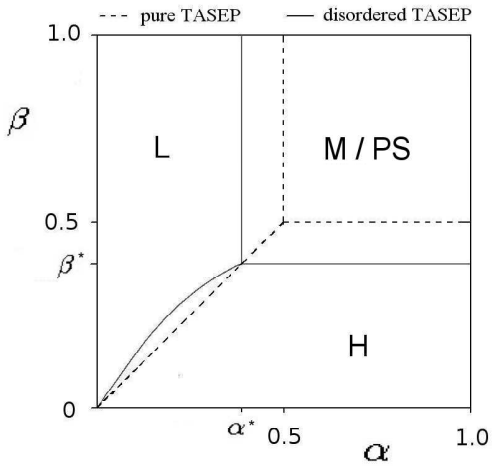

Figure 3.20: Schematic phase diagram of the disordered TASEP for a single defect sample. It is obtained by taking the phase diagram of the TASEP in dependence on α_{eff} and β_{eff} with one bottleneck that corresponds to the longest one and rescaling the axis by $\alpha_{\text{eff}} \to \alpha$, $\beta_{\text{eff}} \to \beta$. For comparison the phase transitions of the homogeneous TASEP with $p = 1$ were included (dashed lines).

in the bulk. This view is valid for gene transcription/translation where RNA-polymerase/ribosomes can only attach and detach to the nucleic acid strands at distinct sites which can be interpreted as the boundaries of the system. However, for modeling intracellular transport on cytoskeletal filaments, the mechanism of attachment and detachment of motor proteins must be explicitly taken into account if no crucial features of the system are supposed to be dropped. If entering and exiting of particles like in the TASEP with Langmuir kinetics is allowed, the concept of a globally constant transport capacity is not supposed to hold since the current is spatially varying. In the following section, driven lattice gases without particle conservation in the bulk are considered and a local extremal principle is introduced that will help us to understand these systems.

3.3 Disordered driven lattice gases with Langmuir kinetics

The single bottleneck approximation turns out to yield good results for driven lattice gases with particle conservation in the bulk. In this section driven lattice gases in presence of Langmuir kinetics, i.e. particles entering and exiting the system at any point in the bulk, are investigated. We have seen that Langmuir kinetics are crucial to capture the phenomenology of intracellular transport by motor proteins on single tracks. In comparison to the TASEP, the current profile in the presence of Langmuir kinetics is no longer constant (see Sec. 2.3.3). This requires a slightly different approach since now a "local" point of view becomes

necessary. Indeed, as was argued in Sec. 3.2.1, the SBA, though a global quantity, arises from the assumption that bottlenecks restrict the current locally. This suggests that the transport capacity which is a global feature of particle conserving driven lattice gases can be generalized by a spatially varying quantity that yields the SBA in the limit of vanishing attachment and detachment rates. Hence we introduce a *local transport capacity*, defined in Sec. 3.3.1 that depends on the position in the system. This important observable is of direct relevance for biological applications.

In this section the disordered TASEP with Langmuir kinetics is studied as a paradigmatic system for driven lattice gases that can be applied to model intracellular transport on inhomogeneous tracks. First current and density profiles are investigated by computer simulations to discover new phenomena. In the subsequent subsections a theoretical framework, based on a local extremal principle and a generalization of the SBA, is developed. These results are used to obtain the structure of the phase diagram. The validity of this approach is checked by computing the probability for phase transitions in large ensembles with different individual defect configurations. The procedure turns out to be generic for driven lattice gases that exhibit a single maximum in their current-density relation and have short-ranged interactions (see conditions in Sec. 2.3.3) indicating that the topological structure of the phase diagram of this system class is the same. Therefore the qualitative features are assumed to be valid in real systems like intracellular transport on cytoskeletal filaments.

3.3.1 Model and Definitions

We consider driven lattice gases with open boundary conditions and Langmuir kinetics (LK). To be more specific we focus on the TASEP-LK (see Sec. 2.3.2).

For convenience fixed boundary densities ρ_0 and ρ_L rather than the corresponding rates α an β are used as boundary conditions. Densities and rates are related by $\rho_0 = \alpha$, $\rho_L = 1 - \beta$. Nonetheless this relation is not generic for other driven lattice gases. In order to be transferable to other systems, here boundary conditions are implemented by fixed boundary densities. However, if the TASEP-LK is considered, the terminology of boundary rates can be used.

Langmuir kinetics are realized by creation and annihilation of particles in the bulk. This can be interpreted as particle exchange with a bulk reservoir and corresponds to attachment and detachment processes in the biological context. The corresponding rates will be considered to be homogeneous, i.e. independent of the position, throughout this section [9].

Usually we are interested in the weak continuum limit as defined in the last section, while in special cases we also consider the strong continuum limit where $\mathcal{O}(1/\ln L)$ vanishes. In the following we restrict ourselves to systems where the local creation and annihilation rates ω_a and ω_d are rescaled with the system size, while the global rates $\Omega_a := \omega_a L$ and $\Omega_d := \omega_d L$ are kept constant. Hence Ω_a and Ω_d are system parameters while ω_a and ω_d are adjusted to the system size. In particular in the (weak and strong) continuum limit, the local rates vanish: $\omega_a, \omega_d \to 0$ for $L \to \infty$. In these limits analytical tools introduced in Sec. 2.3.3 can be applied.

[9] The effects of inhomogeneities in the attachment and detachment rates have recently been studied in [41].

The current-density relation of the systems considered here are assumed to exhibit a single maximum (which is the case for the TASEP-LK). The maximum is at a point ρ_M and takes the value $J_M = J(\rho_M)$. In this case for a given current J, two possible values for the density, the *high density value* $\rho_H(J) > \rho_M$ and the *low density value* $\rho_L(J) < \rho_M$ exist.

The non-conservation of particles can be expressed by a source term in the equation of continuity of the stationary state (see also Sec. 2.3.3) :

$$J_j - J_{j-1} = s(\rho) \quad [10] \tag{3.45}$$

where J_j is the current through the bond between sites j and $j+1$. The attachment of particles is assumed to be inhibited by particles occupying sites, so we assume $s(\rho)$ to be a globally decreasing function. Since $\omega_a, \omega_d \to 0$ in the continuum limit, we also have $s(\rho) \to 0$ in this limit. Hence for large systems the current is locally constant in a microscopic environment and the CDR is the same as in the corresponding system without LK [81, 35]. The transition rules of the TASEP-LK are explicitly described in Sec. 2.3.2, while here hopping rates p_j can also depend on the position j. The source term is given by $s(\rho) = \omega_a(1-\rho) - \omega_d\rho$. We call the hopping rates p_j, which are site-dependent properties, *intrinsic parameters* and in the following will be considered as fixed, $p = 1$ and $q = 0.6$, if not stated otherwise. In contrast to this we consider the explicit dependence of the system properties on the *external parameters* α, β, Ω_a and Ω_d. Other driven lattice gases of the class characterized above can be written in the same way, while the local parameters might depend on the states in the vicinity of the sites and additional correlations might occur. Nonetheless one can assume that the TASEP-LK is quite universal as a paradigmatic model [35].

In this section we consider on the one hand defects that have distinct positions in the system and on the other hand random disorder with finite defect density ϕ, like for the TASEP without LK.

The particle-hole symmetry of the TASEP also holds if Langmuir kinetics are included, while we have to add the operation $\Omega_a \leftrightarrow \Omega_d$ to (2.8) in order to leave properties unchanged. However, the particle-hole-symmetry is not essential for the generic behavior, but it allows to reduce the parameter space that needs to be investigated.

The TASEP-LK with one defect site was already investigated numerically and analytically in [79]. Now we want to generalize these results to arbitrary defect samples. For this purpose we generalize the principle of the transport capacity to introduce a *local transport capacity* J_j^*, which is the site-dependent maximum current that can be achieved by tuning the external parameters α, β, Ω_a and Ω_d in the continuum limit [11]. This quantity will be discussed in detail in section 3.3.3.

3.3.2 Observations by Computer Simulations

In this section some properties of the system are summarized that can be observed with computer simulations. For this purpose quantities of the inhomogeneous TASEP-LK are compared with the homogeneous TASEP-LK and the

[10] Actually $s(\rho)$ can be defined this way.

[11] Note that it is important that first the external rates are tuned and then the continuum limit is taken, since the vanishing of the local bulk influx $s(\rho)$ is necessary.

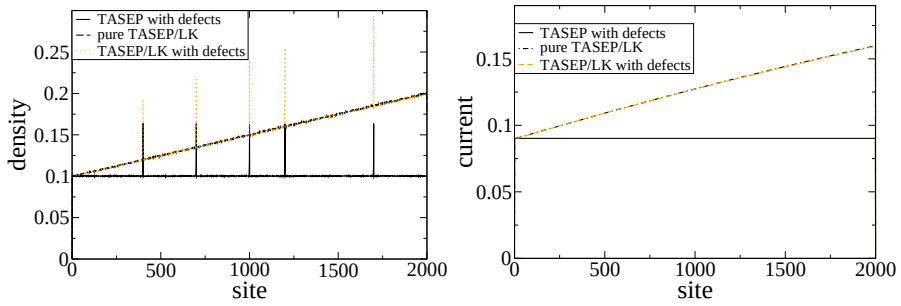

Figure 3.21: Comparison of current and density profiles for $\alpha = 0.1$ and $\beta = 0.9$ (low density phase) in the TASEP with defects, homogeneous TASEP-LK and TASEP-LK with defects and $\Omega_a = \Omega_d = 0.1$.

TASEP with defects. For simulations, random-sequential update with fast hopping probability $p = 1$ is used. If not specified else, $q = 0.6$ is fixed as slow hopping probability. The unit of time is $\Delta t = 1$ so that probabilities and rates have the same numerical value.

Few defects/vanishing fraction of defects

Before finite defect densities $\phi > 0$ are considered, systems with a fixed number of defects in the continuum limit ($\phi = 0$) are discussed. Figs. 3.21–3.25 display the dependence of the densities and the current on the position in the system.

Fig. 3.21 shows the density and current profiles of a TASEP-LK-system with five defects, a homogeneous TASEP-LK-system and a TASEP with five defects in the low density phase. The density profiles of inhomogeneous and homogeneous TASEP-LK-systems differ only in the occurrence of narrow density peaks at the defects, while globally the density profile is the same. The current profiles of the homogeneous and inhomogeneous system are identical. In contrast, the density profile of the TASEP with defects at the same sites shows density peaks as well, but the current profile (and the density profile far from the boundaries) is flat. This is due to particle conservation while the lateral influx of particles allows a spatial variation of the current profile in the TASEP-LK where particles are not conserved in the bulk.

Fig. 3.22 shows the corresponding situation for low exit rate and high entry rate. Due to particle-hole-symmetry, the results are analogous to the previous case. Adopting the terminology of the homogeneous system, the inhomogeneous TASEP-LK-system can be considered to be in a high and low density phase, respectively.

Fig. 3.23 displays density profiles for $\alpha \approx \beta$. As in the case above, homogeneous and inhomogeneous TASEP-LK-systems exhibit the same density profiles, apart from the peaks. In this case we see a shock which cannot be observed in the TASEP with defects (except at $\alpha_{\text{eff}} = \beta_{\text{eff}}$).

Increasing the entry rate α for fixed and large β one observes a queuing transition in Fig. 3.24: At a critical entry rate α^* the peak at the leftmost defect broadens, forming a high density region. This corresponds to phase separation in the bottleneck phase (B) of the inhomogeneous TASEP. There, however, the

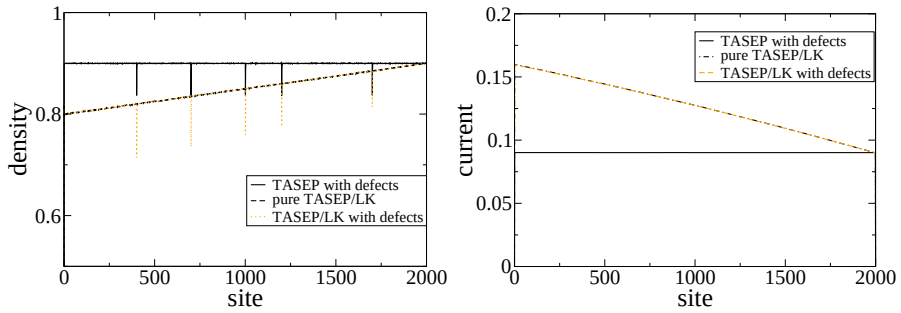

Figure 3.22: Comparison of current and density profiles for $\alpha = 0.9$ and $\beta = 0.1$ (high density phase) in the TASEP with defects, homogeneous TASEP-LK and TASEP-LK with defects.

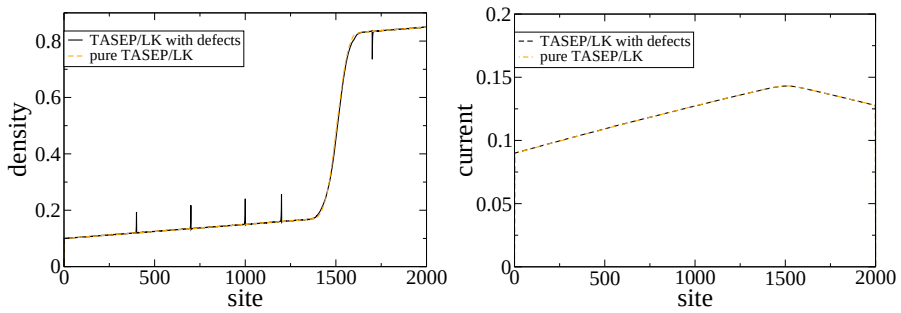

Figure 3.23: Comparison of current and density profiles for $\alpha = 0.1$ and $\beta = 0.15$ (high density phase) in the homogeneous TASEP-LK and TASEP-LK with defects.

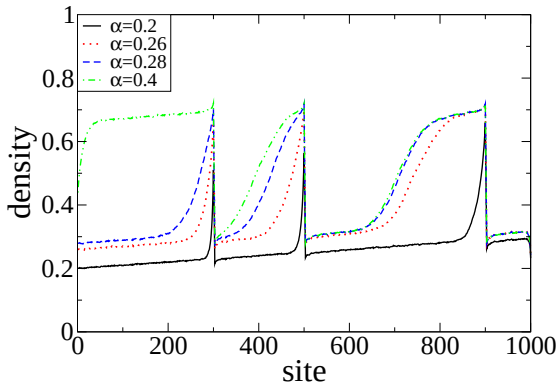

Figure 3.24: Density profiles for increasing values of α and fixed $\beta = 0.9$. At a critical value α' a high density region at the most right defect occurs (phase separation). For higher α multiple high density regions appear.

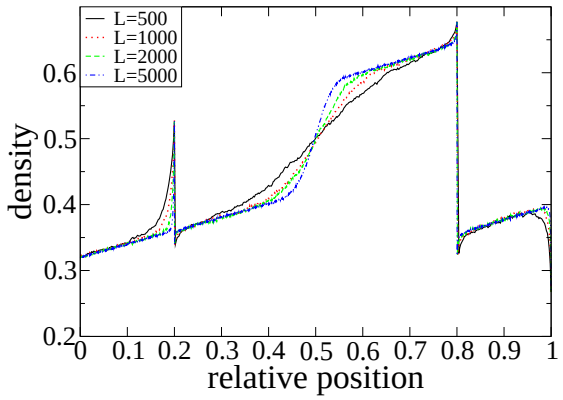

Figure 3.25: Density profiles for identical macroscopic parameters $\Omega_a = 0.1$, $\Omega_d = 0.1$, $\alpha = 0.35$, $\beta = 0.9$ *but different system sizes* L. *The left boundary of the high density region (shock) becomes steeper with increasing system size, indicating a macroscopic regime.*

high density regime always extends to the left boundary. In contrast, the inhomogeneous TASEP-LK-system exhibits a stationary shock separating the low and high density region. Numerical scaling of the system size in Fig. 3.25 shows that the shock indeed is getting sharper with increasing system size. Thus the high density region extends over a finite fraction of the system, corresponding to phase separation. In contrast, the peaks diminish for larger systems indicating that they are just local phenomena. We can associate this phase separation with a phase transition at the critical parameter value α' and call this phase *defect induced phase separated (DPS)*.

Increase in α further moves the shock position to the left. The density profile right of the defect where phase separation occurred does not change anymore by varying the entry rate. The same is true for the *output current* at the right boundary $J_{\text{out}} = J(L)$. At some value of α a second high density region starts to form. Thus in a system with many defects *multiple shocks* can occur associated with alternating domains of high and low density.

Above a critical value α^*, where a high density domain extends to the left boundary, the density profile and the current in the system are independent of the entry rate. Since this independence also holds for large β, we call this a *Meissner phase* in analogy to superconductors, where the magnetic field in the interior bulk is independent of exterior fields. This terminology was also used for the boundary independent phase in the homogeneous TASEP-LK [76] (see also Sec. 2.3.3). However, one has to note that while in the homogeneous system there are long-range boundary layers in the density profile which *do* depend on boundary rates, the Meissner phase in the disordered system only exhibits short-range boundary layers, so the corresponding phases in the two models have different characteristics. The current profile in fact does not depend on the boundary rates, both in the homogeneous and the inhomogeneous system.

Due to particle-hole-symmetry all considerations made in this section can be transferred to the high density phase by replacing α with β.

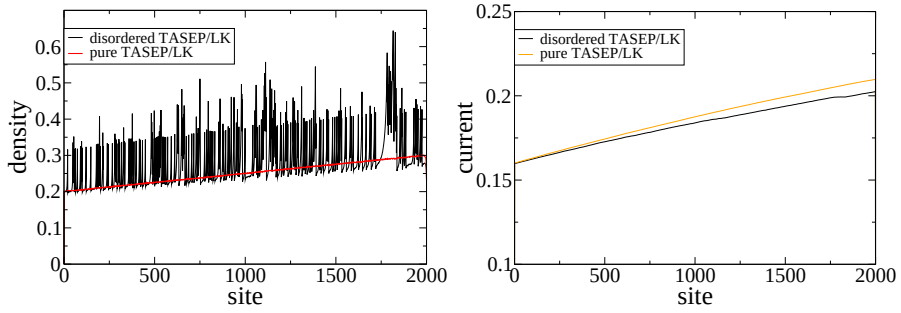

Figure 3.26: Comparison of current and density profiles for $\alpha = 0.1$ and $\beta = 0.9$ (low density phase) in the disordered TASEP-LK with defect density $\phi = 0.1$ and homogeneous TASEP-LK.

Finite fraction of defects and disordered systems

If the density of defects ϕ is finite and the number of defects is of the order of the system size, even a local increase of the density in the vicinity of the defects has considerable impact on the average density due to the large number of defects. The effect can be observed in Fig. 3.26 where disordered systems with small but finite defect density ϕ have been simulated for small α and large β. In contrast to systems with few defects, the current profile of the disordered system differs from that of the homogeneous system. This is due to the change of the density by defects, which leads to an altered influx of particles in the bulk by attachment/detachment. So the gradient of the current profile in the disordered system is different from the one in the homogeneous system and also from the system with few defects because in the latter the effect on the average density is negligible.

As in the TASEP-LK with few defects one observes multiple high and low density domains for large boundary rates, which is displayed in Fig. 3.27. In fact it is harder to distinguish macroscopic high and low density regimes in the disordered case because of the rapid changes of density on a microscopic scale. One has to simulate rather large systems in order to identify a macroscopic high(low) density domain by inspection. In Sec. 3.3.4, a numerical method is introduced that can detect high and low density domains automatically.

3.3.3 Theoretical treatment

In this subsection a theoretical framework for the observations made by Monte Carlo simulations is developed. Concepts developed in this section are expected to be generic for a larger class of disordered driven lattice gases that have a single maximum in the current-density relation and weak induced effective interactions between defects, i.e. satisfying the condition (3.41). In addition, we assume that the bulk influx term $S(\rho)$ is decreasing with increasing density, as in the TASEP-LK.

First we summarize the properties that distinguish the inhomogeneous (disordered) TASEP-LK from the TASEP and homogeneous TASEP-LK, respectively.

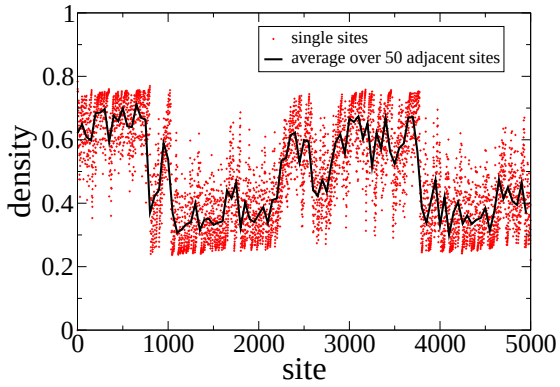

Figure 3.27: Density profile for $\alpha = 0.9$ and $\beta = 0.9$ in the disordered TASEP-LK with defect density $\phi = 0.2$. One observes phase separation with alternating high and low density domains. The black line displays the density, averaged over 50 adjacent sites.

1. In the TASEP-LK the particle number is not conserved in the bulk. Therefore generically the current profile is *not flat* and *stationary shocks* can occur in the bulk. For particle conserving systems these are not possible [81, 27].

2. In the homogeneous TASEP, the current is restricted by the upper bound $J_{\text{hom}}^{\max} = \rho_{\max}(1 - \rho_{\max}) = 0.25$ (for hopping rate $p = 1$) due to the bulk exclusion. In [79] it was shown that also in the TASEP-LK, a single defect site d restricts the current by a value $J_d^* := J_d^{\max} < J_{\text{hom}}^{\max}$ at this site, that cannot be exceeded by tuning external parameters. The quantity J_d^* is exactly the local *transport capacity* defined in Sec. 3.3.1. In the TASEP without LK this restriction was valid for the whole system since the current is spatially constant. Hence $J^* \equiv J_d^*$ there. However, due to the spatially varying current in the presence of Langmuir kinetics, this effect is only local and the maximum value of the current $J_i^{\max}$ on sites i far away from the defect can vary from J_d^*. For completeness, we define $J_i^* = J_{\text{hom}}^{\max}$ on non-defect sites i, such that the transport capacity is peaked on a single site. If the current imposed by the boundary rates is larger than the transport capacity of a defect, phase separation occurs, exhibiting stationary shocks. In the inhomogeneous TASEP no stationary shocks can occur in the bulk, thus the high density regime always fills the whole system left of the current limiting defect, as we saw in the last section.

3. In systems with only few defects the relation between the average density and the current at a given site is the same as in the homogeneous system. Thus current profiles are almost the same (as long as the transport capacity is not exceeded). In disordered systems with a finite fraction of defects, however, the current-density relation is not the same as in the homogeneous system and depends on q and the distribution of defects, since the large number of density peaks have influence on the source term $s(\rho)$ in (3.45) on a macroscopic scale. Therefore the current profiles differ from the homogeneous case.

In order to capture these properties, we follow the concept of [79] by focusing on the current profiles $J(x)$ and apply the analytical tools presented in sec 2.3.3.

The influence of defects: additional initial conditions

Locally the current profiles are determined by the continuity equation (3.45). Following Sec. 2.3.3, the current obeys the ODE

$$\frac{dJ}{dx} = S(\rho) + \mathcal{O}(1/L) \tag{3.46}$$

with $x = \frac{i-1}{L-1}$ and the global source term $S(x) = L\, s(x)$ (see Sec. 2.3.3). In the TASEP-LK, for example, we have $S(x) = S(\rho(x)) = \Omega_a(1-\rho(x)) - \Omega_d\rho(x)$. In the weak and strong continuum limit terms of $\mathcal{O}(1/L)$ are neglected, hence (3.46) becomes an ordinary first order differential equation in x. The ODE is overdetermined and each initial condition at a point x_0 is associated with one solution of (3.46) $J_{x_0}(x)$ for the current and $\rho_{x_0}(x)$ for density, respectively, provided that a unique CDR $J(\rho)$ exists. We call the mathematical solutions to single initial conditions $J_{x_0}(x)$ and $\rho_{x_0}(x)$ *local current/density profiles*.

For the TASEP-LK with a single defect it was shown by Pierobon et al. [79] that the finite transport capacity at the defect site, corresponding to a local upper bound of the current, can be regarded as an additional condition on the current profile. They argued that the local solution of (3.46) with the initial condition $J(x_d) = J^*(x_d)$ becomes relevant if the local current profiles of the boundary conditions exceed J^* at the defect site. Here this approach will be justified and generalized to a larger class of driven lattice gases with many defects, including randomly disordered systems, that meet the restrictions noted in Sec. 3.3.1.

The observations made in [79] motivate the generalization of the global transport capacity to driven lattice gases (including TASEP-LK) with many defects but low defect density, introducing an approximation similar to SBA. We call it the *locally independent bottleneck approximation (LIBA)*: The local transport capacity at a site x, $J^*(x)$, is approximately equal to the maximum current that can be achieved by tuning the boundary rates in the corresponding system containing only one bottleneck at this site [12]. Thus $J^*(x)$ can be obtained by referring to a single-bottleneck system where all other defects (except the bottleneck at site x) have been removed, similar to SBA.

In systems without LK the current is spatially constant and cannot exceed the minimum of $J^*(x)$. This corresponds to the transport capacity of the longest bottleneck, since in single bottleneck systems the maximum current is equal to the local transport capacity $J^*(x)$ and decreases with l. In this case the LIBA reproduces the SBA.

The LIBA neglects the influence of other defects on the transport capacity at site x. Nonetheless, we claim that the influence of other defects on the transport capacity can be considered as a perturbation in the same way as it is the case for the SBA in particle conserving systems. Since the local attachment and detachment rates vanish in the continuum limit, the transport capacity of a bottleneck should be the same as in the corresponding particle conserving system and is independent of Ω_a and Ω_d. For the TASEP without LK the analytical

[12] In this terminology a non-defect site is also called a bottleneck of size 0.

results obtained in 3.1 are available that can be used to obtain approximations for the transport capacity. Since the maximal current in these systems depends only on the bottleneck length $l(x)$ this holds also for the transport capacity. The concept of a local transport capacity is applicable if interactions of defects near a bottleneck are not to large (satisfying (3.41)) and distances of defects are not too small (i.e. low defect density [13]) such that they can be treated as small perturbations.

Hence, the local transport capacity $J^*(x)$ yields an upper bound for the current profile,

$$J(x) \leq J^*(x) \qquad \text{for all } x, \tag{3.47}$$

while the function $J^*(x)$ of course is not continuous. Since on non-defect sites (which correspond to bottlenecks of size $l = 0$) the transport capacity is $J^* = J_{\text{hom}}^{\max}$, it is sufficient to check condition (3.47) for defect sites. Their number is finite in finite systems but can be infinite in the continuum limit (e.g. for disordered systems with finite defect density).

The problem of condition (3.47) is that it is given as an inequality and does not provide properly defined initial conditions for (3.46) on the defect sites. Now we want to show that (3.47) is identically fullfilled by a set of initial conditions

$$J(x) = J^*(x) \qquad \text{at defect sites } x\ , \tag{3.48}$$

if one assumes additionally that the physical local solution at x is selected by shock dynamics.

First of all, if we assume the conditions (3.48) we see that, in contrast to the boundary conditions of the system which are usually given by a fixed density, the initial condition imposed by a defect provides the possibility of two realizations of the local density profile. Given the initial condition $J(x_0) = J^*(x_0)$ at a point x_0, only the current is a fixed initial condition while, due to the non-unique inversion of the current-density relation (one maximum!), there are two possible values for the density, ρ_H and ρ_L (with $\rho_H > \rho_L$), leading to two possible local solutions of (3.46), a *high density solution* $J_H(x)$ and a *low density solution* $J_L(x)$:

$$J^* \begin{array}{ll} \nearrow & \rho_H \longrightarrow J_H(x - x_0, J^*) \\ \searrow & \rho_L \longrightarrow J_L(x - x_0, J^*) \end{array} \tag{3.49}$$

A constraint on the selection of a physical solution is given by the collective velocity

$$v_c(x) = J'(\rho(x)) \tag{3.50}$$

where $J(\rho)$ is the current-density relation and the prime denotes the derivative with respect to ρ (see Sec. 2.3.3). A solution can only propagate away from the initial point if the direction of v_c is pointing away from it, i.e. left of it only solutions with $v_c < 0$ can exist, while right of it solutions must have $v_c > 0$ [87]. In a system with a single maximum at density ρ_m in the CDR, $\frac{dJ}{d\rho} > 0$ for $\rho < \rho_m$ and $\frac{dJ}{d\rho} < 0$ for $\rho > \rho_m$, thus left of an initial point, only the high density solution J_H can be realized, while right of it only J_L can physically exist. This

[13] This is expected to hold even for larger densities, since in the disordered TASEP corrections are also small for large ϕ.

principle is displayed in Fig. 3.28, top. Hence, each initial condition at a point x_0 can have its own solutions. We denote these *local solutions* by

$$J(x - x_0, J^*) = \begin{cases} J_H(x - x_0, J^*) & \text{for } x \leq x_0 \\ J_L(x - x_0, J^*) & \text{for } x > x_0 \end{cases} . \tag{3.51}$$

Obviously at the point x_0 there can be a downward discontinuity in the density if the profile is physically realized. This indeed is the discontinuity that also is present in the TASEP with a defect. However these kind of discontinuities are no "shocks" as was argued in Sec. 2.3.4. Actually the dependence on J^* can easily be obtained by a shift operation of two functions $\tilde{J}_L(x)$ and $\tilde{J}_H(x)$ with initial conditions $\tilde{J}_L(0) = J_L^0$ and $\tilde{J}_H(0) = J_H^0$, where J_L^0 and J_H^0 are arbitrary chosen values in the high- and low density branch of the CDR. If the range in both branches of the CDR includes $J = 0$, one can simply choose $J_L^0 = J_H^0 = 0$ [14]. Since the ODE (3.46) is of first order and does not explicitly depend on x, the high and low density solutions unambiguously depend on ρ and are monotonic. Thus different local solutions $J_{L,H}$ can only differ by a shift in the variable x. An arbitrary solution $J_{L,H}(x - x_0, J^*)$ can be obtained by shifting $\tilde{J}_{L,H}(x)$ by an amount $\tilde{x}_{L,H}(J^*)$ so that the value of the shifted function at $x = 0$ is equal to J^*. The functions $\tilde{x}_{L,H}(J^*)$ are just the inverse functions of the unique functions $\tilde{J}_{L,H}(x)$. Then the local solutions at a point with initial condition J^* are given as

$$J(x - x_0, J^*) = \tilde{J}(x - x_0 - \tilde{x}(J^*)) . \tag{3.52}$$

The functions $\tilde{J}_{L,H}(x)$ and $\tilde{x}_{L,H}(J)$ can for example be obtained by numerical solution of (3.46) with initial conditions $J_{L,H}^0$.

Selection of the global current profile

The physically realized *global* current profile in the steady state is also determined by shock dynamics [81, 87, 27]. If they are stationary they connect different local steady state solutions of (3.46) to form a *global solution*. The shock velocity

$$v_s = \frac{J_+ - J_-}{\rho_+ - \rho_-} \tag{3.53}$$

determines the propagation of a discontinuity in a (not necessarily stationary) density profile. Here J_+ (ρ_+) is the current (density) right of the shock and J_- (ρ_-) is the current (density) left of the shock. In homogeneous driven lattice gases with a single maximum in the CDR (and no minimum) only upward shocks with $\rho_+ > \rho_-$ can exist ([87, 81]). For local bulk rates ω_a, ω_d vanishing in the continuum limit, the CDR that relates the local density and current is the same as in the corresponding particle conserving system.

Since the source term $s(\rho)$ of (3.45) vanishes in the continuum limit, shocks can only be stationary at intersection points of a high and a low density solution $J_H(x)$ and $J_L(x)$. These points hence can connect two local solutions. So only at these intersection points a switch of the physical realized local solution can occur. Note that local solutions of the same kind J_L or J_H cannot intersect since the differential equation (3.46) is of first order. Since $S(\rho)$, which determines the

[14] Note that this is the case for systems with strict exclusion interaction like TASEP and TASEP-LK. If double occupancy is possible, the CDR not necessarily vanishes for $\rho = 1$.

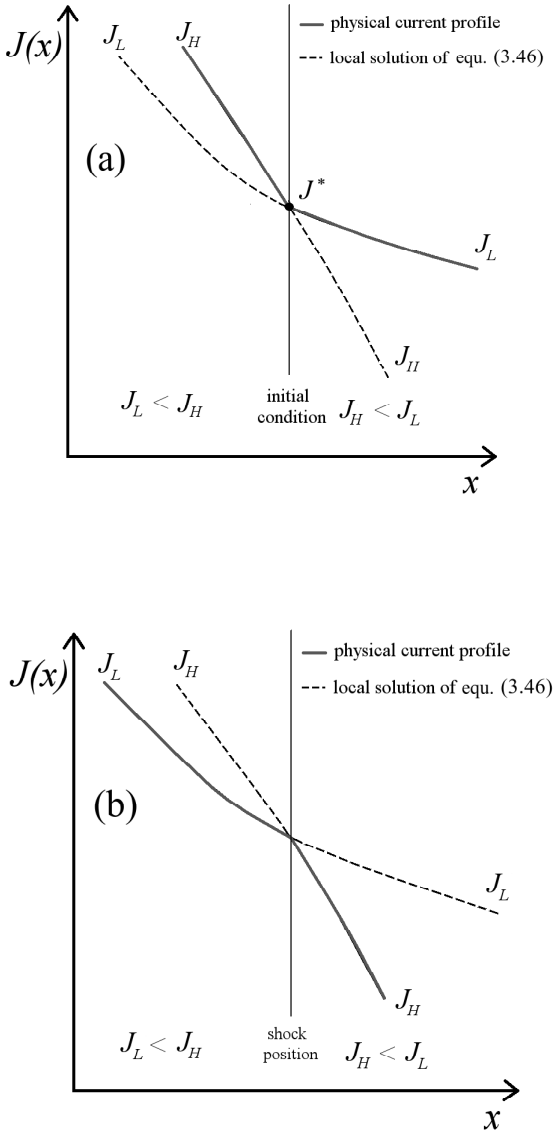

Figure 3.28: (a) Local solutions in the vicinity of a point with an initial condition J^*. Due to the non-unique inversion of the current-density relation, there are two possible solutions. Since for a physical solution the direction of the collective velocity must point away from this position, only solutions with maximal current are realized. (b) Intersection point of local solutions of the density profile. The constraint that only upward shocks can exist implies that only solutions with minimal current are physically realized.

slope of the current profile, is assumed to be a monotonically decreasing function in ρ, we have $S(\rho_H) < S(\rho_L)$, hence the gradient of the high density solution $J_H(x)$ is smaller than the one of the low density solution $J_L(x)$. Therefore left of an intersection point, we have $J_L(x) < J_H(x)$, while right of it $J_H(x) < J_L(x)$. Since J_L is the physical solution left of a shock and J_H right of it, at each point the minimal local solution is the physical one (see Fig. 3.28, bottom). We define the minimal envelope of all the local current profiles as the *capacity field* of the system,

$$\mathcal{C}(x) := \min_{x'} \{J(x - x', J^*(x'))\} \tag{3.54}$$

with defects at the points x'. This function does not depend on the boundary rates. The capacity field is a generalization of the capacity introduced in [79]. Note that the capacity field is not identical with the local transport capacity $J^*(x)$ [15]. For $\Omega_{a,d} \to 0$ the capacity field becomes flat and its value is identical to the global transport capacity of the corresponding particle conserving system. In this case, (3.54) together with the fact that J^* decreases monotonically with bottleneck length yields the SBA for systems without LK with $\mathcal{C}(x) \equiv J^*_{\mathrm{SBA}}$. The local transport capacity can be viewed as the source or "charge" of the capacity field. In this view, the function $\tilde{J}_{L,H}(x - x_0)$, which generates all local current profiles via (3.52), can be called the "Green's function" of the capacity field[16].

Additional conditions on the current profile are given by the boundary rates so that $\rho(0) = \alpha$ and $\rho(1) = 1 - \beta$. Of course the maximum current of the homogeneous system $J^{\max}_{\mathrm{hom}}$ remains an upper bound also in the inhomogeneous system. The capacity field together with the boundary conditions can be used to express the physically realized current profile as

$$J(x) = \min\left[J_\alpha(x), J_\beta(x), \mathcal{C}(x)\right] \tag{3.55}$$

This principle is the generalization of the extremal current principle for the homogeneous TASEP [60]. It provides a tool to obtain the global current profile if it is possible to obtain the local solutions of (3.46) and the local maximum current $J^*(x)$. Indeed the global current profile given by (3.55) identically fulfills the condition (3.47) that the current must always be lower than the transport capacity.

In Fig. 3.29 computer simulations of a system with a few defects are compared with results obtained by the minimal principle. Results from the single-bottleneck TASEP and the homogeneous TASEP-LK are used to check the principle (3.55) and illustrate some features of the TASEP-LK with defects. High boundary rates are chosen, such that the resulting current profile is exactly the capacity field $\mathcal{C}(x)$. For the values $\Omega = \Omega_a = \Omega_d = 0.2$ analytical results for the local current profiles in the continuum limit are available. The analytical results from [27] were used for the reference functions $\tilde{J}_L(x) = \Omega x - \Omega^2 x^2$ and $\tilde{J}_H = -\Omega x + \Omega^2 x^2$ that obey the initial condition $\tilde{J}_{L,H}(0) = 0$ to reproduce the local solutions of (3.46). The transport capacity was obtained in LIBA by results of a TASEP with a single bottleneck. The first three bottlenecks are well separated by a large distance. Here we see that LIBA works very well and the

[15] For example a single defect at site x_d and maximum current J^*_{1def} has a peaked local transport capacity $J^*(x) = J^*_{\mathrm{1def}}\delta(x - x_d)$, while the capacity $\mathcal{C}(x)$ is an extended function.

[16] Though in contrast to a Green's functional the functional relating transport capacity and capacity field is non-linear.

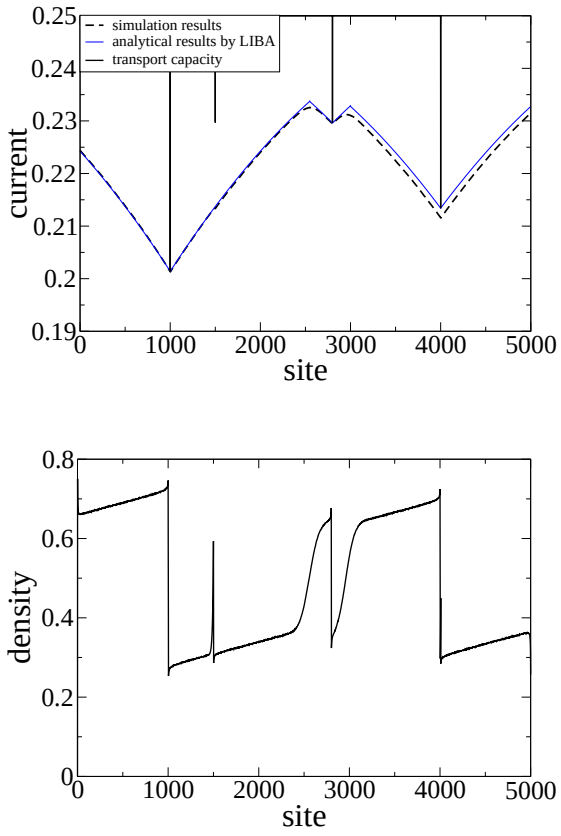

Figure 3.29: Comparison of simulation results and semi-analytical results for the capacity field (= current profile for high boundary rates; here $\alpha = \beta = 0.9$) by LIBA and (3.55). Bottlenecks are at sites x_i (first defect site) with size l_i:
$x_1 = 1000,\ l_1 = 4$
$x_2 = 1500,\ l_2 = 2$
$x_3 = 2800,\ l_3 = 2$
$x_4 = 4000,\ l_4 = 3$
$x_5 = 4008,\ l_5 = 1.$
Further details are given in the text.

current profile is accurately reproduced by the minimal principle (3.55). One observes that at the position of bottleneck 2, the actual current is less than the transport capacity since the local solution of defect 1 is less than $J^*(x_2)$ [17]. For bottleneck 4 there are deviations to LIBA since bottleneck 5 which is quite close to bottleneck 4 (distance = 6 sites) perturbs the transport capacity by further decreasing it. Nonetheless also in this region the minimal principle works if one takes the real transport capacity [18] instead of LIBA.

Local current profiles in the disordered TASEP-LK

We now want to quantify our results by finding the local solutions of the differential equation (3.46) and the continuity equation (3.45), respectively. For a numerical evaluation of these equations the CDR $J(\rho)$ and its inverse $\rho_{L,H}(J)$ are needed.

If there are only few defects in the system we have seen that the CDR is the same as in the homogeneous system, as long as the current is below the maximum current J^*, since the increase of the average density is negligible. Thus in the TASEP-LK with defects we can use the same CDR as in the homogeneous system: $J(\rho) = \rho(1-\rho)$. Therefore the local solutions are the same as the ones of the homogeneous systems.

The situation is different for a finite fraction of defects in the system $\phi > 0$. Then the average density is strongly influenced by the dense distribution of defect peaks which leads to an altered current-density relation even in the non-plateau region [5]. Here we want to find an approximation to calculate the current-density relation for small, but finite, defect density $\phi \ll 1$ if it is not too close to the transport capacity. For that purpose we virtually divide the system into homogeneous subsystems with fast hopping rate p, while the slow hopping bonds connect these subsystems [19]. In first instance we neglect correlations on the defect bonds. The subsystems have an average size $\approx 1/\phi$. In this point of view, the peaks at the defects are the boundary layers of the homogeneous subsystems. Without losing generality, we can assume the system to be in the low density phase and observe the local solution of the right boundary where peaks are concave. This can be transferred to high density solutions by particle-hole symmetry operation. Since $\omega_a, \omega_d \sim 1/L$, we can neglect them for large systems when looking at a single subsystem, thus we can treat them as homogeneous TASEPs. In a large homogeneous TASEP in the low density phase, the density is given by $\rho_0 = 1/2 - \sqrt{1/4 - J}$ in the bulk far from the boundary. We can write the *mass* $m := \sum_{i=1}^{L} \rho_i$ of the system as $m = L\rho_0 + m_p$ with m_p being the mass of the boundary layer. m_p thus corresponds to the mass of a peak in the inhomogeneous system.

We approximate that the mass of the peaks does not depend on distance of adjacent defects. Then we can write the average density as

$$\rho(x) = \rho_0(J(x)) + \phi\, m_p(J(x)), \tag{3.56}$$

[17] One observes a tiny spike at the position of bottleneck 2, which is due to the influence of the density peak on the slope of the current profile at this point, though this effect should vanish in the continuum limit.

[18] The value of the perturbed transport capacity at x_4 can actually be obtained by simulating a TASEP with a bottleneck of length 3 and a single defect at a distance of 6 sites.

[19] This division into subdivision is motivated by the (ISA), though in contrast to ISA each defect separates two homogeneous systems with *fast rates*.

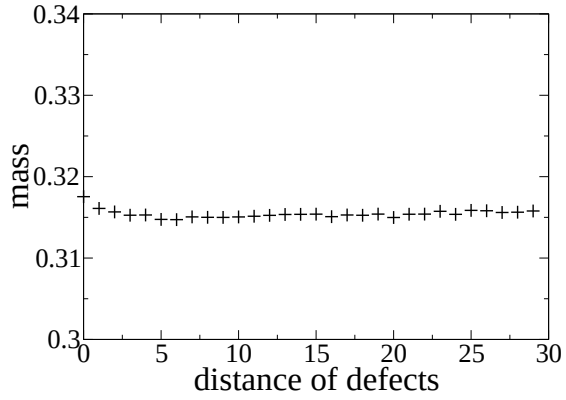

Figure 3.30: Mass $m = \sum_{i=1}^{L}(\rho_i - \alpha)$ of two density-peaks in the low density phase of the TASEP with two defects in dependence on the distance of the defects. One observes that the dependence is rather weak.

since ϕ is the fraction of defect sites. Surprisingly this rather uncontrolled approximation is supported by Fig. 3.30 where the mass in a system with two defects is plotted in dependence on the distance of latter ones.

In this approximation, the mass of the peaks can be calculated analytically, since due to the independence of distance we can take it as the mass of the boundary layer in a large homogeneous TASEP, where exact results are available for given current J. Following [17], the density at a site $L - n$ is given by

$$\rho_{L-n} = JS_n\left(J\right) + J^{n+1}R_n\left(1/(1-\rho)\right) \tag{3.57}$$

with

$$S_n(x) = \frac{1-\sqrt{1-4x}}{2x} - \sum_{j=n}^{\infty}\frac{(2j)!}{(j+1)!j!}, \tag{3.58}$$

$$R_n(x) = \sum_{j=2}^{n+1}\frac{(j-1)(2n-j)!}{n!(n+1-j)!}x^j\,. \tag{3.59}$$

Thus the peak mass is

$$m_p = \sum_n \left[\langle\tau_{L-n}\rangle - \alpha(1-\alpha)\right]\,, \tag{3.60}$$

while the sum is truncated once the terms are small enough.

Equations. (3.56)-(3.60) can be used to calculate the current J for a given density ρ in the low density phase (and in the high density phase by particle-hole symmetry) and vice versa:

$$J(\rho) = (\rho - \phi\, m_p)(1 - \rho + \phi\, m_p)\,. \tag{3.61}$$

This relation can be used to obtain a local solution of the differential equation (3.46) for a given initial condition J_i by iteration. In Fig. 3.31 profiles obtained by this procedure are compared with results from computer simulations.

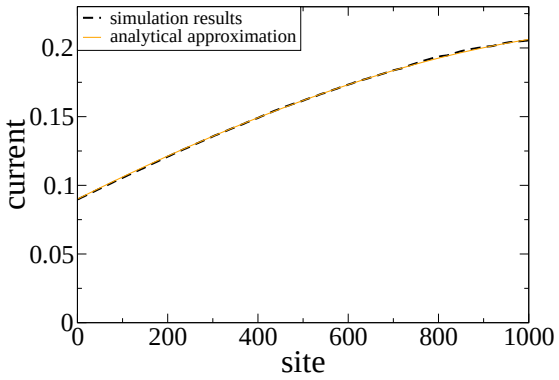

Figure 3.31: Comparison between simulation and analytical results for the current profile in a disordered system with $\phi = 0.2$, $\omega_a = 0.2$, $\omega_d = 0.1$ for entry rate $\alpha = 0.1$ and exit rate $\beta = 0.9$. Since the current is less than the transport capacity throughout the system the profile corresponds to the local current profile of the boundary condition $\rho(0) = \alpha$. One observes excellent agreement between numerical and analytical results. This agreement holds for low current. Deviations occur only if the current comes close to the transport capacity.

One observes an excellent agreement which holds if the current is not close to the transport capacity. Together with the minimal current principle (3.55) the global current profile can be obtained.

The corresponding density profile can be obtained by inverting the CDR with respect to its two branches. Regions with a high density solution of the current profile correspond to a high density domain with the density $\rho_H(J(x))$ obtained by the inverted current-density relation. Analogous to that low density domains exist in regions of low density solutions.

Phase diagram of disordered systems

We now want to investigate the phase diagram of inhomogeneous driven lattice gases. This can be done by identifying intersection points (if present) between boundary solutions and the capacity field. This is illustrated in Fig. 3.32.

If one of the local boundary solutions $J_\alpha(x)$ or $J_\beta(x)$ is the minimum of all local solutions in the whole system (no intersection with other solutions), we have a *low density phase* (L) in the former case and a *high density phase* (H) in latter one and there are no shocks in the system. These phases have the same macroscopic properties like in the corresponding homogeneous system.

If there are intersecting points of local solutions they manifest themselves as shocks in the density profile, separating high and low density regions (phase separation) corresponding to the realized high and low density solutions of the current profile. Phase separation can also be observed in homogeneous systems with Langmuir kinetics like the TASEP-LK [75, 27] and the NOSC model considered in [71, 36]. There the local solutions of the boundaries J_α and J_β can intersect leading to a single stationary shock in the density profiles, separating a low density domain left of it and a high density region right of it. This is called the shock phase (S) [27] which is preserved as long as the minimum local profiles are the boundary current profiles. However, this kind of phase separation dif-

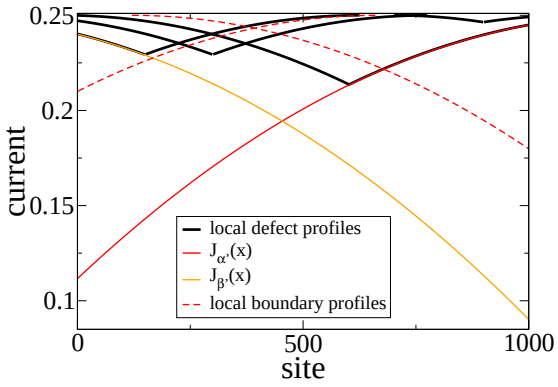

Figure 3.32: Illustration of some current profiles, including critical profiles. We see that the critical rates are related by the critical current profiles: $\alpha^* = \rho_L(J_{\beta'}(1))$, while $\rho_L(J)$ is the inverted (low density) CDR and $J_{\beta'}(1)$ is the local right boundary solution for $\beta = \beta'$. An analog relation is valid for β^*. The bold lines are the local current profiles consistent with the initial conditions imposed by the defects, whose minimal envelope is the capacity field. The thin lines are the critical boundary profiles and the dashed line corresponds to phase separated boundary current profiles.

fers from the phase separation induced by defects which occurs if the boundary profiles $J_{\alpha,\beta}$ intersect $\mathcal{C}(x)$. While in the S-phase the bulk behavior is still determined by the boundary conditions, phase separation due to the finite transport capacity of defects is accompanied by a region where the current is "screened" by the defect(s) and is independent of the boundary condition, i.e. $\frac{\partial J(x)}{\partial \alpha} = 0$ for all x inside this region. If the phase separation is due to the screening by defects we rather refer to a *defect-induced phase separated phase* (DPS). If both boundary profiles $J_\alpha(x)$ and $J_\beta(x)$ are larger than $\mathcal{C}(x)$ in the whole system, the complete system is screened. The current profile is completely determined by the defect distribution and identical to the capacity field $\mathcal{C}(x)$. As argued in Sec. 3.3.1 we call this fully screened phase *Meissner phase (M)*.

Another possible scenario is that the current near the boundaries is only limited by the maximum current of the bulk, i.e. $\mathcal{C} = J_{\text{hom}}^{\max}$ and we have a *maximum current phase* with long ranging boundary layers like in the homogeneous TASEP. However in disordered systems with randomly disordered defects, distances of defects are microscopic and the probability that $\mathcal{C} = J_{\text{hom}}^{max}$ vanishes in the continuum limit.

The phases can be characterized by two quantities:

1. The total length λ_H of high density regions. This is the sum of individual high density regions and corresponds to the total jam length in traffic models [14].

2. The screening length ξ [20], which is the size of the area where the current profile does not depend on the boundary conditions. This is exactly the

[20] This terminology is inspired by the screening length in [79]. Nonetheless, the reader should be alert that in that work the meaning of ξ is different, corresponding to a *maximum* screening length in our terminology

	L	H	S	DPS	M
λ	0	1	$0 < \lambda < 1$ continuous	$0 < \lambda < 1$ continuous	λ_M
ξ	0	0	0	$0 < \xi < 1$ discontinuous	1

Table 3.5: Values and properties of the characteristic order parameters ξ and λ in the different phases. These properties can be used to define phases.

region where the boundary independent capacity field $\mathcal{C}(x) < J_{\alpha,\beta}(x)$ and the local boundary profiles are not the physically realized ones.

In Table 3.5 the behavior of these quantities in the different phases is displayed. Indeed this can be used to *define* the phases. For $\xi = 0$ defects do not influence the current profile and the system is in one of the "pure" phases, L,H or S, determined by the boundary conditions. If $0 < \xi < 1$ there is phase separation and a part of the system does not depend on the boundary conditions, the system is in the DPS-phase. For $\xi = 1$ the complete system is screened and the current profile is solely determined by the defect distribution and the system is in the M-phase. The "pure" phases L,H,S can be characterized by $\xi = 0$ and the vanishing of high density regions (L, $\lambda = 0$), coexistence of high and low density regions (S, $0 < \lambda < 1$), and a global high density region (H, $\lambda = 1$).

The transition from L or H to DPS is marked by a discontinuity in ξ, but it is continuous in λ. Indeed due to the discrete distribution of defects, ξ itself is discontinuous throughout the DPS-phase while λ is not. In the M-phase both ξ and λ are constant, while $\xi = 1$ and λ takes a finite value λ_M that is determined by the fraction of high density regions in the capacity field $\mathcal{C}(x)$ which depends on the individual defect distribution.

We see that at most phase boundaries both quantities ξ and λ are non-analytic. At the transition from S to DPS though λ is analytic; thus it cannot be characterized by λ. Hence for theoretical investigations it appears to be more convenient to use ξ to discriminate defect- and non-defect phases. In simulations it is easier to detect phase separation (see next section) and use the non-analytic behavior of λ to obtain critical points. Due to the analytic behavior between S- and DPS-phase, however, this approach is only applicable at L-DPS and H-DPS-transitions. The S-DPS transition has to be obtained by theoretical considerations.

In particle-conserving systems with defects, i.e. for $\Omega_{a,d} \to 0$, the DPS- and S-phases vanish since no stationary shocks are possible. Here both ξ and λ are discontinuous at the transition to the M-phase. In this case the Meissner phase is equivalent to the bottleneck phase (B).

A sketch of the $\alpha-\beta$-phase diagram of a disordered driven lattice gas with LK is displayed in Fig. 3.33. Attachment and detachment rates are fixed, while here $\omega_d > \omega_a$. L-,H- and even S-phase might vanish for large $\Omega_{a,d}$ if $J_{\alpha=0}(L) > J^*(x_b)$ at some point x_d for any boundary rate α or β, thus phase separation with screening already occurs for vanishing boundary density. The dashed lines mark the phases of the homogeneous system. These pure phases are overlaid by the DPS- and M- phase which are characterized by the critical boundary rates α', β' and α^*, β^*. α' and β' mark the minimal boundary rates at which the respective local boundary profile intersects the capacity field, i.e $J_{\alpha,\beta} > \mathcal{C}(x)$ for at least

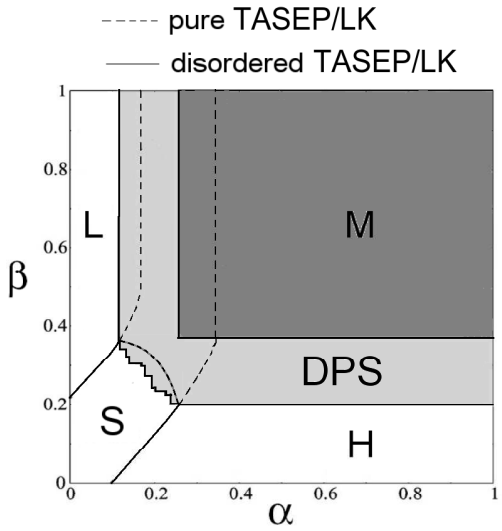

Figure 3.33: Phase diagram of the disordered TASEP-LK for $\Omega_a > \Omega_d$. The critical rates depend on each other as $\alpha^* = \rho_L(J'_\beta(1))$, which is argued in the text. The transition line between S- and DPS-phase is not smooth in the weak continuum limit due to the non-smooth structure of the capacity field (bold line in Fig. 3.32). In the strong continuum limit the DPS phase is concave (bold dashed line). The topology of other disordered driven lattice gases is expected to be the same.

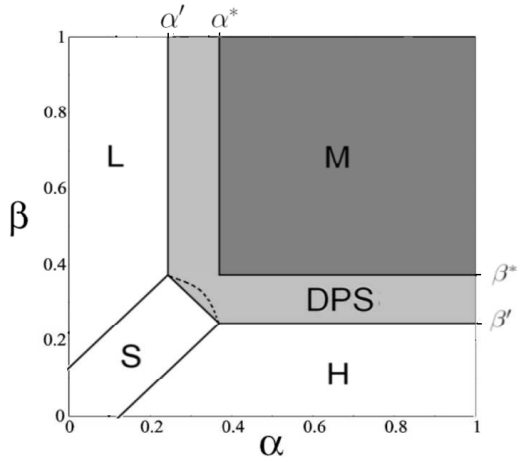

Figure 3.34: Phase diagram of the disordered TASEP-LK with $\Omega_a = \Omega_d =: \Omega$ in the strong continuum limit (see Appendix B). The bold line at the S-DPS-boundary is valid for ϕ scaling as $1/\ln L$ and dashed line (sketched) is valid for finite defect density. The critical rates are given by $\alpha^* = \beta^* = (1-\sqrt{1-q})/2$, $\alpha' = \alpha^* - \Omega$, same for β, with $\Omega = 0.1$, $q = 15/16$. The phase boundaries of the S-phase are of second order. For $\Omega > 1/2$, L- and H-phase vanish.

one point x, while at the rates α^*, β^*, $J_{\alpha,\beta} > \mathcal{C}$ for all x, so that local boundary profiles cannot propagate into the bulk. In Fig. 3.32 some critical current profiles are sketched to illustrate the critical parameters. In parameter regions where J_α and J_β do not intersect, α' and β' do not depend on each other as well as α^* and β^*, hence the phase diagram has a simple structure with phase boundaries parallel to the parameter axes. However, as we can see in Fig. 3.32, α' and β^* do depend on each other since $J(\beta^*) = J_{\alpha'}(1)$. The same relation is valid for β' and α^*. Inside the S-phase, the structure is nontrivial. The phase transition between S- and DPS-phase depends explicitly on the variation of the intersection points of boundary profiles and minimal defect profiles. Explicitly it is given by the condition that a triple points x_t with $J_\alpha(x_t) = J_\beta(x_t) = \mathcal{C}(x)$ exist. One special case for which this condition can be solved exactly is the disordered TASEP-LK for $\Omega_a = \Omega_d$ in the strong continuum limit, if ϕ scales to zero as $\phi \sim 1/\ln L$. In this case the capacity field $\mathcal{C}$ is constant and the transition line is just a diagonal straight line. The phase diagram in the strong continuum limit is derived in Appendix B and displayed in Fig. 3.34. Although this limit is not quite physical it can be used as a reference point to argue that for finite defect densities the S-phase is convex (see also Appendix B).

If we go away from the strong continuum limit, $\mathcal{C}(x)$ is not a constant. The structure of $\mathcal{C}$ is not smooth as was argued in Sec. 3.3.3, so neither is the transition line. In Fig. 3.33 a rather generic sketch of a phase diagram is displayed that incorporates these arguments. Phase diagrams of other driven lattice gases with the properties noted in the Introduction will have the same topology.

3.3.4 Expectation values for phase transitions

As in particle conserving systems, the properties of disordered driven lattice gases with Langmuir kinetics depend strongly on microscopic details of the defect sample. Since we are interested in macroscopic properties that do not depend on microscopic defect distributions, we concentrate on probabilistic quantities of ensembles of systems. One quantity of interest is the expected fraction of systems that exhibit phase separation in an ensemble of systems with identical system parameters and defect density. Here we derive a procedure to calculate this quantity based on analytical results obtained by the principles from the last section.

In order to compare these results with Monte Carlo simulations, virtual probe particles similar to second class particles [7] are introduced that indicate if phase separation occurs in the simulated system. These particles do not change the dynamics of the system. The predicted probability for phase separation is then compared with the relative frequency of phase separation in a set of simulations.

Automated detection of phase separation

We introduce *virtual particles* (V-particles) as probes to identify and distinguish high and low density regions. These particles do not follow the exclusion constraint, instead they can occupy all sites even if these are occupied by particles. The dynamics of the V-particles are the following: At the beginning, a V-particles is put on each defect site. After each lattice update the V-particles

are updated sequentially beginning at the left. Each V-particle hops to the right if there is a particle on its site, while it hops to its left adjacent site if it is residing on an empty site. The V-particle cannot hop over slow bonds, thus if it is on a defect site, it cannot hop to the right, while if it is on a site right of a defect site, it cannot hop to the left. Hence, at any time, there is exactly one V-particle between each pair of contiguous defect sites. If the average density between two defects is larger than $1/2$, the V-particle tends to move to the right, while for $\rho < 1/2$ it tends to move to the left. Thus, a high density region can be identified by a V-particle that is, on average, closer to the right defect. By computing the average distance of a V-particle to the defect right of it, we can identify if there is a high density region in its vicinity.

Using this procedure a large number of simulations can be performed and one can automatically identify whether high and low density regions coexist. This way the relative frequency of phase separated systems and an estimate for the probability of phase separation can be determined.

Analytical approach for phase separation probability

The results from the last subsections can be used in order to derive an analytical approach that allows the determination of the probability that for a given defect density ϕ phase separation occurs. Again we consider ensembles of systems instead of a fixed configuration of defects.

The condition that no phase separation occurs is

$$J_\alpha(x) < J^*(x_b) \quad \text{and} \quad J_\beta(x) < J^*(x_b) \quad \text{for all } x_b. \tag{3.62}$$

The fact that only low density solutions can intersect high density solutions also implies that an increases of α leads to a shift of phase boundaries (in the phase separated phase) to the left while an increase of β moves the phase boundaries to the right. This can be seen in Fig. 3.24.

Following the LIBA we assume that the transport capacity at a position x approximately depends only on the length of the bottleneck at this point; thus $J^*(x) \approx J^*(l(x))$. In a system with binary disorder there are on average $L(1-\phi)$ bottlenecks and the probability that one specific bottleneck has length l is $P(l) = (1-\phi)\phi^l$.

The relation between bottleneck length and transport capacity $J^*(l)$ as well as its inverse relation $l(J^*)$ can be obtained by analytical considerations or numerical computations in single bottleneck systems. The probability that the current is below the transport capacity at a given position x is then

$$P\left[J < J^*\right] = P\left[l < l(J)\right] = \sum_{l'=0}^{\lfloor l(J) \rfloor} P(l) = 1 - \phi^{\lfloor l(J(x)) \rfloor} \ , \tag{3.63}$$

where $\lfloor ... \rfloor$ denotes the floor function.

The probability $\mathcal{P}$ that no phase separation occurs is equal to the probability that the current is below the transport capacity everywhere in the system:

$$\mathcal{P} = \prod_{i=1}^{\langle N_{bn} \rangle} P\left[J(i) < J^*(l(i))\right] = \prod_{i=1}^{L} (1 - \phi^{\lfloor l(J(i)) \rfloor}) \ . \tag{3.64}$$

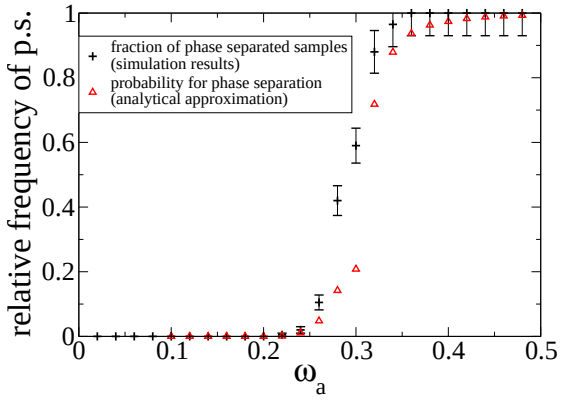

Figure 3.35: Fraction of samples that exhibit phase separation in dependence on the attachment rate ω_a for fixed $\alpha = 0.1$, $\beta = 0.9$, $\omega_d = 0.3$. The system size is $L = 1000$ and each data point is obtained by simulating 200 random defect samples with same system parameters. This is compared with analytical results obtained by (3.64).

Here N_{bn} is the number of bottlenecks from left to right, so $J(i)$ is the current at bottleneck i counted from the left. Since on average there are $\langle N_{bn}\rangle = L(1-\phi)$ bottlenecks, $J(i)$ can be determined recursively by rescaling eq. (3.45) by the factor $1/(1-\phi)$ to obtain

$$\begin{aligned} J(i+1) &= J(i) + \omega_a(1-\phi)(1-\rho(i)) - \omega_d(1-\phi)\rho(i)\,, \\ \rho(i) &= \rho_0(J(i)) + \phi m_p\ . \end{aligned} \tag{3.65}$$

This way the probability for phase separation, which explicitly depends on the system size can be computed iteratively by (3.64), while analytical results for $J(l)$ in the TASEP with a single bottleneck are available by ISA. In comparison to Monte Carlo simulations, this computation can be made with little effort. In Fig. 3.35 ensembles of random defect samples were simulated for different parameter values. The fraction of samples exhibiting phase separation is determined by the method of virtual particles and compared with results obtained by (3.64). One observes a region with a quite steep increase of the probability. The analytical results fit the simulation results quite nicely, although there is a small shift to larger values of ω_a.

3.4 Discussion

In this chapter, inhomogeneous driven lattice gases were investigated. In particular a theoretical framework was developed that allows approximate determination of the maximum current that can be achieved by tuning external parameters (the transport capacity) and effective boundary rates that treat the impact of boundary-near defects by a virtual retuning of boundary rates. The methods are also applicable to determine the structure of the phase diagram of driven lattice gases. Checking the validity of the analytical results, the TASEP (with and without Langmuir kinetics) and the NOSC model (without Langmuir

kinetics) were explicitly considered. However, most results are believed to be generic for a class of ergodic driven lattice gases that obey following conditions:

1. Particle-particle interactions have a finite distance
2. The current-density-relation $J(\rho)$ has a single maximum
3. $S(\rho)$ is a monotonically decreasing function
4. defects correspond to a local decrease of the average velocity

For this approach it was postulated that the transport capacity imposes an upper bound to the current. In systems with Langmuir kinetics this quantity is a local upper bound for the current and provides initial conditions for the current and density profiles in the continuum limit which obey the differential equation (2.26). Each initial condition provides an individual solution to (2.26). The physically realized global profiles hence follow a minimal principle selecting the minimal envelope out of all local solutions. The structure of the phase diagram can be determined by identifying the dominant, i.e minimal local solutions. Phases are distinguished by the dependence on the boundary conditions, which vanishes for high values due to screening by defects. Observations in the TASEP and effects described below indicate for low defect densities that the local transport capacity is predominantly determined by the length of consecutive stretches of defects (*bottlenecks)* present at a given point in the system, while interactions with other defects in its vicinity act as small perturbations.

For vanishing Langmuir kinetics the minimal principle reproduces the single bottleneck approximation (SBA) that was investigated in Sec. 3.2. It states that the (global) transport capacity can be approximated by neglecting all defects except the longest bottleneck. This way one can rely on analytical results obtained in Sec. 3.1. The performance of the SBA method was checked not only by numerical simulations, but also a criterion for the validity of the SBA was found that distinguishes if the influence of other defects to SBA can be treated perturbatively. It was shown that at least a first order perturbative expansion can be applied if the bottleneck-bottleneck interactions (in terms of their influence on the transport capacity) are small enough (equation (3.41)). This property can be tested by numerical simulations of a system with two bottlenecks at different distances. In case of the disordered TASEP the first order expansion yields accurate results. Since systems with Langmuir kinetics locally behave like the corresponding particle conserving systems, it can be assumed that this criterion can be generalized to check the validity of the LIBA in non-conserving systems like the TASEP-LK.

While defects far from the boundaries do not have significant impact on the current as long as it is below the transport capacity, an effect on the current is observed if defects are near the boundaries (*edge effect*). In the non-bottleneck regime, one observes a negative edge effect with lower current due to these defects. Since the effect is short ranged in the continuum limit, boundary-near defects do not have to be treated explicitly, but their effect can be taken into account by virtually replacing the boundary rates by *effective* ones. This does not affect the qualitative phenomenology of the system. An expectation value for the edge effect can be obtained by a perturbative expansion similar to the one used to determine the transport capacity. Knowledge of both the functional behavior of the transport capacity and effective boundary rates can in principle

reproduce the full phase diagram and large scale phenomenology of disordered driven lattice gases.

Both the SBA and the concept of effective boundary rates relate average quantities of disordered systems with the corresponding ones in systems with one or two bottlenecks, i.e. bottleneck-bottleneck interaction. While generic analytical results of bottleneck-bottleneck interactions in most driven lattice gases are pending, numerical results of single- and two bottleneck systems in these cases can be the basis to obtain the corresponding values of disordered systems. By a virtual segmentation of the system, however, for the TASEP it was successful to developed a (semi-) analytical approximation scheme [21] to determine transport capacity and effective edge effect of single bottleneck systems (*interacting subsystem approximation (ISA)*). Foulaadvand et al. [30] could extend this method to systems with two single defects.

The models investigated in this chapter are relevant for modeling gene translation on single mRNA strands (Sec. 3.1) and active intracellular transport by motor proteins on single cytoskeletal filaments in presence of impurities that impede movement of motor proteins. Both the protein production rate as well as the delivery rate of vesicles are determined by the current of molecular motors, ribosomes and cytoskeletal motor proteins respectively. Therefore the transport capacity marks the optimal performance of these systems. Knowledge of the dependence of the transport capacity on external parameters hence appears to be a biologically relevant issue.

As remarked in Sec. 2.1, microtubules constitute a rather radially ordered network and are usually not crosslinked. In this case a single filament description can be appropriate to extract transport properties of the cell (e.g. for rates of secretion of proteins transported on microtubules) since vesicles on different filaments only rarely interact mutually. Actin filaments in contrast constitute highly connected disordered networks [2], where vesicles on different filaments might interact at crossing points. Transport networks of this kind will be considered in the following chapter.

[21] The ISA method maps the problems analytically on finding a root of a polynomial. However for higher order polynomials (corresponding to longer bottlenecks), this task has to be performed numerically.

Chapter 4

Active transport on inhomogeneous filament networks

The model presented in Sec. 3.3 only accounted for interactions of particles travelling on the same track while particles in its environment were treated by an effective particle reservoir controlling attachment and detachment of vesicles by a fixed density. In the context of active intracellular transport, this view seems to be appropriate if one only accounts for *freely* diffusing vesicles in the environment of a filament. Actin filaments though constitute highly connected networks exhibiting crossing filaments. Considering vesicles travelling on different filaments, interactions between them might lead to non-trivial behavior that cannot be taken into account by the (non-interacting) particle reservoir. Interactions can arise e.g. when vesicles travelling on two different filaments encounter at an intersection at the same time. Since both particles are bound, treating one of them by an effective reservoir is insufficient.

Even if filaments itself are homogeneous, the structure of the network might be disordered leading to different behavior compared to networks exhibiting a regular structure. Actually intersections in networks can also be seen as defects where crossing particles inhibit each others movement. Nonetheless, this kind of hindering mechanism does not appear to be accounted for by merely introducing decreased hopping rates in models.

This chapter will introduce a model for vesicular transport on 2D actin networks. The model is motivated by transport of vesicles by myosin on the quasi-two-dimensional cortical actin networks backing the cell membrane. It is implemented in continuous space. Following basic principles of actin growth dynamics, a network of filaments with discrete binding sites for particles is generated and the dynamics of particles travelling on this network is studied. In the first section, the model is introduced and phenomena arising due to hard core interaction between actively driven particles are investigated, while periodic boundary conditions are applied. The main interest will be on the distribution of particle clusters that correspond to high density domains observed in front of defects in single track systems as were considered in the last chapter. The results are compared with transport on a regular network to identify the influence of

random disorder in the network structure on clustering features. In the second section confining boundary conditions are introduced, mimicking the topology of a cell, that break the translation symmetry. This yields non-trivial effects on the network structure and hence particle dynamics. In particular a bias of particle dynamics due to boundaries is observed that significantly reduces travelling times of vesicles on the endocytic pathway. Though the model is in 2D, an analytical treatment suggests that this effect is also present for transport in 3D confined geometries, e.g. on actin networks in the cell lumen.

4.1 Cluster formation in 2D transport networks

In this section a model of filament networks in continuous space is proposed. Particles perform diffusive movement in space but can also attach to filaments to perform directed movement along them. The network itself is generated by stochastic dynamics motivated by growth dynamics of actin filaments following the processes described in Sec. 2.1.3, yielding a disordered structure. Being effectively two-dimensional, the cortical actin network of eukaryotic cells [84] can be modeled by these dynamics.

In Sec. 2.4 previous results for transport networks were presented. These show that the active components of the system enhance diffusive dynamics [53], while inhomogeneous network structures were shown to result in inhomogeneous particle distributions [73]. Additional attractive interactions in these networks can induce condensation phenomena [72]. These results show that the structure of a transport network strongly influences transport properties. In order to model active transport on actin filament networks, it is therefore necessary to consider realistic network structures.

As we have seen in the last sections transport systems like the TASEP can exhibit high density domains at defects if the particle current is larger than the transport capacity. Since particles on crossing filaments can hinder each others movement, intersection points show some characteristics of defects in single filament systems. This situation is similar to car traffic in cities. There cars cannot move freely over intersections but other cars trying to cross the same intersection hinder movement. This effect can cause traffic jams at intersections that correspond to clusters of cars [15]. We therefore expect the possibility of queuing of particles at intersections leading to an aggregation of particles in form of clusters.

For many biological processes, concentration gradients are crucial. One example is the aggregation of proteins inside the cell or in the cell membrane. Clusters of aggregated proteins can be observed and characterized experimentally for example by high resolution fluorescence microscopy [90]. In some cases these clusters are essential for cell functionality but they can also lead to dysfunctions or even apoptosis. In yeast cell membranes for example one observes the aggregation of Erd2p-receptors which can promote the internalization of toxins [11]. Most recent works on membrane protein aggregation considered an attractive interaction between proteins as source for (reversible) aggregation [18, 90, 31]. For this kind of particle dynamics, the resulting clusters are governed by a well defined size scale.

Jamming in vesicular transport may yield an alternative aggregation mechanism of proteins. Vesicles, transported on different filaments can block each

other at filament crossing points, inducing queuing of vesicles. The existence of a quasi two-dimensional irregular actin filament network beneath the membrane [2, 9] suggests jamming of vesicles prior exocytosis, resulting in receptor clusters on the membrane surface. In this case large scale features of cluster distributions can vary from diffusion limited aggregation. The limits of resolution in optical microscopy [89] make it difficult to distinguish clustered single receptors in-vivo. By contrast, the size of larger particle aggregates can in principle be given with relatively high precision [90]. Therefore it is useful to relate the cluster size distribution with microscopic transport mechanisms by means of theoretical modeling.

The focus of this section will be on particle configurations in order to identify the formation of clusters and the investigation of cluster size distributions. The results[1] are compared with a regular network in diffusive environment and a diffusion limited model where attractive particle-particle interactions promote cluster formation. The main focus will be on robust properties of clusters that serve as criteria to discriminate between different microscopic dynamics.

4.1.1 Network models

In the following, stochastic models for active transport on 2D networks embedded in a diffusive environment are introduced. At each time step N particles within the system area L^2 are randomly chosen and updated (random sequential update) according to the rules given in Tables 4.1-4.3 applying periodic boundary conditions. Time steps are normalized such that on average each free particle performs one diffusive step per time step Δt. Results are discussed for different *particle densities* $\rho_p^0 := N/L^2$ which, by biological reasons, is chosen as $\rho_p^0 = 0.04$ if not stated differently (see Table 4.4) .

Regular networks

As a the first example for active transport on networks, a discrete lattice gas model with a square network of active stripes, similar to the model investigated in [53], is considered. $N \times N$ sites are arranged in a square lattice of edge length $L = N\Delta x$ where Δx is the lattice spacing. We distinguish the particle states *attached*(A) and *detached*(D). Detached particles always move diffusively. The system contains stripes of *active* sites that constitute a regular square transport network. If particles are located at an active stripe, they can attach (if not yet attached) or detach (if attached). Attached particles perform a directed motion along stripes. The orientation of stripes was chosen randomly with equal probability. As in the last chapter, the exclusion principle is applied, hence steps that would result in double occupation of a site are prohibited due to exclusion.

Compared to the dynamics of non-interacting self-driven particles qualitatively new features arise due to the steric particle-particle interactions at intersections of the network. Here an additional parameter is introduced, the *blocking probability*: If at least two particles are at sites adjacent to an intersection site, each particle may only access the intersection site with the probability $1 - b$ (cf. figure 4.1). Particles on intersection sites retain their moving direction.

[1] Results of this section are available on [37].

Process	Particle state(s)	Description	Probability
Diffusion	D	Detached particles move to sites randomly chosen from the four neighbors	$\omega_D = 1$
Forward Step	A	Attached particles move to the next site in forward direction of filament	$p = 0.5$
Attachment	D→A	Detached particles on filament sites becomes bound	$\omega_a = 0.25$
Detachment	A→D	Attached particles become detached	$\omega_d = 0.02$
Blocking	D	Forward movement of particles adjacent to intersection sites is inhibited if other particles occupy sites adjacent to intersection	$b = 1$

Table 4.1: Brief prescription of the dynamic processes in the square lattice model. Column 2 displays the particle states "attached"(A) and "detached"(D). The right column displays the probability that the respective process occurs within one time step. Numerical values given in the right column are default values which are used if not stated else and are chosen to fit the ones in [53]. System size $N = 200$, mesh size $a = 10$ sites.

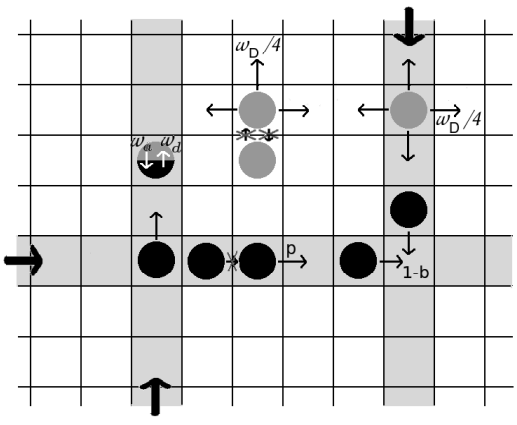

Figure 4.1: Illustration of the dynamics in a regular network. Dark gray discs are particles diffusing freely with rate ω_D. Black discs represent attached particles that can only step in the preferred direction of the active stripe they occupy (bold arrows) with rate p. On filament sites (light gray), particles can interchange between attached and detached state with rates ω_a and ω_d, respectively. Crossed arrows denote steps that are inhibited due to the exclusion principle.

The explicit rules for the particle dynamics are displayed in Table 4.1 and illustrated in figure 4.1. The default parameter values have been chosen analogously to [53] $\omega_D = 1$, $p = 0.5$, $\omega_d = 0.02$ and system size $N = 200$. In [53] the attachment rate is equal to one, which corresponds to an effective attachment rate $\omega_a = 0.25$ if a particle is on an adjacent non-active site[2]. To be consistent with the subsequent continuous space model, we choose $b = 1$.

Inhomogeneous networks

Generalizing to continuous space and allowing for arbitrary directions and lengths of active stripes, a continuous model with randomly generated linear filaments is presented where hard-core particles can perform directed paths along these filaments. The model is motivated by actin filament dynamics introduced in chapter 2, though only basic mechanisms that are essential for a random network structure are considered.

General properties of the model The main components of our model are filaments and particles interacting via a spherical hard-core potential represented by a disc of radius r_p. This hard core potential is implemented by cancelling any steps that would result in an overlap of discs and corresponds to exclusion in discrete models. Filaments are represented by linear sequences of subunits with length d_s. They are directed with a *minus-end* at which they can shrink and a *plus-end* at which new subunits can be generated to elongate the filament. Particles can attach to binding sites at each subunit that are within a distance less than d_b [3] and perform steps to adjacent subunits in the plus-direction of the filament.

Dynamics of filaments and particles The filament network is generated by stochastic dynamics, updating network configurations by the processes commented in Table 4.2 and illustrated in Fig. 4.2. Since the model is motivated by the dynamics of actin filaments, some additional parameters originating from the biological processes presented in Sec. 2.1.3 are included.

The quantity ρ_{ARP} introduced in Table 4.2 represents the density of free $ARP2/3$-*complexes* that serve as nucleation and branching seeds for filaments, while the actin density ρ_{act} corresponds to the density of free (actin-) filament subunits constituting the filaments. Their initial values are ρ^0_{ARP} and ρ^0_{act} which corresponds to the case if all monomers are dissociated. The densities decrease with the growing filament network as shown in Fig. 4.3. After 5000 steps a stationary actin density is reached. We assume that also the structure of the network is stationary and in qualitative agreement with a real actin network. Network dynamics are therefore stopped at this point. Since in the stationary state association and dissociation of subunits must balance, $\omega_g \rho_{act} \approx \omega_s \Rightarrow \rho_{act} \approx \omega_s/\omega_g$ [4] (cf. [2] for actin networks).

After construction of the network, particles obeying the exclusion principle are fed into the system at random positions. As mentioned above, the particle positions are updated following a random sequential update scheme, whereby the

[2] In contrast to [53], crossing of active stripes by diffusion is allowed.

[3] The binding involves a hopping of the particle such that the center of the particle is exactly on the binding site of the subunit.

[4] The contribution of filament nucleation can be neglected for average filament lengths $\gg 1$

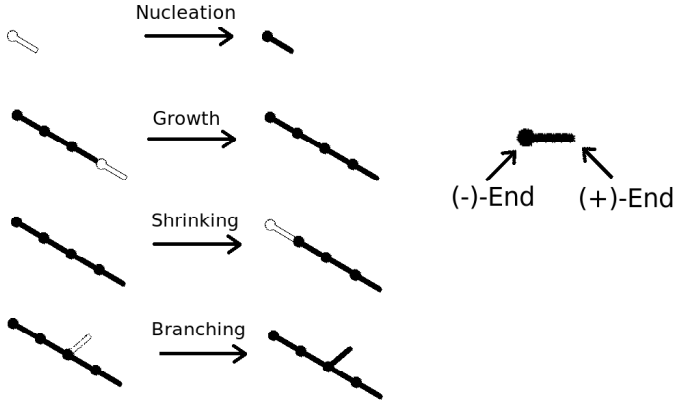

Figure 4.2: Illustration of the filament dynamics. Filaments are implemented as sequences of subunits (small dots, corresponding to actin monomers) separated by a distance d_s (short bars). Filament subunits are polarized, with a plus-end where subunits are created to elongate, and a minus-end where subunits dissociate causing shrinking.

Process	Description	Probability
Nucleation	Initialization of filaments with arbitrary direction at an arbitrary point in the system. The minus-end receives a cap inhibiting shrinking.	$\omega_n\, \rho_{act}\, \rho_{ARP}$
Branching	New filaments are initialized at an existing one (not necessarily the plus-end; angle between parent filament and branch=70^o[68].	$\omega_b\, \rho_{act}^2\, \rho_{ARP}$
Growth	New subunits are generated at the plus-ends. of filaments	$\omega_g \rho_{act}$
Shrinking	Subunits are removed at the minus-end of filaments if the end is not capped.	ω_s
Uncapping	Caps are removed.	ω_u

Table 4.2: Dynamics of the filament network.

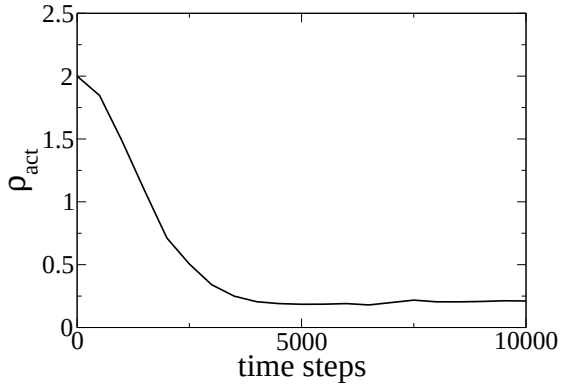

Figure 4.3: Density of free actin ρ_{act} in dependence on time. After 5000 time steps a stationary state is reached.

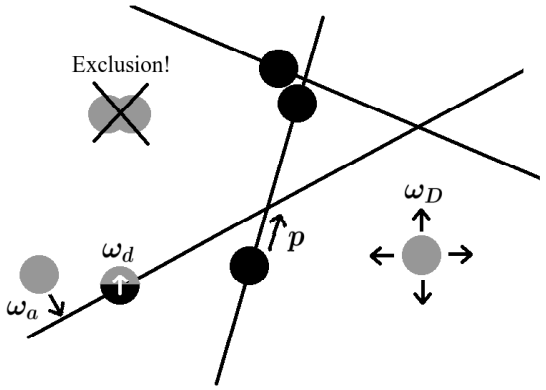

Figure 4.4: Illustration of the particle dynamics in an inhomogeneous network. Dark gray discs are free particles, black discs represent particles attached to filaments stepping to adjacent subunits (distance d_s) with rate p. Particles can attach to filaments with rate ω_a if they are within the binding distance d_b and detach with rate ω_d. Overlapping is inhibited due to exclusion.

Process	Particle state(s)	Description	Probability
Diffusion	D	Detached particles move in a random direction. Step widths are uniformly distributed between 0 and $2l_D$	$\omega_D = 1$
Step	A	Attached particles move to adjacent subunit in plus-direction.	p
Attachment	D→A	Particles bind to subunits if their distance is less than d_b, becoming 'attached'	ω_a
Detachment	A→D	Particles detach	ω_d

Table 4.3: Particle dynamics. A='attached'; D='detached'

particle-particle as well as the interactions between particles and the generated static network are considered. Like in the regular network model, particles can freely diffuse in the 'detached' state and perform directed movement in the 'attached' state. The rules of the particle dynamics are described in Table 4.3 and illustrated in Fig. 4.4. On single filaments away from intersections, the dynamics is similar to that of driven lattice gases described in the last chapters.

Although no particular biological system is considered, parameters are chosen to fit the typical order of magnitude in real vesicular transport. If not stated differently, default parameters as displayed in Table 4.4 are used for our simulations. The referenced works used experimental and modeling techniques to obtain the data given in the third column. For particle dynamics, the parameters are chosen to be consistent with the discrete model introduced in the last section relying on the model in [53].

Parameter name	Reference	Reference Value	model parameters
Filament dynamics:			
nucleation rate ω_n	[10]	$8.7 \times 10^{-5}\,\mu M^{-2} s^{-1}$	$1.0 \times 10^{-5}\,lu^{-6} tu^{-1}$
growth rate ω_g	[10]	$8.7\,\mu M^{-1} s^{-1}$	$0.5\,lu^{3}\,tu^{-1}$
shrink rate ω_s	[8]	$4.2\,s^{-1}$	$0.075\,tu^{-1}$
branch rate ω_b	[10]	$5.4 \times 10^{-4}\,\mu M^{-3}\,s^{-1}$	$0.0001\,lu^{9}\,tu^{-1}$
uncap rate ω_{uc}	[10]	$0.0018\,s^{-1}$	$0.0001\,tu^{-1}$
actin density ρ^0_{act}	[84]	meshsize: $0.1 - 1\,\mu m$	$2\,lu^{-3}$ [1]
ARP2/3 density ρ^0_{ARP}	[32]	$0.1\,\mu M$	$0.1\,lu^{-3}$
Particle dynamics:			
particle radius r_p	[59]	42.5 nm (average)	0.5 lu
binding distance d_b	[53]	1 site (50 nm)	0.5 lu
subunit distance d_s	[2]	36 nm	0.36 lu
attachment ω_a	[53]	1/4 of diffusive steps	0.25 tu^{-1}
detachment ω_d	[53]	$0.8\,s^{-1}$	$0.02\,tu^{-1}$
diffusive step length l_D	[53]	1 per time step	0.5 lu
step rate p	[53]	$20\,s^{-1} \Rightarrow v = 1\,\mu m/s$	$0.75\,tu^{-1}$
particle density ρ^0_p	[33]	10-60 vesicles in bud ($\sim$0.75 μm radius)	$0.04\,lu^{-3}$

Table 4.4: Default parameters of the model which are biologically motivated by transport of vesicles by myosin on actin filaments. The referenced values are either based on experimental data or existing models for intracellular transport [53] and filament dynamics [32]. Model parameters are chosen to be in the order of magnitude of referenced values, fitted to time and space scale of the simulations. Length scale: $1\,lu = 100nm = 2r_p \Rightarrow 1\,\mu M = 0.6\,lu^{-3}$. *Time scale:* $1\,tu = \Delta t = 0.025\,s$. *By default square systems of system length* $L = 200\,lu$ *and a layer thickness of* $1\,lu$ *are considered. In theoretical considerations the layer thickness however is neglected and the system is treated two-dimensional.*

[1] The parameter ρ^0_{act} was adjusted such that the mesh size is in the order of magnitude as in the referenced work.

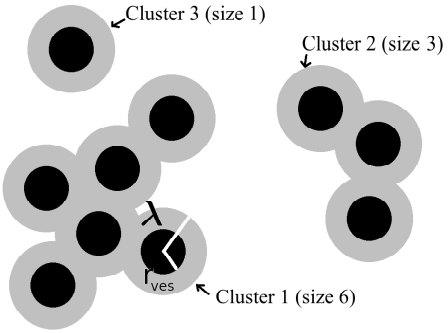

Figure 4.5: Illustration of particle clusters. Black discs represent particles, while gray discs are the λ-neighborhoods of each particle. Connected gray areas are clusters; the size of a given cluster is the number of particles on it.

4.1.2 Numerical results

Characterization of Clusters

As already mentioned in the introduction we aim to relate the microscopic particle dynamics to the size distribution of their aggregates. In this subsection the definition of clusters is discussed for the different model systems.

Clusters are groups of particles that are connected by overlapping neighborhoods. We therefore introduce the $\lambda-$*neighborhood* of a particle representing a disc of radius λ around the center of the particle. A cluster is defined as a set of particles included in a connected area of $\lambda-$neighborhoods (cf. Fig. 4.5). If continuous space variables are used, there exists no natural scale which identifies two particles as neighbors. We therefore have to specify the value of λ. In order to extract relevant results, λ is chosen such that qualitative results are robust on variation of λ. If not stated differently we choose $\lambda = 2r_p$, which turns out to meet this condition (cf. fig 4.20).

In lattice models, static particle clusters are usually considered as connected sets of adjacent particles. However, this definition is not appropriate in this context since clusters move by propagation of vacancies. Therefore particles separated by a single vacancy are considered as belonging to the same cluster.

Our main interest is in ensemble and time averages of *cluster size distributions (CD)* and their asymptotic behavior. CDs display the relative frequency of cluster sizes emerging in the system. If not stated differently it was averaged over 50000 time steps within individual runs, evaluating cluster distributions in distances of 500 time steps, taking an ensemble of 100 samples.

Clustering also occurs for random particle configurations. In Fig. 4.6 and 4.7 cluster size distributions of random configurations in discrete and continuous space are displayed for different particle densities. Here the density ρ_p^0 is the particle number per area unit which corresponds to $(2r_p)^2$ in continuous space and one site in the lattice model. If densities are not too large, the formation of large clusters is impeded resulting in an exponentially decaying cluster size distribution. For high densities one observes a narrow peak at the right end. At these densities clusters spanning the whole system emerge. In order to rule out these kinds of random clustering we only consider densities below the regime of

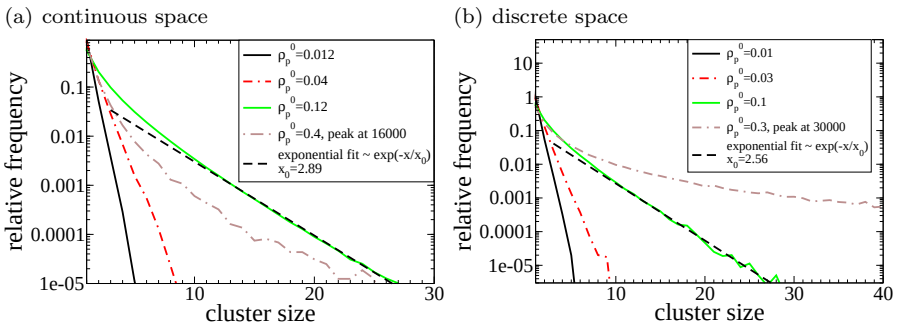

Figure 4.6: Cluster size distributions of random particle configurations in dependence on the particle density. For low densities the CD decays fast with a short size-scale. For large densities clusters on large size-scales and even such that span the whole system emerge (not visible in figure since on too large size-scale).

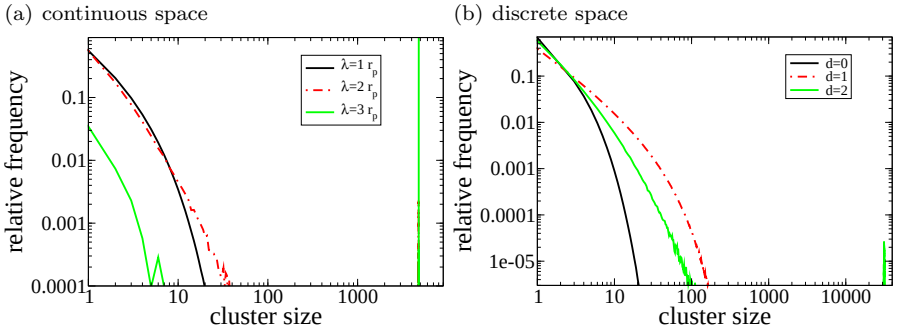

Figure 4.7: Cluster size distributions of random particle configurations for different coarse graining scales. λ is the radius of the environment as defined in section 4.1.2, while d represents the maximum distance (number of vacancies) allowed between two particles connecting a cluster. One observes that for large coarse graining scales clusters spanning the whole system emerge.

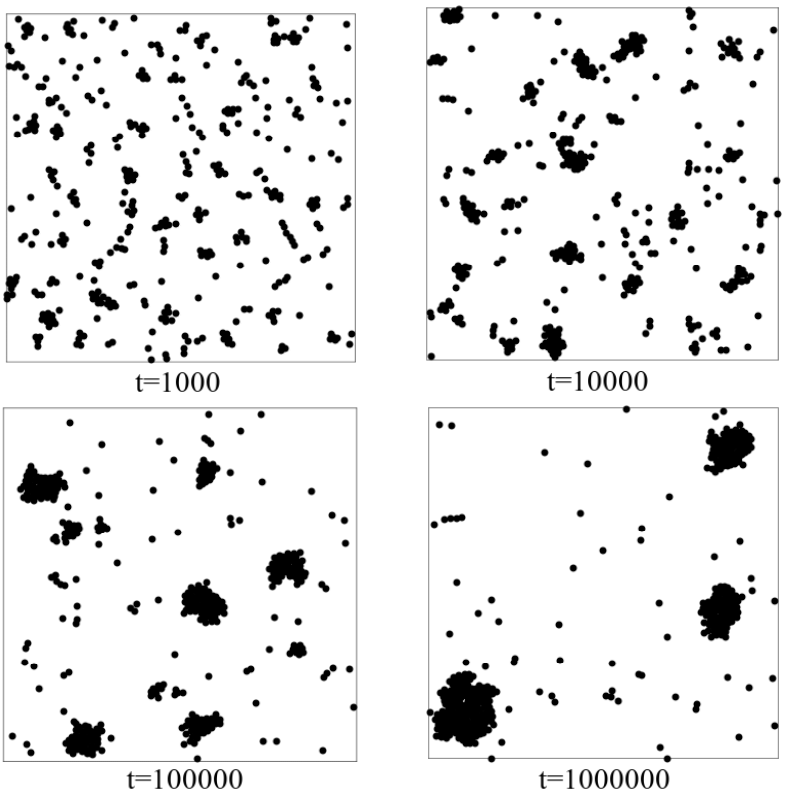

Figure 4.8: Configurations of particles (black discs = particle neighborhoods with radius $\lambda = 2\,r_p$), exhibiting a mutual attractive interaction. Snapshots at different times for $V_0 = 2, d_V = 3.5$, $\rho_p^0 = 0.04$, $L = 200$, $\Delta t \hat{=}$ 0.025 sec. One observes that already at small times clusters form and for long run times the number of clusters decreases, while the average size of cluster increases.

spanning clusters at relevant scales λ. Here we are interested in cluster formation mechanisms beyond random clustering.

In the following, we will focus on particle configurations and cluster size distributions in several transport models.

Aggregation without network

As a first reference a diffusion limited aggregation model similar to the one introduced in [18] is investigated[5]. Omitting filaments, we can use a variant of our model to mimic freely diffusing particles with an attractive interaction. The corresponding process can be formulated as an equilibrium model consisting of diffusing hard-core particles (radius $r_p \hat{=} 10\,nm$; within the size-scale of membrane proteins [90]) interacting via an attractive potential. We apply the particle dynamics discussed in Sec. 4.1.1 but do not consider filaments. In addition a particle-particle interaction is introduced realized by a square well

[5]Here however, no additional long range repulsive force is assumed.

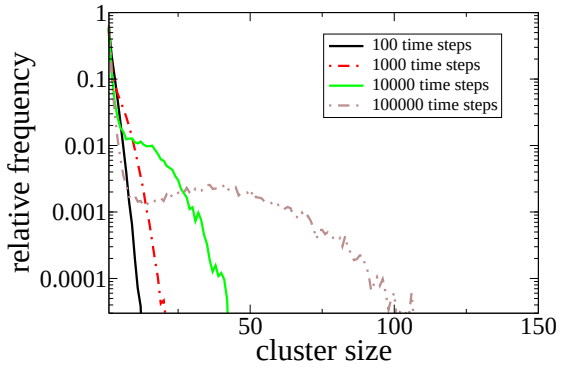

Figure 4.9: Cluster distributions in dependence on the runtime in a system without network but attractive square well interaction potential. Parameters are $V_0 = 3, d_V = 3.5$, $\rho_p^0 = 0.04$, $L = 200\, r_p$, average over 200 runs. A maximum establishes, that moves slowly towards larger scales.

potential of the form

$$V(\mathbf{x}-\mathbf{x}') = \begin{cases} -V_0 & \text{for } |\mathbf{x}-\mathbf{x}'| \leq d_V \\ 0 & \text{for } |\mathbf{x}-\mathbf{x}'| > d_V \end{cases} \tag{4.1}$$

where $\mathbf{x}, \mathbf{x}'$ are particle positions. This potential can be implemented using a acceptance probability $p = \min(e^{-\beta(V(x_{n+1})-V(x_n))}, 1)$ (β =inverse temperature) for a step from x_n to x_{n+1} (n denotes the time index). In the following we use dimensionless quantities and put $\beta = 1$. The default parameters are $V_0 = 2, d_V = 3.5 r_p$ and particle density $\rho_p^0 = 0.04$. Assuming a diffusion constant for membrane proteins $D \approx 0.0025\,\mu\text{m}^2/\text{s}$ [98] we choose a time step corresponding to $\Delta t = 0.02$ seconds such that one diffusive step of length $l_D = r_p = 10\,nm$ is performed per time step Δt.

In Fig. 4.8 typical particle configurations at several runtimes are displayed, while in Fig. 4.9 ensemble averages of cluster size distributions are shown. Initial clustering already occurs on a rather small time-scale. Regarding the particle configurations we see that the number of clusters decreases with increasing runtime while the average size of remaining clusters increases. This is due to diffusion and merging of existing clusters after long times. Movement of large clusters is strongly suppressed, so that merging occurs quite slowly. The coarsening process can also be observed in the cluster size distribution: One observes a characteristic scale for larger clusters, manifesting in the emergence of a maximum, indicating a characteristic scale for cluster sizes. The dominant clusters are always within the same size-scale which increases with time.

Since the cell membrane changes its structure steadily, patterns arising at time-scales corresponding to a finite fraction of a cell cycle cannot be assumed to be in a stationary state. Computing time averages we therefore focus on intermediate times and fix the averaging interval starting at 20000 time steps (corresponding to ∼7 minutes in real time) after random initialization of particles and ending at 30000 time steps. The time interval lies in the transient regime for default parameters. Within this interval cluster size distributions were computed (time and ensemble averages, 200 samples) for different parameter regimes and displayed them in figure 4.10. One observes that for weak

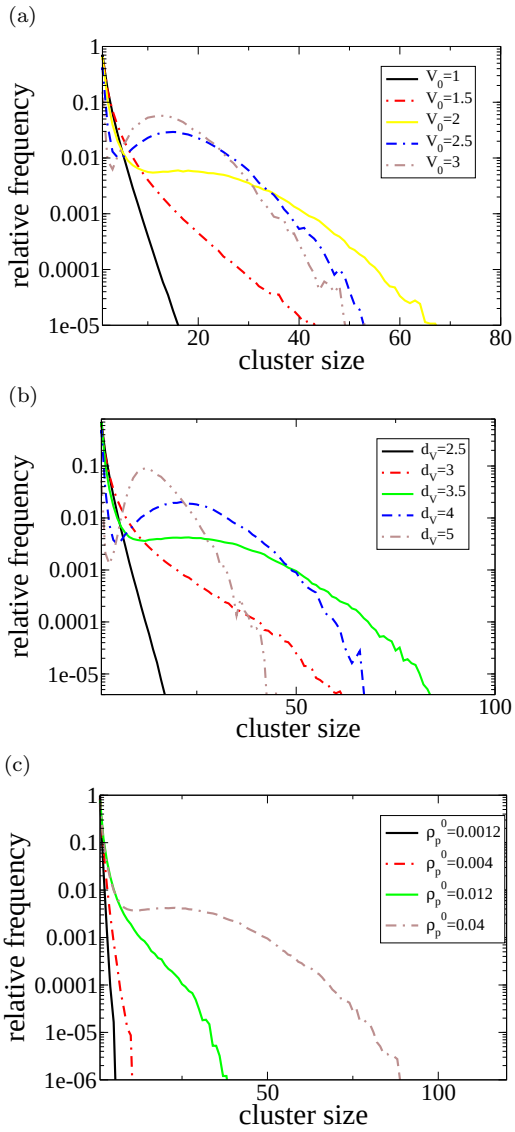

Figure 4.10: Plots of cluster distributions in the attractive particles model at intermediate times ($t = 20000 - 30000$ time steps) in dependence on the potential depth V_0 (a), the potential width d_V (b) and particle density ρ_p^0 (c). One observes the transition from an exponential decay (non-clustering phase) to the formation of a maximum, corresponding to clusters at this size-scale (condensation). Default parameters are given in the text.

interaction no significant clustering occurs, manifesting in an exponentially decaying CD, while for strong interaction V_0, including the default parameters, a maximum emerges, hallmarking the formation of clusters.

One has to emphasize that for this kind of dynamics, clustering is reversible, i.e. in general particles can detach from a cluster due to thermal fluctuations and move to another one, such that non-vanishing particle currents between clusters may be present. This is in contrast to the irreversible clustering process discussed by Meakin and Family [67] where a power law distribution of clusters was found at transient times[6]. The interaction mechanism proposed in [31] however indicates a finite strength of protein-protein attraction so that thermal fluctuations allow detachment of particles. Destainville introduced an aggregation model claiming an additional long range repulsive force that stabilizes clusters such that a stationary state with a characteristic cluster size scale is reached [18]. Here we see that at transient times, that might be more relevant for cell membrane dynamics, this intrinsic size scale is present even without a long range repulsive force

Directed transport on regular networks

Features of particle configurations and cluster distributions are examined in the model introduced in the first paragraph of section 4.1.1, i.e. a regular network of active stripes. As in the last section, time averaging was started after $t_s = 20000$ time steps. It was carefully checked that a stationary state has been reached at this point. (cf. Fig. 4.12). As time averaging interval 50000 time steps were chosen. In Fig. 4.11 particle configurations for moderate and high densities are displayed. For particle density $\rho_p^0 = 0.04$ one observes small L-shaped clusters centering at intersections. For higher densities it appears that clusters are becoming larger and merge with each other to form large mesh-shaped clusters (cf. fig 4.11(b)). However, in this case clusters are hardly distinguishable and not well separated, which results in sensitive dependence on the coarse graining scale (cf. Fig. 4.14). In Fig. 4.13 the cluster size distributions averaged over time and 100 individual runs are plotted. Examining the cluster size distributions in Fig. 4.13, one observes similar to random clustering an exponential decay for densities which are biologically relevant (see also the configuration in figure 4.11(a)). However, here they are overlapped by one or more bulges which appear to be in the size scale of the L-shaped clusters at intersections. A more detailed discussion of these profiles will be explicated in Sec. 4.1.3.

For large densities ($\gtrsim 0.1$) the decay of the cluster size distribution becomes algebraic, indicating that clusters on all size-scales exist. These large clusters correspond to the ones generated by merged small clusters as displayed in Fig. 4.11(b).

Inhomogeneous networks

The filament growth dynamics described in the second paragraph of section 4.1.1 generate a network where single filaments have random length and direction. In order to keep dynamics simple but retaining the crucial features of disordered networks, we neglect branching and the dynamics of ARP2/3 in the first

[6]The stationary state of irreversible clustering is a single cluster if phase space is not separated.

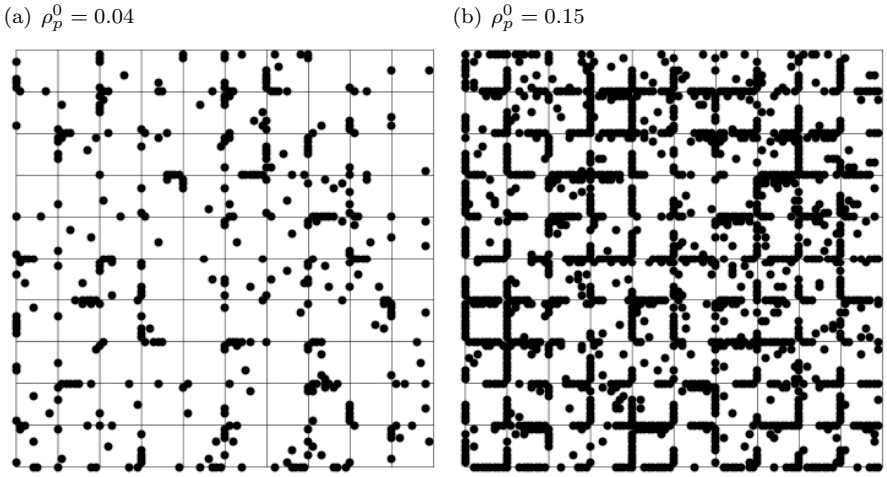

Figure 4.11: Particle configurations in a regular square network with system length $N = 100$ sites. The black discs represent particle neighborhoods with radius 1.1 sites so that discs of particles with one vacancy or less in between overlap. One observes the formation of small L-shaped clusters at intersection points for moderate densities (a). For large densities clusters merge, forming cluster meshes on all size-scales (b).

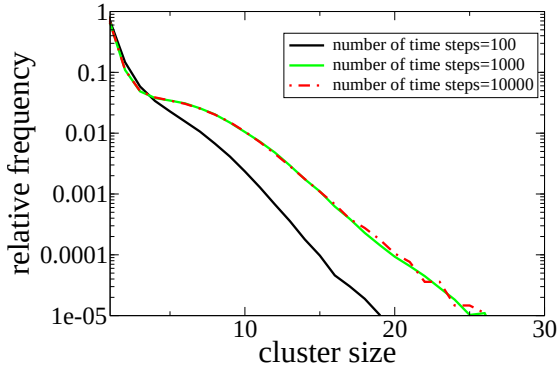

Figure 4.12: Cluster size distributions in a regular network for different runtimes (given in time steps). For a given runtime, the last 100 steps were chosen to perform the measurement, taking 100 samples. The CD does not change after 1000 time steps, indicating that the system is in a stationary state.

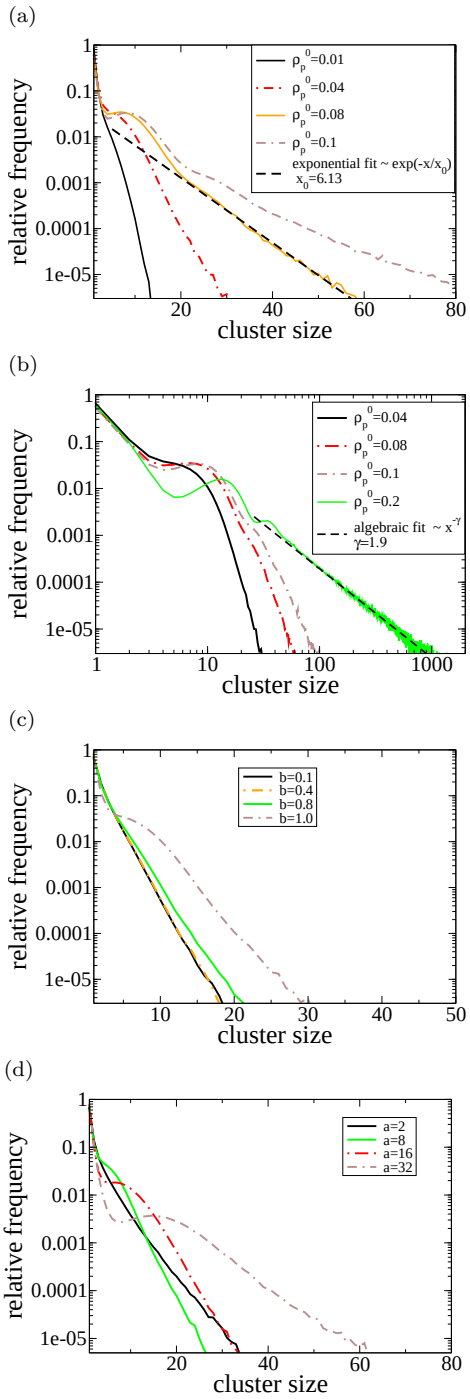

Figure 4.13: Cluster size distributions in a lattice gas model with exclusion interaction and a regular square network of active stripes in dependence on particle density ρ_p^0, logarithmic plot (a), double logarithmic plot (b), blocking rate b (c) and mesh size a (d). One observes that cluster size distributions decay exponentially for moderate densities resulting in a finite size-scale of clusters, while at small scales, bulges emerge. For very large densities decay is algebraic indicating the emergence of clusters on all size-scales (see also Fig. 4.11). Default parameters: see Table 4.2.

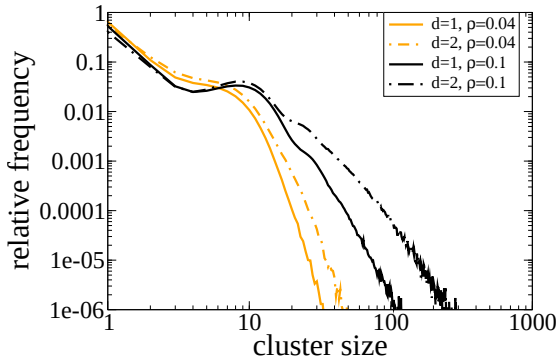

Figure 4.14: Cluster size distributions in the regular network obtained by using different definitions of the coarse graining scales. d is the distance allowed between two particles to connect a cluster. One observes that while variations are small for moderate density, there is a significant influence on the scale for larger densities, indicating that clusters are not well separated.

paragraph to obtain a network of uncorrelated filament orientations. The other processes are required to obtain a disordered stationary network configuration.

Networks without branching filaments Particle configurations and cluster size distributions were obtained, applying steric interactions, which are shown in figures 4.15-4.20. The time evolution of the cluster size distribution (Fig. 4.16) shows that a stationary state is reached after 10000 time steps. Starting time averaging after 20000 time steps (averaging interval=50000 time steps) therefore captures the steady state dynamics. For low ω_d however, the transient time might be significantly prolonged. Therefore a much larger time of $400000\Delta t$ was used for starting cluster evaluation. After that time no time dependence of CDs is observed even for the smallest considered value of ω_d.

The configuration for default density $\rho_p^0 = 0.04$ (Fig. 4.15) shows that well separated compact clusters exhibiting different sizes emerge (see also scaling in Fig. 4.20). In a large parameter regime including the biological relevant default parameters (Table 4.4), the asymptotic decay of the CD is algebraic in contrast to the predominant exponential behavior on a regular network. For intermediate cluster sizes m, the CD follows a power law, $P(m) \sim m^{-\gamma}$, while at larger scales, there appears to be a crossover to a decreased exponent $\tilde{\gamma} < \gamma$. The exponent γ depends explicitly on system parameters. It decreases with particle density ρ_p^0 and increases with the network density, which is determined by ρ_{act}. The dependence on ρ_p^0 indicates a behavior in form of $(\gamma - 2) \propto 1/\rho_p^0$, which is consistent with analytical results in Sec. 4.1.3 (see Fig. 4.19). The dependence on other parameters like ω_a and ω_d appears to be weak for default parameters. However, for lower ρ_p^0, or a larger value of ω_d/ω_a, the dependence on these parameters becomes more relevant, while varying other parameters does not lead to qualitative changes except in extreme regimes. In Fig. 4.21 cluster size distributions of a regular and inhomogeneous network are compared[7]. One observes that clustering is significantly enhanced in the inhomogeneous network.

[7]Differences in effective rates due to the different spatial character of the system (discrete and continuous) are not significant since dependence on these parameters is weak.

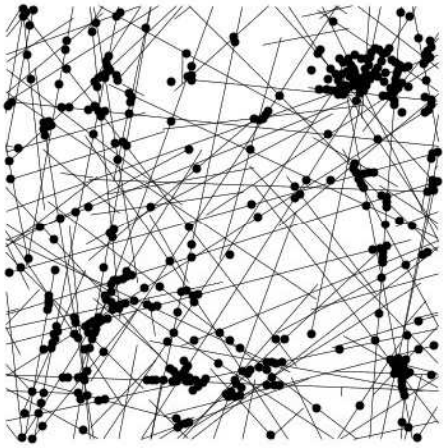

Figure 4.15: Particle configurations (black discs = neighborhoods with $\lambda = 2\,r_p$) for default parameters and $\rho_p^0 = 0.04$ and system size $L = 200\,r_p$. One observes big and small clusters. This general picture is predominant for a large parameter regime and moderate densities.

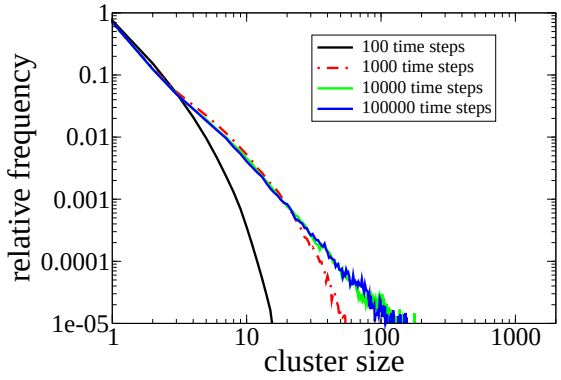

Figure 4.16: Cluster size distributions for different runtimes. For 10000 time steps a stationary state is reached.

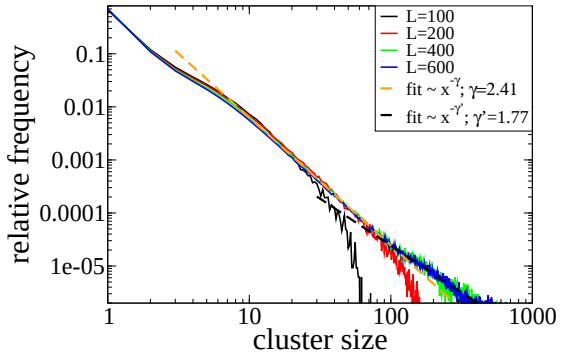

Figure 4.17: Cluster size distributions in dependence on the systems size. The CD decays algebraically in a large regime indicating the absence of a intrinsic size-scale. Fitting the curves, one observes a crossover from exponent γ to a smaller exponent γ' for large cluster sizes. This crossover is well approximated by the formula $\gamma' = \gamma/2 + 0.5$ (4.16) . Default parameters: see Table 4.4

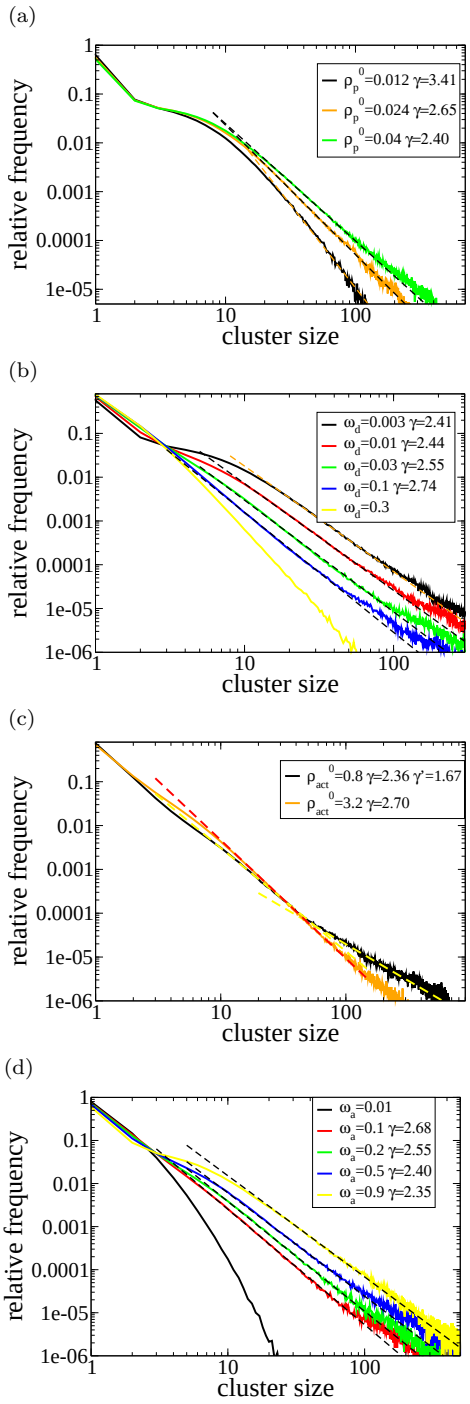

Figure 4.18: Cluster size distributions in a diffusive system with an inhomogeneous active transport network, single parameters varied: (a) particle density ρ_p^0 for small detachment rate $\omega_d = 0.002$, (b) detachment rate ω_d, (c) actin density ($\sim$ network density) ρ_{act}^0, (d) attachment rate ω_a. The exponent of the algebraic fit mainly depends only on ρ_p^0 and ρ_{act}^0. The dependence on ω_d and ω_a is weak, as long as $\omega_d \ll \omega_a$. Default parameters: see Table 4.4

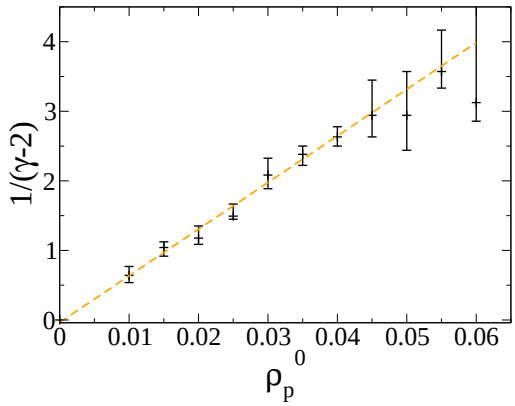

Figure 4.19: Dependence of the exponent γ of the cluster size distribution $p(m)$ on the particle density ρ_p^0 for $\omega_d = 0.002$. One observes a linear dependence on the value $1/(\gamma - 2)$ up to $\rho \approx 0.045$ which yields $\delta := \gamma - 2 \propto 1/\rho_p^0$ as predicted by the phenomenological analysis in Sec. 4.1.3. The exponents were obtained by power law regressions in the range $m \in [30, 80]$ for $\rho < 0.04$ and $m \in [30, 100]$ for $\rho > 0.04$. Error bars (obtained by varying fitting range) increase for γ approaching the singular value 2.

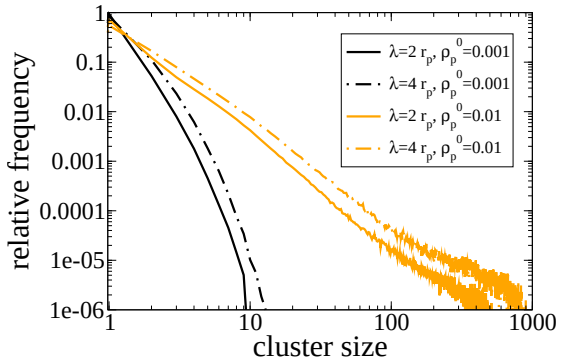

Figure 4.20: Cluster size distributions in the inhomogeneous network for different coarse graining scales. λ is the radius of the neighborhood as defined in section 4.1.2. As well in the regime where large clusters emerge and in the non-clustering regime, the dependence on the coarse graining scale is weak indicating well separated clusters.

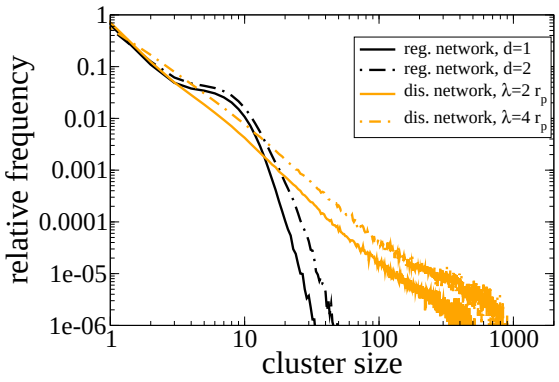

Figure 4.21: Comparison of regular and inhomogeneous network displaying cluster size distributions for particle density $\rho_p^0 = 0.04$. While the CD decays exponentially in the regular network, its slope is algebraic in the inhomogeneous one, demonstrating significant enhancement of clustering by the inhomogeneous network structure (see Fig. 4.14 for definition of d).

Due to the finite number of particles there is a cut-off at the upper end (e.g. in Fig. 4.20). Fig. 4.17 shows that for increasing system size L the cut off regime tends to larger values, indicating that this indeed is a finite size effect and asymptotically algebraic behavior prevails in the thermodynamic limit. Though the exponent γ of the algebraic decay varies for different particle densities, the algebraic form is a robust feature. This indicates that in the thermodynamic limit clusters on all size-scales exist. In contrast to regular networks, scale free clustering occurs even for moderate densities ($\rho_p^0 \approx 0.01$) exhibiting a pattern of well separated clusters.

Networks with branching filaments In real actin networks, branching of filaments takes place quite frequently, resulting in a dendritic network structure. If one is interested in the dynamics of vesicle transport on submembranal actin networks, one has to consider this process as well. CDs in a system with finite branching rate ω_b were checked (here: branching probability $\omega_b \Delta t = 0.0035$) including the dependence of growth dynamics on the ARP2/3-density ρ_{ARP} (cf. section 4.1.1, second paragraph). In this system, filament orientations are highly correlated.

In Fig. 4.22 cluster size distributions for different particle densities ρ_p^0 are displayed. Like in the more basic case of uncorrelated filaments, $\omega_b = 0$, one observes an algebraic decay as well. This indicates that the scale free behavior of the clusters is a robust feature of inhomogeneous transport networks with active hard-core particles.

4.1.3 Phenomenological description of Cluster Formation

In order to understand the distribution of cluster sizes m in the inhomogeneous network theoretically, we analyze the capacity of intersections. Thereby we consider dynamics of cluster initialization and stability of the cluster distribution in the stationary state.

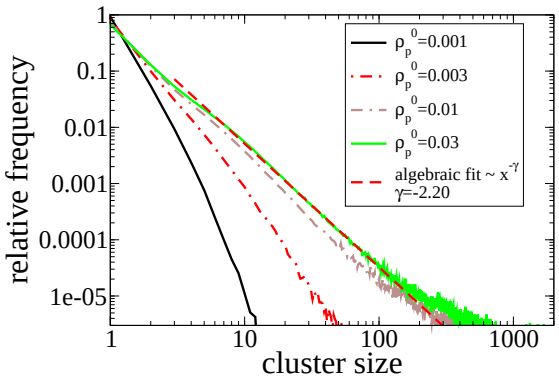

Figure 4.22: Cluster size distribution for branch rate $\omega_b > 0$. Like in the system with non-correlated filaments, the CD exhibits algebraic decay for large clusters.

Single queues

A necessary condition for cluster formation is that two particles moving along a filament encounter each other at an intersection. Then the two particles may block each other due to steric interactions and form a *cluster seed*. Therafter other particles can attach to the filament moving towards the initial two-particle cluster and form a queue.

Studying the queuing mechanism, we regard a single filament with an intersection occupied by a cluster seed. The filament can be considered as a one-dimensional discrete system coupled to a reservoir of particles with density $\rho_p - \rho_b$, i.e. the density of unbound particles (where ρ_p denotes the *local* particle density and ρ_b the density of bound particles).

The effective attachment rate of a particle is the attachment rate ω_a times the fraction of area that allows binding and the probability that there is space on the filament, i.e. [8]

$$\tilde{\omega}_a \approx \omega_a 2 d_b d_s \rho_s \left(1 - \frac{\rho_p}{\rho_s} n_s\right) \quad . \tag{4.2}$$

Here n_s is the number of binding sites that are not accessible if a particle occupies a filament and ρ_s is the total density of filament subunits of length d_s in the system, i.e. $\rho_s = \rho^0_{act} - \rho_{act}$. We assume $\rho_p \ll \rho_s$ which is the case for default parameters. In a regular discrete network $n_s = 1$, while in the inhomogeneous one $n_s = 5$ for $d_s = 0.36\,lu, r_p = 0.5\,lu$, since the distance of two particles must be at least $2r_p$ [9].

Complete detachment occurs with an effective rate $\tilde{\omega}_d$, comprising detachment and diffusing away, such that there is free space for particles behind to move on the filament. Therefore a detached particle may not reattach immediately and a subsequent diffusive step must be lateral to the filament. Diffusing can also be inhibited by a high density of free particles. We therefore write $\tilde{\omega}_d = \omega_d(1 - \omega_a \Delta t)(1 - \rho_p \pi r_p^2 \Delta t) C_1(D)$ where the phenomenological factor $C_1 < 1$ reflects the inhibition of a diffusing step by other attached particles

[8] The binding area of a filament in continuous space is approximated by a rectangular shape since $d_s < d_b$. In the regular network $d_s = 1, d_b = 1/2$ and binding area = active tracks.

[9] For default parameters, $\tilde{\omega}_a$ takes the value $\tilde{\omega}_a \approx 2/3\omega_a$

on the filament. This factor represents the angle sector that allows free diffusion and is assumed only to depend increasingly on the diffusion constant $D = l_D^2/2\Delta t$. In this single queue view, particle dynamics correspond to the TASEP-LK. Queues correspond to high density domains in the TASEP-LK, i.e. one-dimensional clusters, hence the queue ends correspond to shocks. On long filaments the density of attached particles quickly approaches the stationary density $\rho_b = \rho_p\tilde{\omega}_a/(\tilde{\omega}_a + \omega_d)$ (cf. [53]). Therefore the inflow on a single filament queue can be approximated by $J_{in}^1 = p\,\rho_b/\rho_s(1-\rho_b/\rho_s) \approx p\,\tilde{\omega}_a/(\omega_d+\tilde{\omega}_a)\,\rho_p/\rho_s$, neglecting $(\rho_b/\rho_s)^2$. Outflow by detaching particles is $J_{out}^1 = \tilde{\omega}_d l$ where l is the number of particles in the queue. The condition that a stationary queue of length l establishes is $J_{in}^1 = J_{out}^1$ if a two particle cluster has established. Hence we have $\rho_p p/(\rho_s(\tilde{\omega}_a + \omega_d)) = \tilde{\omega}_d l$ and

$$\rho_p(l) \approx \frac{\tilde{\omega}_d l \rho_s}{p}\left(1 + \frac{\omega_d}{\tilde{\omega}_a}\right) \tag{4.3}$$

If the queue does not cross other filaments, a finite queue of length l_0 establishes, while the shock, i.e. the end of the queue performs fluctuations around the mean value l_0 [27, 49].

Cluster branching

If a queue spans over intersections connecting the filament with other ones, it acts as an obstacle for particles moving along crossing filaments. This obstacle serves as a nucleation seed for other queues on respective filaments in a same manner like at the initial two-particle cluster seed. It leads to a branching of the queue and can initialize a cascade of queues that constitute a large connected cluster (see Fig. 4.23). At first glance, we neglect freely diffusing particles in the neighborhood of the queues which can also be part of clusters by the definition in Sec. 4.1.2, since their effect on cluster in- and out flow can be treated by the local particle density ρ_p and effective detachment rate $\tilde{\omega}_d$. Then the full cluster is constituted by the connected set of these individual queues, $m = \sum_i l_i$ where the index i runs over all filaments covered by the cluster.

The intersections not only initialize new cluster branches, but also serve as defects for particle hopping, since at these points the hopping rate p is effectively lowered. In principle this corresponds to the TASEP-LK with defects which was treated in the last chapter. If inflow is larger than the transport capacity of a defect, a macroscopic high density domain emerges corresponding to a queue. Though at defects, small diluted regions after defect sites occur, we can assume the queues to be connected on a coarse graining scale $\lambda > r_p$ and by particles diffusing in the neighborhood of the filament[10]. If $\rho_p < \rho_p(l = a) =: \rho^*(a)$ such that queues do not span other intersections, clusters consist of two queues each on one of the filaments at the cluster seed's intersection. Since the length of the queues in the TASEP-LK is always finite, there is a finite mean value $\bar{l}$. Therefore the total cluster size can be estimated by

$$m \approx n_F \bar{l}\,, \tag{4.4}$$

where n_F is the number of filaments it covers.

[10]Though the considerations of the last chapter were for large systems where attachment and detachment rates scale like $\omega_{a,d} \sim 1/L$, qualitative results do not change while relative fluctuations of shockpositions and boundary layers increase for small systems.

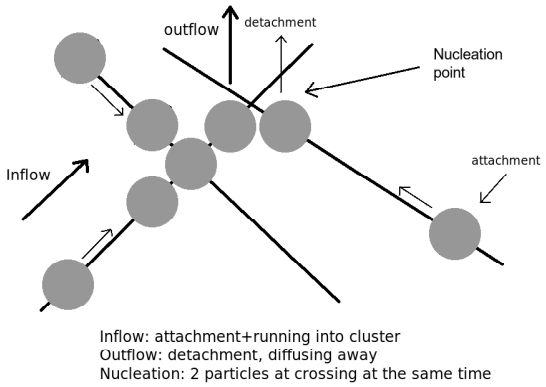

Figure 4.23: Illustration of the mechanism that leads to the formation of clusters in a inhomogeneous network. If the density of intersections is high, existing clusters serve as additional obstacles for particles on other filaments, enhancing cluster formation.

The considerations of this and the last paragraph apply in an analogue way to a regular network if d_b is replaced by $1/2\,lu$ and $d_s = 1\,lu$. In the following paragraphs, however, the explicit statistics of the inhomogeneous network are considered.

Graph approximation

The above considerations show that the statistics of filament crossings appear to be crucial for cluster dynamics if the network is disordered. In the following a coarse graining (length-)scale ξ is introduced and the distribution of filaments on this scale is studied. This provides the basis for a coarse graining procedure where the filament network is approximated by a *graph* and dynamics of particles are approximated by effective transition rates between nodes of a topological network (see Sec. 2.4).

In the following considerations on inhomogeneous networks we assume that filament lengths L_F are large compared to the scale ξ of the target area we consider.

The probability that a given filament with arbitrary orientation, position and length $L_F \gg \xi$ intersects an area of diameter ξ is

$$p \approx \frac{\xi}{L}\,\frac{L_F}{L} \tag{4.5}$$

The average length of filaments is $\langle L_F \rangle = \rho_s L^2 d_s / N_F$ and N_F is the number of filaments. Averaging over filament lengths, one obtains

$$p = \frac{\xi \rho_s d_s}{N_F} \quad . \tag{4.6}$$

Obviously the probability that n_F filaments cross an area of diameter ξ is equivalent to the probability distribution of a Poisson process with individual hit probability p.

$$P(n_F) = \frac{\sigma^{n_F}}{n_F!} e^{-\sigma} \tag{4.7}$$

with expectation value and standard deviation $\sigma = p\,N_F = \xi\rho_s d_s$. Therefore the average number of intersecting filaments grows linearly with the diameter of the considered area and one can define a linear filament density $\rho_F = \langle n_F\rangle/\xi = \rho_s d_s$. The average subunit density is related to the actin density by $\rho_s = \rho^0_{act} - \rho_{act} \approx \rho^0_{act}$ (for $\omega_s/\omega_g \ll \rho^0_{act}$, cf. Sec. 4.1.1). In uncorrelated filament networks, the average distance between nodes, i.e. the mesh size $a = \pi/(2\rho_s d_s)$ [43], therefore the dependence on the actin density is $a \sim 1/(\rho_s d_s) \sim 1/\rho_{act} d_s$. Since the structure of the clusters is one-dimensional, its linear scale is $\xi \propto m r_p$. Therefore the number of filaments a cluster covers is $n_F \sim m\,r_p/a$. On the other hand we have $n_F \approx m/\bar{l}$. Hence the average queue length scales like the mesh size, i.e. $\bar{l} \sim a/r_p$.

In order to describe particle dynamics on a coarse grained level, we approximate the filament network by a topological network (graph) consisting of nodes connected by links, representing the filaments. On the topological network the particle dynamics is described by hopping from node to node with given rates, assuming that particle transport is dominated by active transport. In this approximation we assume that most particles are bound to filaments, i.e. $\rho_b = \rho_p\,1/(1+\omega_d/\tilde{\omega}_a) \approx \rho_p$, which is justified for $\omega_d \ll 2\omega_a\rho_s d_s d_b$ [11]. This marks the limit of the *graph approximation*. Diffusive phases are assumed to be short but can lead to a change of the filament, i.e. changing travel direction.

Similar to the considerations above, the network structure is coarse grained by virtually subdividing filaments into segments of length ξ representing the nodes of the network. Segments from different filaments that overlap at intersections are treated as one node. A filament hosting segments of two nodes i and j directed from i to j corresponds to a link from i to j. It mediates a net particle drift from i to j. The full network can then be represented by the adjacency matrix $\mathbf{A}$ whose components A_{ij} denote the number of links between i and j. Note that in this view two nodes can be connected by more than one link. Corresponding to Sec. 2.4, we denote the number of out-going links from a node i by $K_i^{out} = \sum_j A_{ij}$ and the number of in-going links by $K_i^{in} = \sum_j A_{ji}$. Each filament crossing a node without ending inside provides exactly one link in and one out of the node. If filament lengths are large compared to the length scale ξ as assumed above, we can neglect filament ends inside a node. Therefore the number of incoming links is approximately equal to the number of out-going links. Their number is given by the number of filaments, i.e. $K_i^{in} \approx K_i^{out} = n_F$.

In Sec. 2.4 it has been shown that for noninteracting particles performing a random walk on a topological network with $K_i^{in} = K_i^{out} =: K_i$ for all nodes i, the density of particles in the stationary state is proportional to the number of links

$$\rho_i = K_i/\mathcal{N} \tag{4.8}$$

We can transfer the results from topological networks to the graph approximation and state that the density of free particles ρ_p^f inside a node, i.e. particles that are not associated to a cluster, is proportional to the number of links which is given by the number of filaments n_F crossing it. The spatial distribution of (local) free particle density therefore is proportional to the distribution of filaments $\rho_p^f = \bar{\rho}_p^f n_F/\langle n_F\rangle$, where n_F is the number of filaments in a node and $\bar{\rho}_p^f$ is the *average* free particle density. This distribution however is scale dependent and the selection of the appropriate scale must be justified by other means.

[11] For default parameters $\omega_d/2\omega_a\rho_s d_s d_s \approx 0.12$

In the graph approximation the system is modelled by a hopping of particles from one node to another. This introduces a time scale τ which is the time, a particle needs to travel from one node to another. If we use the average distance between intersections (mesh size of the network) a as length scale ξ, the effective hopping time can be related to the node distance by $a = pd_s\tau_b$, where τ_b denotes the time a particle is bound to a filament, i.e. $\tau_b = \tau/(1 + \omega_d/\tilde{\omega}_d)$ (see first paragraph). Hence $\tau = a/pd_s(1 + \omega_d/\tilde{\omega}_d)$. For this coarse graining scale each node contains one intersection on average and in the corresponding graph they are connected on average by two filaments with adjacent nodes, i.e. $\langle n_F \rangle = 2$ and the distribution of links (and therefore local densities) is governed by a Poisson distribution with mean value $\sigma = 2$. If queues branch, queue cascades constitute a *large* cluster that covers a number of filaments n_F proportional to its size m. The structure of the graph must hence be adjusted, since large clusters are able to span over more than one node as defined above. In order to treat clusters as single objects we consider all nodes a cluster covers as a single one. Then the network consists of cluster nodes made up by large clusters and free nodes where there are no stable clusters. We denote the number of cluster nodes by N_{cl} and the cluster density $\rho_{cl} = N_{cl}/(L/a)^2$.

The free particle density ρ_i corresponds to the probability that after long times a particle inserted anywhere will be at node i. Since the size m_i of a cluster i is proportional to the number of filaments n_F it covers, it is proportional to its connectivity K_i and therefore ρ_i. The probability of new inserted particles to end up in cluster i is hence proportional to its size, i.e. the growth rate of a cluster is proportional to its size m.

Cluster size distributions

Due to particle conservation, the total inflow of particles in clusters J_{in} must balance outflow J_{out} in the stationary state. In the following we denote the total portion of particles associated to clusters by $\tilde{N}$ and free particles by $N_f = N - \tilde{N}$. The outflow can be expressed by $J_{out} = \omega_d^{eff}\tilde{N}$, where the effective rate ω_d^{eff} comprises the rate of particle detachment from a filament and attachment to another one in order to be moved to a free node. We can write $\omega_d^{eff} = \tilde{\omega}_d C$. The phenomenological factor $C < 1$ denotes the inference by interactions with particles on *other* queues of the cluster and other filaments directed into the cluster that allow reattachment to the cluster. The factor C is a mean value and depends explicitly on the structure of the clusters, but not explicitly on system parameters[12]. It becomes small if very large clusters are present that can confine particles within their structure (see paragraph on large clusters below). The flow of particles into clusters is given by $J_{in} \approx N_f\, \rho_{cl}\, \langle n_F \rangle/\tau$. The stationarity condition is $J_{out} = J_{in}$ and with $\tilde{N} = N_{cl}\langle m \rangle$, $\langle n_F \rangle = \langle m \rangle/\bar{l}$ we obtain

$$\tilde{\omega}_d C N_{cl}\langle m \rangle \approx N_f \frac{N_{cl}}{(L/a)^2}\,\frac{\langle m \rangle}{\bar{l}}/\tau \tag{4.9}$$

$$\Leftrightarrow \quad \bar{\rho}_p^f = N_f/L^2 = \frac{\tilde{\omega}_d C\ \bar{l}}{apd_s}\left(1 + \frac{\omega_d}{\tilde{\omega}_a}\right)$$

[12] At least in the network approximation where particles are assumed to be attached to filaments most of the time. For higher values of ω_d/ω_a an explicit dependence on ω_a is assumed.

The corresponding number of particles associated to a cluster is $\tilde{N} = N - N_f$. For large ω_d^{eff} this quantity could reach zero so that there are no clusters left. This suggests a condensation transition between a free phase and a phase exhibiting clusters. However, we have to be careful since on the one hand the graph approximation does not work for large ω_d and on the other hand aster-like configurations of nodes, where filament ends are arranged to point only into a node, have been neglected. These configurations can become relevant in this situation and allow clusters even for lower particle densities. We therefore assume that for $L \to \infty$ large clusters can be present even for small densities. However since we have seen in the last sections that most particles are in clusters for default parameters, we can assume that $\omega_d^{eff} \ll a^2\rho_p^0/(\tau\bar{l})$ which suggests $C_1 C \ll 1$.

In order to determine the probability distribution of cluster sizes $P(m)$, we virtually expand the system. Assume the system to be in the stationary state. Increasing the system size by a small area ΔA, while always remaining in the stationary state, $\Delta N = \rho_p^0 \Delta A$ new particles are inserted. The portion of cluster-associated particles hence is

$$\Delta\tilde{N} = \Delta N - \Delta N_f \approx \Delta A(\rho_p^0 - \tilde{\omega}_d C\tau\bar{l}/a^2) \tag{4.10}$$

which is the number of particles that are effectively added to the clusters. However, not only particles are added to the clusters but also $\Delta N_{cl} = \rho_{cl}\Delta A/a^2$ new clusters emerge within the new area ΔA. Thus for each new cluster that emerges $\Delta\tilde{N}/\Delta N_{cl} = \langle m\rangle = a^2(\rho_p^0 - \tilde{\omega}_d C\tau\bar{l})/\rho_{cl}$ new particles are distributed among the clusters, while the probability that a particle is associated to a given cluster is proportional to its size m as argued above. This process corresponds to a generalized Yule process, where between two cluster initialization events, $\langle m\rangle$ objects are distributed among the clusters (see e.g. the review [70]). The stationary state of the Yule process exhibits a distribution which approaches for large m asymptotically a power law distribution $P(m) \sim m^{-\gamma}$ with an exponent $\gamma = 2 + \frac{m_0}{\langle m\rangle}$ where m_0 is the initialization value of the clusters. Hence the exponent yields

$$\begin{aligned} \gamma &= 2 + \delta \\ \delta &\approx \frac{m_0\rho_{cl}}{\rho_p^0 - \tilde{\omega}_d C\tau\bar{l}/a^2} \end{aligned} \tag{4.11}$$

If distances between clusters are large, the cluster density ρ_{cl}, i.e the number of clusters per area unit $\xi^2 \approx a^2$, corresponds to the probability P_{cl} that a cluster seed nucleates at an intersection. In order to maintain a stable queue with at least one particle on a filament (i.e. a initial two-particle cluster), according to (4.3), the density of particles on the filament must be $\rho_p^1 = \bar{\rho}_p^f n_F/\langle n_F\rangle > \tilde{\omega}_d\rho_s/p(1 + \omega_d/\tilde{\omega}_a)$. Inserting (4.9) and $\rho_s = \pi/(2\,a d_s)$, this yields a condition on the local filament density

$$\frac{n_F}{\langle n_F\rangle} = \frac{2}{\pi\bar{l}C} \sim \frac{1}{aC} \sim \rho_{act} r_p d_s \tag{4.12}$$

where the fact that $\bar{l}$ scales like a/r_p was used. Since we are only interested in the dependence on system parameters, we neglect any prefactors that do not depend explicitly on them, like C. Since the filaments are Poisson-distributed

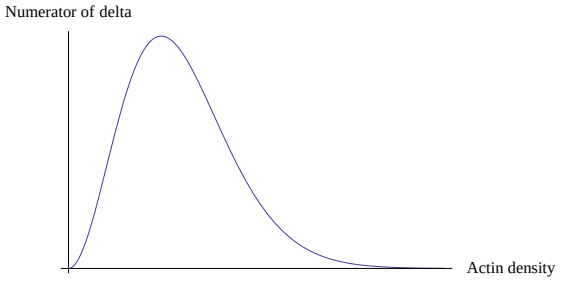

Figure 4.24: Sketch of the probability that a cluster nucleates at a intersection in dependence on the network density.

with mean value 2, this probability can be given by the cumulative Poisson distribution with mean $\sigma = 2$:

$$P_{cl} = P\left(n_F > \frac{2}{C\bar{l}}\right) \sim \frac{\Gamma(2/C\bar{l}+1,2)}{\Gamma(2/C\bar{l})} \tag{4.13}$$

and the dependence of $\gamma = 2 + \delta$ is given by

$$\delta \sim \frac{P_{cl}(\rho_{act})\rho_{act}^2}{\rho_p^0\left(1 - \frac{\pi\tilde{\omega}_d\bar{l}C\rho_s}{2p\rho_p^0}\right)} \tag{4.14}$$

by inserting $a = 2/(\pi\rho_s d_s) \sim 1/\rho_{act}$, considering r_p and d_s to be fixed by biological reasons. As argued above, we assume $C_1 C \ll 1$, hence the term $\pi\tilde{\omega}_d\bar{l}C\rho_s/2p\rho_p^0$ can be neglected for small ω_d, and δ can be further simplified to

$$\delta \sim P_{cl}(\rho_{act})\rho_{act}^2/\rho_p^0 \ . \tag{4.15}$$

The dependence of $\delta = 2 - \gamma$ on ρ_p^0 appears to be a quite good approximation as can be seen in Fig. 4.19. In Fig. 4.18, one observes only a weak monotonic dependence on ω_d as long as ω_d is small, though this dependence becomes stronger for large ω_d, as expected. The numerator depends only on ρ_{act} and has the form as displayed in Fig. 4.24 (the scale is not defined, since the prefactor is not given). However, only for small values of ρ_{act} the cluster density can be approximated by the probability P_{cl}. For large network densities if clusters on average cover many intersections the effective cluster number is smaller since clusters nucleating on different intersections can merge. Therefore we assume that the relevant values are restricted to the lower branch which attains a monotonic growth. This appears to be valid as is shown in Fig. 4.18.

Summarizing, we can say that for small ω_d relative to $\tilde{\omega}_a$ and mean particle density ρ_p^0, δ is proportional to $1/\rho_p^0$ and depends increasingly on ρ_{act} (though not linear in general). In these limits there is no dependence on other system parameters (see Fig. 4.18). For larger ω_d, the influence of ω_d, ω_a, l_D and p becomes relevant.

So far, free particles that also contribute to clusters have been neglected. This approximation yields good results for low particle densities and if clusters are not too large. Then the cluster structure is mainly one-dimensional, made up by queues and only some free particles in their neighborhood whose influence

on detachment can be comprised in ω_d^{eff}. Large clusters however rather have a two- than a one-dimensional structure since detaching particles can completely fill the cavities engulfed by queues. Then the full cluster size is $\tilde{m} \sim m^2$. Cluster attachment and detachment are still determined by the one-dimensional fraction m constituted by the queues, thus arguments from above remain valid. Hence the distribution of 2D-clusters yields

$$P(\tilde{m}) = P(m)|_{m=\tilde{m}^{1/2}} \frac{\partial m}{\partial \tilde{m}} \sim \tilde{m}^{-\gamma'} \tag{4.16}$$

with $\gamma' = \gamma/2 + 1/2$. The distribution is also described by a power law but with a decreased exponent γ'. This result is consistent with simulation results in Fig. 4.17. Note that high filament densities suppress this effect since no big cavities between filaments are present (cf. 4.18(c)). High ω_d / low ω_a enhance the effect, since due to a large number of unbound particles their contribution to clusters is enhanced.

In principle the above considerations are also valid for a regular network, while in those systems the particle density is homogeneously distributed and $a = const.$. If the density for cluster initialization ($l = 1$) is exceeded, clusters can emerge anywhere in the system. As long as the density is lower than the critical density $\rho^*(a)$ to form queues of length a, only small L-shaped clusters consisting of two queues emerge (see configuration in Fig. 4.11(a)). These are characterized by a centered distribution P_{m_0} exhibiting fluctuations around a mean value m_0, while no cluster branching occurs. Since the scale of queue lengths is in the same order of magnitude as random clustering (cf. Fig. 4.6), the exponential background of free particles must be added, hence $P(m) \approx P_{m_0}(m) + 1/m_r \exp(-m/m_r)$ where m_r is the scale of random clusters[13]. This behavior corresponds to Fig. 4.13 where a bulge over an exponential is exhibited. However, if $\rho^*(a)$ is exceeded, cluster cascades can develop. Due to the homogeneous density, clusters can branch at any intersection and due to the high cluster density, they merge forming a mesh shaped structure. This leads to a percolative behavior yielding a scale free distribution, while clusters are not well separated (cf. Fig. 4.11(b)). Hence cluster distributions do not follow the same scheme as disordered networks.

While scale free clustering in regular networks only emerges for $\rho_p^0 > \rho^*$, in inhomogeneous networks this can occur also for small densities $\rho_p^0 \ll \rho^*$ since the distribution of the particle density and filament distances determining the critical density is wide. Only few regions where the critical density is exceeded are needed for scale free clustering. This corresponds to a Griffith phase where only locally critical values are exceeded exhibiting an ordered structure, in contrast to the case when the full system is clustered[14]. Therefore clusters are well separated and do not depend significantly on the coarse graining scale.

The formation of clusters in active transport networks yields the possibility of an aggregation mechanism even without attractive interactions. The function of vesicle transport on actin therefore might not be restricted to merely enhanced diffusive dynamics. However, due to translational symmetry, single particle

[13]Note that due to the attractive interaction of filaments a lateral aggregation of particles is induce that locally increases the density compared to the average density ρ_p^0. This leads to an increased size scale of random clusters

[14]Note that this does not imply percolation. There are dilute regions behind intersections emerging that can tear clusters apart, if there are only few free particles.

dynamics are completely undirected if periodic boundary conditions are applied. This symmetry is broken if boundary conditions are applied that confine particle and filament dynamics to a finite area/volume. In the following section, effects on single particles due to boundary conditions will be studied.

4.2 Transport on inhomogeneous networks in confined geometries

Since the growth dynamics introduced in the last section is undirected and periodic boundary conditions obey translational invariance, the network structure is unbiased, besides finite size effects that can lead to a weak bias. In most works due to these undirected growth dynamics, the transport on actin networks therefore is considered to merely enhance diffusive properties of vesicle transport, while no bias on large scales is present. Directed long range transport is thought to be associated with microtubules (see e.g. [44]). In mammalian cells, directed transport from the cell center (ER or Golgi) towards the cell membrane in order to liberate proteins to the exterior (secretory pathway) or transport of internalized proteins to the center (endocytic pathway) is mediated by the radially structured microtubule network. In smaller cells (e.g. budding yeast) usually the microtubules do not play an essential role in transport [45] that provide a radial structure, such that it is assumed that targets are reached purely by diffusive dynamics.

However, in real systems there are boundaries imposed by cell organelles and the cell membrane that confine filament and particles dynamics and break translational symmetry. In this section we will see that the inclusion of boundary conditions in our model can lead to a bias in particle dynamics despite non-directed filament growth dynamics. The application of boundary conditions can significantly decrease the times, particles need to find a given destination (*Mean First Passage Time*). E.g. it is shown that the time, particles need to travel from the boundary of a sphere to a target sphere in the center is significantly reduced due to this bias. We will see that an analogy to electrostatics can elucidate this unexpected bias induced by boundary conditions and suggests that the mechanism is also valid in three dimensions.

4.2.1 Results

Reflecting boundary conditions

In contrast to the model of disordered networks in the last section, here the movement of particles is restricted on a sphere/disc of radius R around the origin. In addition filaments are not allowed to be initialized or to grow out of this sphere. The microscopic growth dynamics remain unbiased, i.e. newly initialized filaments have random direction. In addition to particles that move to plus-ends of filaments (*plus-particles*), which represent transport by myosin V, we introduce particles that move in minus-direction of filaments (*minus-particles*). These are motivated by vesicles that are transported by myosin VI [2].

Boundary conditions break the translational symmetry that is present in periodic systems. Here boundary conditions are introduced that restrict filament

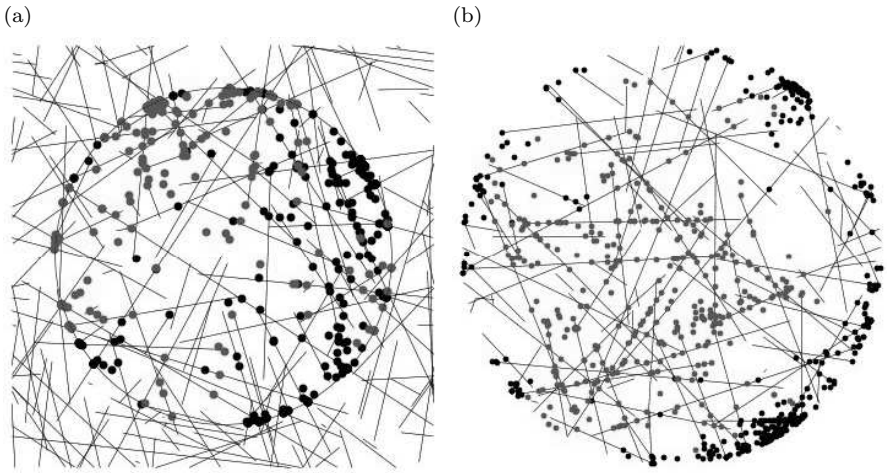

Figure 4.25: Configuration of plus- (black) and minus-particles (gray).(a) dynamics of filaments not restricted (periodic boundary conditions). Both kinds of particles appear to be concentrated at boundaries. (b) Dynamics of both particles and filaments restricted to the sphere. One observes separation of particles with plus-particles at the boundaries and minus-particles in the interior. The inhomogeneity of the distribution of the minus-particles however is not that significant as for plus-particles, which can also be seen in Fig. 4.26.

dynamics and the region, that particles can explore to a finite area/volume. In order to distinguish effects on filament and particle dynamics, also artificial mixed boundary conditions are applied, i.e. periodic boundary conditions for filaments and confining ones for particles. Here we are interested in single particle dynamics. Hence in simulations, interactions between particles are neglected.

In Fig. 4.25 configurations for periodic and confining boundary conditions for filaments are shown. Particle movement is restricted to a sphere in both cases. Fig. 4.26 shows the ensemble averaged particle density distributions. If both particle and filament dynamics are restricted to the confined area, one observes a segregation of the two particle species. While plus-particles are concentrated at the boundaries, minus-particles are diluted at the boundary and get a tendency towards the center of the sphere. If filament dynamics are not restricted there is no radial separation of particles. However both particle species appear to be driven to the boundaries at opposite sides of the system. This effect can be easily understood. In a finite size configuration of filaments a weak random bias remains that drives plus-particles in a given direction towards the boundary at one side of the system, while minus-particles are driven to the other side. Both particle species aggregate at the boundaries at opposite sides of the system. While this indeed leads to separation of both species in space, the radial distribution appears to be the same for both species since left and right are not distinguished in radial distributions.

The observation that restricting filament dynamics leads to a radial separation of particle species indicates that breaking the translational symmetry induces a self-organized global bias in filament orientations. In order to understand this effect, the *radial bias* of the network is studied, which is defined as

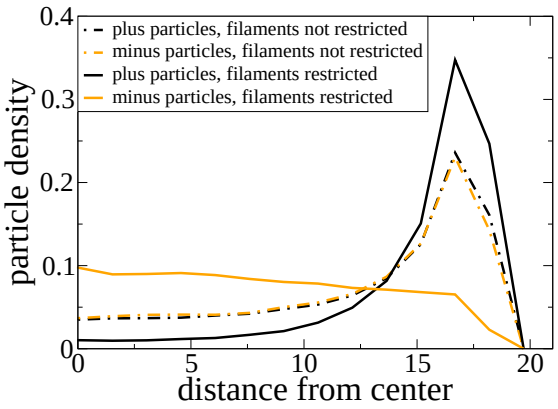

Figure 4.26: Density distribution of non-interacting particles in dependence on the distance from the center. Even for a non biased network the density distribution is inhomogeneous: both particle species are concentrated at the boundary. For restricted filament dynamics, one observes a separation between plus- and minus-particles.

the correlation of filament subunit orientations $\mathbf{d}$ with the radial unit vector[15]:

$$\eta(r) := \langle \mathbf{d} \cdot \mathbf{e}_r \rangle = \frac{1}{n(r)} \sum_{|x| \in [r, r+dr]} \mathbf{d} \cdot \mathbf{e}_r \ , \tag{4.17}$$

where $n(r)$ is the number of filament subunits in an distance interval $[r, r + dr]$ from the center. This quantity is positive if filaments are predominantly orientated radially, i.e. pointing away from the center, and negative if orientated towards the center.

In order to quantify the impact of the boundaries on the network structure, results are compared with a system where filament dynamics are not restricted, while vesicles may not leave the sphere. In Fig. 4.27 the radial bias for a network with confining boundaries and without is plotted. In the case without boundaries, periodic boundary conditions are applied. One observes that there is no radial bias for periodic boundary conditions. However if filament dynamics are restricted, filaments are indeed biased and plus-ends are predominantly oriented away from the center, resulting in a positive radial bias. The bias becomes stronger approaching the boundary.

The emergence of a biased network structure can be understood by an analogy to electrostatics. In order to illustrate this analogy, we define the *filament field*

$$\mathbf{F}(x) = \left\langle \lim_{V \to 0} \frac{1}{V} \sum_{V} \mathbf{d} \right\rangle \tag{4.18}$$

where V is any volume (or area in 2D) including the point x and $\langle \cdots \rangle$ denotes the ensemble average. Thus $\mathbf{F}(x)$ results from a superposition of filament orientations at the point x. Due to radial symmetry of the boundaries, the ensembe average must exhibit radial symmetry, and we can also write

$$\mathbf{F}(\mathbf{x}) = \mathbf{F}(r)\mathbf{e}_r \tag{4.19}$$

[15]By convention the minus-end of a filament subunit is used as refererence position.

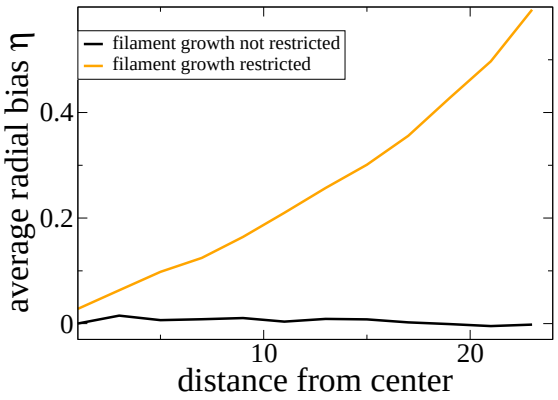

Figure 4.27: Ensemble averages for the network radial bias η in dependence on distance of filament segments from the center. If growth dynamics is not restricted to boundary conditions, there is no overall radial bias, while if growth dynamics is restricted, filament plus-ends appear to be directed towards the boundary of the system.

Note that the radial component of $\mathbf{F}$ and the network bias η are related by

$$F(\mathbf{r}) = \eta(\mathbf{r})\, \rho_s^r(r) \tag{4.20}$$

where $\rho_s^r(r) = 2\pi r \rho_s(r)$ is the radial density of filament segments at distance r from the center.

At any point inside the allowed volume, filaments can be initialized with random direction while any direction has equal probability. First we assume that filaments are restricted to be nucleated only at a single point, i.e. the origin, but can grow anywhere. Since the orientation of filaments always points away from the nucleation point, the filament field must have a radial structure $\mathbf{F}(\mathbf{x}) = F(r)\mathbf{e}_r$. Since the field obeys a linear superposition principle, the strength of the field at a point $\mathbf{x}$ can be expressed by the probability that a created filament crosses $\mathbf{x}$, $P(\mathbf{x})$, times the average fraction of time τ_{fil} a segment is present there, i.e. $F(\mathbf{x}) = P(\mathbf{x})\tau_{fil}$. In order to quantify these values, we approximate the dwell times by the inverse rates for leaving a state.

After nucleation, a filament remains capped, i.e. it does not dissociate for a time $1/\omega_{uc}$. When it uncaps, the filament dissociates and it requires an average time $1/\omega_n\rho_{act}$ until a new filament is nucleated. The overall time of a nucleation cycle therefore is $t_{tot} = 1/\omega_{uc} + 1/\omega_n\rho_{act}$. The average velocity of the growing end is $d_n\,\omega_g\rho_{act}$ while the velocity of the shrinking end is $d_n\,\omega_s$. After nucleation the distance r is reached by the growing end after a time $r/(d_n\omega_g)$. After uncapping an average time of $r/(d_n\omega_s)$ passes until the shrinking end passes the distance r removing nodes there. The overall fraction of time that filament nodes are present at distance r during one nucleation cycle therefore is

$$\tau_{fil} = \frac{t_{fil}}{t_{tot}} = \frac{\left(\frac{1}{\omega_{uc}} - \frac{r}{d_n\omega_g\rho_{act}}\right) + \frac{r}{d_n\omega_s}}{\frac{1}{\omega_n\rho_{act}}} = \frac{\omega_n\rho_{act}}{\omega_{uc}} + \frac{r\omega_n\rho_{act}}{d_n}\left(\frac{1}{\omega_s} - \frac{1}{\omega_g\rho_{act}}\right) \tag{4.21}$$

Since the surface of a sphere is $\sim r^2$ in 3D and r in 2D, the probability that a nucleated filament crosses a given point scales as $P(x) \sim 1/r^{D-1}$ (D=dimension).

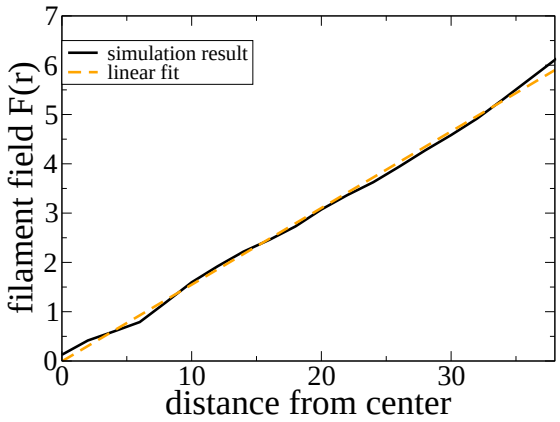

Figure 4.28: Filament field $F(r)$ for default parameters. One observes approximately a linear behavior as predicted by the analytical treatment.

In the stationary state there is no net change of the number of filament subunits, hence $\omega_s = \omega_g \rho_{act} + \omega_n \rho_a ct \approx \omega_g \rho_{act}$ (for $\omega_g \gg \omega_n$). In this case the dependence of τ_{fil} on the distance r vanishes and the filament field takes the form

$$F(r) = \frac{C}{r^{D-1}}, \;\; C \text{ independent of r} \Rightarrow \mathbf{F}(\mathbf{x}) = \frac{(\mathbf{x} - \mathbf{x}')}{|\mathbf{x} - \mathbf{x}'|^D} \tag{4.22}$$

which is equivalent to the electrostatic field of a point charge. In particular the first Maxwell equation div$\mathbf{F} = 4\pi C \delta(\mathbf{x})$ and the corresponding Gaussian law are valid. In the transient state, $\omega_g \rho_{act} \neq \omega_s$ and the divergence varies from the delta-function structure.

If there is a larger volume where filaments can nucleate, due to superposition the filament field behaves like a electrostatic field of a homogeneously charged volume: $\mathbf{F}(x) = \int_V C \frac{(\mathbf{x}-\mathbf{x}')}{|\mathbf{x}-\mathbf{x}'|^D} d^D x$. For periodic boundary conditions, no net field remains because of the translational symmetry, and therefore the overall bias $\eta \equiv 0$. However if the filament-generating volume is restricted to a sphere, the filament field has the same form like the electrostatic field inside a homogeneously charged sphere, thus

$$\mathbf{F}(\mathbf{x}) \sim r \mathbf{e}_r \tag{4.23}$$

This linear behavior of $\mathbf{F}$ is reproduced by simulations of filament ensembles as can be seen in Fig. 4.28. Since $F(r) \sim \eta$ and $\rho_s^r > 0$, the bias η must be positive and filament orientations tend to point away from the center, although locally filament dynamics are undirected. The emerging radial bias of the network explains why for confined filament dynamics plus-particles are driven towards the boundaries and minus-particles are driven to the center of the sphere.

Creation and annihilation of particles at boundary and center

In secretory cells proteins produced in the interior of a cell (usually near the nucleus), have to be transported to the cell membrane in order to be liberated to the exterior (secretory pathway). On the other hand macromolecules that have

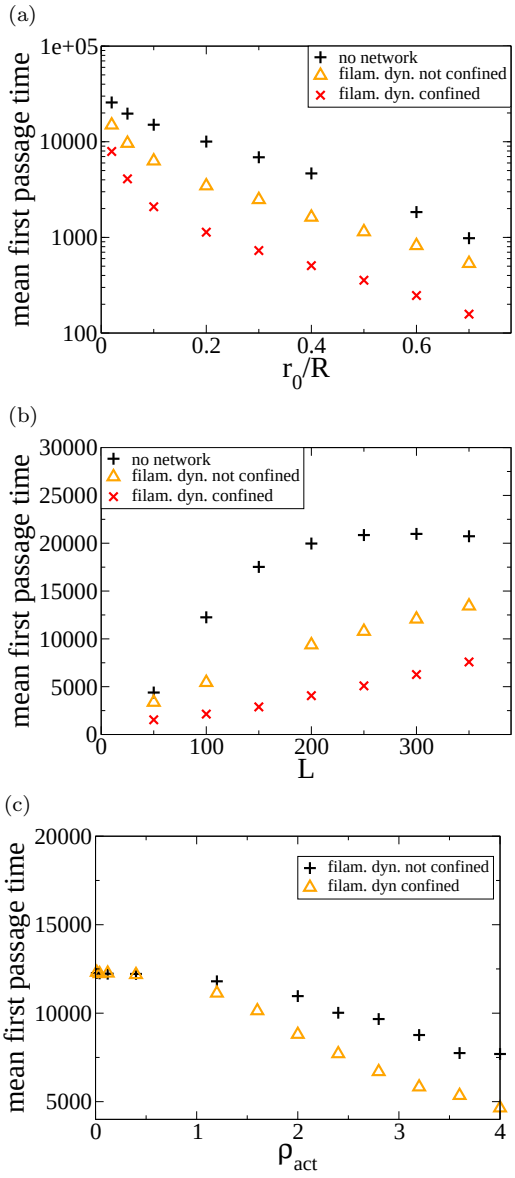

Figure 4.29: Mean first passage times of minus-particles in a purely diffusive syste. Comparison of confined network dynamics and non-confined. The plots in the subfigures show the dependence on different parameters: (a) radius of target area r_0 (fixed R), (b) system radius R (fixed ratio r_0/R), (c) actin density (determining mesh density) ρ_{act}. In all figures one observes a significant reduction of MFPT if an active network is present, and a further reduction of about the same amount due to confined filament dynamics.

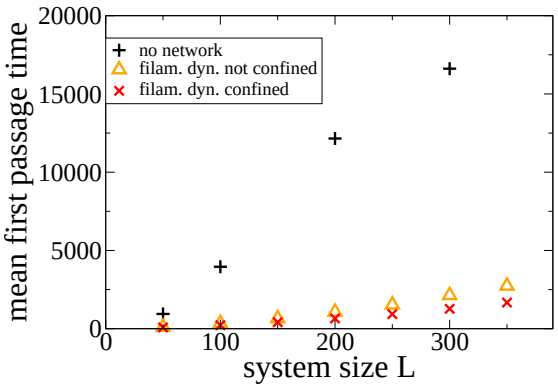

Figure 4.30: Mean first passage times in dependence on the system size for plus-particles. The MFPT are significantly reduced by the presence of a network. A further decrease of the MFPT by restricted network dynamics is observable, but the difference to a non-directed network is not as significant as for minus-particles.

been internalized by endocytosis might be needed by organelles near the center of the cell, e.g. the nucleus or ER (endocytic pathway). In both cases effective mechanisms to transport vesicles to their target destinations are necessary. A quantity of interest therefore is the time a vesicle needs to reach its target.

In our model the secretory pathway can be simulated by creating particles near the center of the sphere, while particles are annihilated if they reach the boundary. The endocytic pathway corresponds to particles that are created at the boundary and disappear if they reach their target area, which is implemented as a sphere of radius r_0. The time particles need on their pathways corresponds to the *first passage time (FPT)*. Here, the distribution of first passage times in particle ensembles and their average value, the *mean first passage time (MFPT)*, is investigated.

In Fig. 4.29 and 4.30, the mean first passage times in dependence on system size L, radius of target area r_0 and actin density ρ_{act} are plotted. Here pure diffusive particles dynamics are compared with a network generated by unrestricted filament dynamics and restricted filament dynamics. One observes that the presence of a active transport network significantly reduces the times, particles need to reach their target. In case of the unbiased network, this is consistent with results in [65], where a mixture of random walk and ballistic fast directed movement was considered[16]. However, the restriction of filament dynamics to a finite volume leads to a further reduction of mean first passage time on the endocytic pathway. The MFPT for minus-particles is significantly reduced. The factor of this reduction is rather independent of the fraction of the target area.

The acceleration of pathways may be a beneficial property for some cell types. For particles on the secretory pathway, however, this effect does not seem to be strong.

[16]There however the network dynamics were not explicitly modelled.

4.3 Discussion

The transport on filament networks rather than single tracks appears to introduce new phenomena both on single particle dynamics and collective properties. Besides the enhancement of diffusive properties compared to a purely diffusive system [53], the presence of filament crossings allow steric interactions of particles on different filaments. This interaction causes jamming of particles at intersections, leading to the formation of particle queues.

In a regular network, these queues remain usually small exhibiting a finite size scale. Only if densities are high enough, such that clusters on different intersections merge, there are large non-separated clusters. In a disordered network where filaments are randomly distributed (in orientation, position, and length), distances between intersections are spatially varying. In this kind of network, large, well-separated clusters can emerge. The corresponding distribution of cluster sizes appears to be algebraic in a wide range of the parameter space indicating that clusters on all size scales exist.

In contrast to regular networks, inhomogeneous networks exhibit regions of small mesh sizes where queues can span over several intersections, hence even small queues can span over several intersections. The interaction with other particles on these intersections can induce new queues on latter ones leading to branched large clusters. Since each branch contributes to cluster inflow, the growth rate of a cluster is proportional to its size. Dynamics of this kind can be described by a Yule process (see e.g. [70]) which yields a power law distribution $P(m) \sim m^{-\gamma}$ with an exponent depending on the microscopic parameters (see also preferential attachment in scale-free networks [4]). A thorough investigation shows that for small detachment rate and moderate network densities, the exponent merely depends on the average particle density and the average network density, while dependence on other parameters is weak. Since only distinct parts of the system exhibit a network density high enough to induce cluster branching, the resulting large clusters are usually well separated, in contrast to the regular network.

Periodic boundary conditions that exhibit translational symmetry demand a globally unbiased network structure, as long as filament dynamics are not explicitly biased and the system is large. This constraint does not hold if boundary conditions are applied that break this symmetry. In our case, motivated by actin dynamics, filaments nucleate and grow in an arbitrary direction, i.e. locally non-biased. However, if these dynamics are restricted to a finite volume (as it is the case in cells), the breaking of translational symmetry introduces a bias in the network structure. Applying the same growth dynamics as before, but confining filament dynamics to a sphere/disc of finite volume/area, now plus-ends of filaments are predominantly orientated towards the boundaries, while minus-ends tend to point towards the center. This can be understood by an analogy to electrostatics: since the Greens function of an electrostatic field does not prefer any direction, the field of a homogeneous charge density distribution vanishes if there are no boundaries. However a homogeneously charged sphere of finite volume exhibits a radial electric field inside the sphere, increasing linearly with distance from the center. This linear behavior can also be observed in the filament network if the spatial dependence of the orientation, weighted by the filament density, is considered.

Chapter 5

Conclusions and outlook

In this thesis inhomogeneous driven stochastic systems used for modeling active transport processes of sterically interacting particles were investigated. The focus is on intracellular processes. The considered inhomogeneities are of two types:

(a) Spatially varying velocity of driven particles. These are for example varying codons on mRNA that need different times to be processed by ribosomes, or macromolecules that cover intracellular filaments and inhibit movement of motor proteins. These are observed in neurons affected by Alzheimer's disease (degenerated tau proteins) and it was shown that vital transport properties in axons are significantly reduced in this case [93].

(b) Networks with a disordered irregular structure. One example is the cortical actin network at the inner side of the cell membrane of most eukaryotic organisms which exhibits a irregular structure [84].

Both species of disorder significantly change large scale dynamics of particle transport compared to homogeneous systems. Common to both kinds of systems is the emergence of queuing transitions due to inhibited movement of particles at defects (corresponding to intersections in network systems). These queues result in alternating high- and low density regions, observed in one-dimensional single filament models, and particle clusters that can arise in two-dimensional transport network models. The results of the thesis are separated in two parts, each of them covering one species of disorder.

In chapter 3 disordered driven lattice gases are considered, which are used to model active transport on single tracks. The disorder is implemented by randomly including slow sites with a lower hopping rate q (defects) within predominant fast sites of hopping rate $p > q$. The motif of investigations is the observation that the transport capacity, i.e. the maximum current that can be achieved by tuning external parameters, is predominantly determined by the longest *bottleneck*, i.e. consecutive stretch of defects [96, 61]. This motivates the *Single Bottleneck Approximation (SBA)* stating that the transport capacity of a driven lattice gas is approximately the same as in a system containing only one, i.e. the longest bottleneck. Therefore results for systems with single bottlenecks of arbitrary length appear to be relevant to understand randomly disordered systems. In this work in particular the paradigmatic *totally asymmetric simple exclusion process (TASEP)* was considered. In fact a good approximation for the TASEP with a single bottleneck is obtained in chapter

3 by the *interacting subsystems approximation (ISA)* that treats the system as separate but connected homogeneous subsystems. Using the exact solution of the homogeneous TASEP and connecting subsystems, a good approximation for the transport capacity of a single bottleneck system can be obtained. The ISA not only yields the transport capacity, but also the phase diagram can be obtained and the influence of defects near the boundaries (*edge effect*) can be explained. It was shown that the edge effect can be treated by introducing *effective boundary rates*.

Applying extreme value statistics, the SBA can be used to relate the ensemble averaged transport capacity of the disordered, many-defect TASEP to a single bottleneck system. Hence the single bottleneck results can be used to determine the transport capacity of disordered systems. Deviations from SBA are mainly due to other defects in the vicinity of the longest one. The limits of the validity of SBA for generic driven lattice gases were checked and formulated, giving a criterion that other defects can be treated perturbatively for small defect densities (3.41). For the TASEP, a perturbative expansion of the transport capacity in terms of the defect density ϕ yields accurate results already in first order. In general, SBA can also be applied for other driven lattice gases fullfilling a set of conditions (see discussion in 3.4) and conserving particles in the bulk, which was exemplified for the disordered *NOSC model*. In intracellular transport, however, attachment and detachment of motor proteins from a bulk reservoir occurs which violates particle conservation in the bulk. An inclusion of these processes in driven lattice gases breaks the spatial invariance of the current. In Sec. 3.3 a generalization of the SBA considering the transport capacity as a local quantity is introduced (*local independent bottleneck approximation (LIBA)*). A local minimal principle for the current is derived, which is shown to reproduce current profiles and phase diagrams of driven lattice gases with defects. Applied on disorder ensembles, the approach yields the approximate parameter region for phase separation.

The results provide insight into generic features of disordered driven systems. While in their presented form they are restricted to binary quenched (time-independent) disorder, it might be a favorable future task to extend the methods to time-dependent defect distributions or allowing more than one defect value. From a biological point of view, the results of this part might help to understand and quantify the transport slowing effect by tau proteins in neuronal axons of Alzheimer patients. Since neuronal activity depends vitally on transport of e.g. neuro transmitters to synapses, it is assumed that this effect marks a main contribution to the pathology of Alzheimer's disease. On the other hand inhibiting molecules can also be intentionally inserted in the system, as was done in in-vitro experiments [22, 88], with the perspective to develop drugs that can control or reduce intracellular transport by blocking molecular motors (e.g. in cancer cells). Since on mRNA, clusters of slow codons have been observed [77], results on the transport capacity of single bottlenecks can help to quantify protein production rates in presence of high ribosome concentration. This might improve understanding of gene regulation and synthetic protein production.

The second part of this thesis considers model networks, in particular disordered ones that correspond to the second type of inhomogeneities, (b). The models introduced in this part combine free diffusion of particles with stages of active transport on the network. The disordered model is motivated by transport of vesicles on actin filaments by myosin V/VI. The model network is

generated by growth dynamics motivated by real actin filament growth which do not exhibit a preferred direction. For a periodic system this dynamics constitutes a globally undirected network for large systems. However, not only diffusive properties of particles are enhanced, but the presence of intersections introduces the possibility of steric interactions between particles on different filaments, inhibiting each others movement. Hence intersections act as defects in a similar manner like in single track systems, inducing queues. It was shown that in a regular square network, these clusters usually remain restricted to small size scales, constituted by two individual queues. In contrast disordered networks exhibit large well separated clusters, whose sizes are distributed by a power law distribution while its exponent significantly depends on parameters of particle dynamics and mesh size. It was shown that this scale free behavior can occur in general if queues span over intersections inducing a cascade of cluster branching. A mechanism that enhances growth of larger clusters (preferential attachment) can explain the observed power law distribution. In contrast a comparison with a clustering mechanism driven by attractive interaction of particles reveals that there only clusters on intrinsic size scales exist.

The significant differences in qualitative aspects of the cluster distributions, emerging from the different microscopic mechanisms, suggest that an experimental analysis of cluster size distributions can help to identify microscopic mechanisms. A possible application lies in the investigation of receptor clusters on cell membranes (e.g. clusters of receptors that promote the internalization of deleterious toxins in budding yeast [11]). While the optical resolution of single receptors is a difficult task in-vivo, protein clusters can be observed ([90]) and conclusions on microscopic particle dynamics can be made, which might improve the understanding of toxin uptake of cells.

If confining boundaries are included that restrict particle dynamics and filament growth on a finite volume/area, the translational symmetry is broken. Investigating the mean orientation of filaments numerically, one observes a self-organization of the network, in a way that plus-ends of filaments are predominantly orientated away from the center, if growth dynamics are confined to a sphere/disc. The bias of the network structure can be understood by an argument well known from electrostatics. This effect significantly reduces the time which minus-particles (those moving to the minus-end of filaments) need to travel from the boundary to the center compared to periodic boundary conditions.

These observations suggest that the contribution of the actin network in the dynamics of intracellular transport might not be restricted to enhancement of diffusion but can also significantly drive directed radial transport between the cell center, especially on the endocytic pathway. The results might be extendable to study the effect of generic boundary conditions that are given e.g. by the presence of cell organelles.

Appendix A

Negative vs. positive edge effect

We now want to determine a condition that the current decreases for a bottleneck approaching a boundary (*negative edge effect*). Again, due to the particle-hole symmetry (2.8) it is sufficient to consider a bottleneck near the left boundary. We have to distinguish if the current for a defect at a small distance $L_1 = \mathcal{O}(1)$ from the boundary is larger or less than the current for a defect far from the boundary, $L_1 \to \infty$. Though the dependence of the current on the position of the first defect is not always monotonic, for an approximation it is sufficient to compare the current $J(L_1)$ for *one* position of the defect near the boundary with the current $J(\infty)$ for a defect far from the boundary, since the mixed edge effect (see Sec. 3.1.3) is quite weak and only in a small parameter region. For simplicity we take $L_1 = 2$.

Using (2.9) and (3.8) yields

$$J(\alpha, \beta_1, 2) = \frac{\alpha\beta_1^2 + \alpha^2\beta_1}{\beta_1^2 + \alpha\beta_1 + \alpha^2 + \alpha\beta_1^2 + \alpha^2\beta_1}\,, \tag{A.1}$$

where β_1 is the virtual exit rate of subsystem 1. The edge effect is negative if

$$J(\alpha, \beta_1, 2) < J(\alpha, \beta_1, \infty)\,. \tag{A.2}$$

In the L-phase[1] we have $J(\alpha, \beta_1, \infty) = \alpha(1-\alpha)$ and (A.2) is fullfilled if

$$\beta_1 < 1 - \alpha\,. \tag{A.3}$$

Though we cannot determine β_1 exactly, we can state that β_1 is less than in a homogeneous system with $q = 1$, $\beta_1 < \beta_1^{\mathrm{hom}}$. However, in a pure system there is a flat density profile without correlations, and we have exactly $\beta_1^{\mathrm{hom}} = 1 - \alpha$, so (A.3) is always fulfilled. Therefore in the L-phase and, due to particle-hole-symmetry, in the H-phase, the edge effect is always negative.

In systems with many randomly distributed bottlenecks it is very unlikely that longest one is near the boundary. Thus the transition to the B-phase, where the current is independent of the boundary rates, will occur for lower rates of $\alpha(\beta)$, where the negative edge effect is predominant.

[1]The term "phase" here refers to the phases of the system with a defect far from the boundaries where it is well defined.

Appendix B

Phase diagram of the disordered TASEP-LK

Usually it is quite difficult to determine the transition line between S- and DPS-phase. One special case where it is possible to solve that problem exactly is in the strong continuum limit in the disordered TASEP-LK for $\Omega_a = \Omega_d =: \Omega$. In addition the number of defects is infinite, while the defect density is scaled to zero as $\phi = \mathcal{O}(1/\ln L)$. The average length of the longest bottleneck in a system of size L scales as $\ln L/\ln\phi$ [61], so in the strong continuum limit there has to be an infinitely large bottleneck with a local transport capacity $J_M^* = q/4$. Moreover, we can say that this is the case for any small interval of length ε if ε is scaling slower than $\sqrt{1/L}$, corresponding to $L\sqrt{1/L} = \sqrt{L}$ sites. The global capacity field therefore simply is the constant function $\mathcal{C}(x) = q/4$. Since the defect density vanishes, the CDR is the same as in the homogeneous system as was shown in the last sections numerically and analytically. The local boundary current and density profiles will therefore be the same as in the homogeneous system. Now the problem to solve is equivalent to finding the transition from S- to LMH-phase[1] in the homogeneous TASEP-LK if the homogeneous maximum current $J^* = 1/4$ is exchanged by $q/4$ [27]. In these works, the transition line was determined to be $\tilde{\beta}^*(\tilde{\alpha}) = \rho_L(J^*) - \Omega - \tilde{\alpha}$. Inserting $J^* = q/4$, we obtain for the transition line

$$\tilde{\beta}^*(\tilde{\alpha}) = 1/2 - \sqrt{\frac{1-q}{4}} - \Omega - \tilde{\alpha} \tag{B.1}$$

which is just a shift of the phase transition line to the right by the term $\sqrt{(1-q)/4}$. The properties of the phases of course are different to the ones in the homogeneous system as was argued before (especially the absence of long ranged boundary layers). The phase diagram is displayed in Fig. 3.34. We have to point out that in this limit, the transition is of second order, since ξ is continuous.

Nonetheless the vanishing of ϕ in the continuum limit is not quite physical, so we try to obtain at least qualitative results for the S-DPS transition line for finite ϕ. In Sec. 3.3.2 and 3.3.3 we have seen that a small but finite defect density $\phi > 0$ leads to a flattening of the local density profiles due to a broadening of the

[1] For definition of the LMH-phase, see [27].

density peaks, so that their slopes $\frac{\partial \rho_{L,H}}{\partial x}$, which are positive for $\Omega_a = \Omega_d,\ \alpha < 1/2,\ \beta < 1/2$, are decreasing for higher current J.

Assume the system is on the transition line between S and DPS, i.e. a triple point x_t with $J_\alpha(x_t) = J_\beta(x_t) = q/4$ exists. A shift of both ρ_α and ρ_β by an infinitesimal amount dx also shifts the triple point though it persists. In parameter space, this corresponds to a movement along the transition line, while the boundary values are changed by

$$d\alpha = \left.\frac{\partial \rho_\alpha}{\partial x}\right|_{x=0} dx \quad \text{and} \quad d\beta = -\left.\frac{\partial \rho_\beta}{\partial x}\right|_{x=1} dx \tag{B.2}$$

$$\Rightarrow \quad \frac{d\beta}{d\alpha} = -\frac{\left.\frac{\partial \rho_\beta}{\partial x}\right|_{x=1}}{\left.\frac{\partial \rho_\alpha}{\partial x}\right|_{x=0}} \tag{B.3}$$

using the relations $\alpha = \rho_\alpha(0)$ and $\beta = 1 - \rho_\beta(1)$. Since the boundary current $J_{\alpha,\beta}$ is monotonously increasing with α and β for $\alpha, \beta < 1/2$, the flattening of the density profiles leads to:

$$\text{For } \beta > \alpha: \left.\frac{\partial \rho_\beta}{\partial x}\right|_{x=1} < \left.\frac{\partial \rho_\alpha}{\partial x}\right|_{x=0} \quad \Rightarrow \quad \frac{d\beta}{d\alpha} > -1 \tag{B.4}$$

$$\text{For } \alpha > \beta: \left.\frac{\partial \rho_\beta}{\partial x}\right|_{x=1} > \left.\frac{\partial \rho_\alpha}{\partial x}\right|_{x=0} \quad \Rightarrow \quad \frac{d\beta}{d\alpha} < -1 \tag{B.5}$$

along the transition line. This corresponds to a concave distortion of the DPS-phase as displayed in Fig. 3.34.

Own publications

P. Greulich, A. Garai, K. Nishinari, A. Schadschneider, D. Chowdhury. Intra-cellular transport by single-headed kinesin KIF1A: effects of single-motor mechano-chemistry and steric interactions. *Phys. Rev. E*, 75:041905, 2007

K. Nishinari, Y. Kanayama, Y. Okada, P. Greulich, A. Schadschneider and D. Chowdhury. Stochastic modelling and experiments on intra-cellular transport of single-headed molecular motors. *Traffic and Granular Flow '05*, 2007

P. Greulich and A. Schadschneider. Phase diagram and edge effects in the ASEP with bottlenecks. *Physica A*, 387:1972, 2008

P. Greulich and A. Schadschneider. Single-bottleneck approximation for driven lattice gases with disorder and open boundary conditions. *J. Stat. Mech.: Theor. and Exp.*, P04009, 2008

D. Chowdhury, A. Basu, A. Garai, P. Greulich, K. Nishinari, A. Schadschneider and T. Tripathi. Intra-cellular traffic: bio-molecular motors on filamentary tracks. Eur. Phys. J. E, 64:593, 2008

D. Chowdhury, A. Garai, P. Greulich, K. Nishinari, A. Schadschneider, T. Tripathi, J.-S. Wang. From CA to Gene Expression: Machines and Mechanisms. *Lecture Notes In Computer Science: ACRI 2008*, 2008

P. Greulich and A. Schadschneider. Statistical Properties of Disordered Driven Lattice Gases with Open Boundaries. *Traffic and Granular Flow '07*, 2009

P. Greulich and A. Schadschneider. Disordered driven lattice gases with boundary reservoirs and Langmuir kinetics. *Phys. Rev. E*, 79:031107, 2009

P. Greulich and L. Santen. Active transport and cluster formation on 2D networks. Submitted to *Eur. Phys. J. E*, 2009

Bibliography

[1] R. Albert and A.-L. Barabási. Statistical mechanics of complex networks. *Rev. Mod. Phys.*, 74:47, 2002.

[2] B. Alberts, A. Johnson, J. Lewis, M. Raff, K. Roberts, and P. Walter. *Molecular Biology of the Cell.* Garland, 2002.

[3] T. Antal, P. L. Krapivsky, S. Redner, M. Mailman, and B. Chakraborty. Dynamics of an idealized model of microtubule growth and catastrophe. *Phys. Rev. E*, 76:041907, 2007.

[4] A.-L. Barabási and R. Albert. Emergence of scaling in random networks. *Science*, 286:509, 1999.

[5] M. Barma. Driven diffusive systems with disorder. *Physica A*, 372:22, 2006.

[6] O. Biham, A. A. Middleton, and D. Levine. Self-organization and a dynamical transition in traffic-flow models. *Phys. Rev. A*, 46:R6124, 1992.

[7] C. Boldrighini, G. Cosimi, S. Frigio, and M. G. Nunes. Computer simulation of shock waves in the completely asymmetric simple exclusion process. *J. Stat. Phys.*, 55:611, 1989.

[8] M. L. Cano, D. A. Lauffenburger, and S. H. Zigmond. Kinetic analysis of F-actin depolymerization in polymorphonuclear leukocyte lysates indicates that chemoattractant stimulation increases actin filament number without alterin the filament length distribution. *J. Cell Biol.*, 115:677, 1991.

[9] A. E. Carlsson, A. D. Shah, D. Elking, T. S. Karpova, and J. A. Cooper. Quantitative analysis of actin patch movement in yeast. *Biophysical Journal*, 82:2333, 2002.

[10] A. E. Carlsson, M. A. Wear, and J. A. Cooper. End versus side branching by ARP2/3 complex. *Biophysical Journal*, 86:1074, 2004.

[11] S. Y. Carroll, P. C. Stirling, H. E. Stimpson, E. Gießelmann, M. J. Schmitt, and D. G. Drubin. A yeast killer toxin screen provides insights into A/B toxin entry, trafficking, and killing mechanisms. *Developmental Cell*, 17:552, 2009.

[12] T. Chou and G. Lakatos. Clustered bottlenecks in mRNA translation and protein synthesis. *Phys. Rev. Lett.*, 93:198101, 2004.

[13] D. Chowdhury, A. Basu, A. Garai, P. Greulich, K. Nishinari, A. Schadschneider, and T. Tripathi. Intra-cellular traffic: bio-molecular motors on filamentary tracks. *Eur. Phys. J. B*, 64:593, 2008.

[14] D. Chowdhury, L. Santen, and A. Schadschneider. Statistical physics of vehicular traffic and some related systems. *Phys. Rep.*, 329:199, 2000.

[15] D. Chowdhury and A. Schadschneider. Self-organization of traffic jams in cities: Effects of stochastic dynamics and signal periods. *Phys. Rev. E*, 59:R1311, 1999.

[16] J. A. Cooper. The role of actin polymerization in motility. *Annu. Rev. Physiol.*, 53:585, 1991.

[17] B. Derrida, M. R. Evans, V. Hakim, and V. Pasquier. Exact solution of a 1D asymmetric exclusion model using a matrix formulation. *J. Phys A Math. Gen.*, 26:1493, 1993.

[18] N. Destainville. Cluster phases of membrane proteins. *Phys. Rev. E*, 77:011905, 2008.

[19] J. Dong, B. Schmittmann, and R. K. P. Zia. Towards a model for protein production rates. *J. Stat. Phys.*, 128:21, 2006.

[20] J. L. Doob. *Stochastic Processes*. Wiley-Interscience, 1990.

[21] K. Doubrovinski and K. Kruse. Self-organization of treadmilling filaments. *Phys. Rev. Lett.*, 99:228104, 2007.

[22] K. Dreblow, N. Kalchishkova, and K. J. Böhm. Kinesin bypassing blockages on microtubule rails. *Biophysical Reviews and Letters*, 4:139, 2009.

[23] M. Ebbinghaus and L. Santen. A model for bidirectional traffic of cytoskeletal motors. *Journal of Statistical Mechanics: Theory and Experiment*, page P03030, 2009.

[24] C. Enaud and B. Derrida. Sample-dependent phase transitions in disordered exclusion models. *Europhys. Lett.*, 66:83, 2004.

[25] P. Erdös and A. Rényi. On random graphs. *Publ. Math. Debrecen*, 6:290, 1959.

[26] M. R. Evans. Phase transitions in one-dimensional nonequilibrium systems. *Braz. J. Phys.*, 30:42, 2000.

[27] M. R. Evans, R. Juhász, and L. Santen. Shock formation in an exclusion process with creation and annihilation. *Phys. Rev. E*, 68:026117, 2003.

[28] M. Faxen, J. Plumbridge, and L. A.lsaksson. Codon choice and potential complementarity between mRNA downstream of the initiation codon and bases 1471 -1480 in 16S ribosomal RNA affects expression of glnS. *Nucleic Acids Research*, 19:5247, 1991.

[29] E. Foulaadvand, S. Chaaboki, and M. Saalehi. Characteristics of the asymmetric simple exclusion process in the presence of quenched spatial disorder. *Phys. Rev. E*, 75:011127, 2007.

[30] E. Foulaadvand, A. B. Kolomeisky, and H. Teymouri. Asymmetric exclusion processes with disorder: Effect of correlations. *Phys. Rev. E*, 78:061116, 2008.

[31] T. Gil, J. H. Ipsen, O. G. Mouritsen, M. C. Sabra, M. Sperotto, and M. J. Zuckermann. Theoretical analysis of protein organization in lipid membranes. *Biochim. Biophys. Acta*, 1376:245, 1998.

[32] A. Gopinathan, K. Lee, J. M. Schwarz, and A. J. Liu. Branching, capping, and severing in dynamic actin structures. *Phys. Rev. Lett.*, 99:058103, 2007.

[33] B. Govindan, R. Bowser, and P. Novick. The role of Myo2, a yeast class V myosin, in vesicular transport. *J. Cell Biol.*, 128:1055, 1995.

[34] U. Graf, H.-J. Henning, K. Stange, and P.-T. Wilrich. *Formeln und Tabellen der angewandten Mathematischen Statistik*. Springer, Berlin, 1987.

[35] P. Greulich. Eindimensionale getriebene Gittergase zur Modellierung intrazellulärer Transportprozesse. Diploma thesis, Universität zu Köln, 2006.

[36] P. Greulich, A. Garai, K. Nishinari, A. Schadschneider, and D. Chowdhury. Intra-cellular transport by single-headed kinesin KIF1A: effects of single-motor mechano-chemistry and steric interactions. *Phys. Rev. E*, 75:041905, 2007.

[37] P. Greulich and L. Santen. Active transport and cluster formation on 2D networks. *arXiv:0904.3890v1*, 2009.

[38] P. Greulich and A. Schadschneider. Phase diagram and edge effects in the ASEP with bottlenecks. *Physica A*, 387:1972, 2008.

[39] P. Greulich and A. Schadschneider. Single-bottleneck approximation for driven lattice gases with disorder and open boundary conditions. *Journal of Statistical Mechanics: Theory and Experiment*, 2008.

[40] P. Greulich and A. Schadschneider. Disordered driven lattice gases with boundary reservoirs and langmuir kinetics. *Phys. Rev. E*, 79:031107, 2009.

[41] H. Grzeschik, R. Harris, and L. Santen. Traffic of cytoskeletal motors with disordered attachment rates. *arXiv:0806.3845v1*, 2008.

[42] R. J. Harris and R. B. Stinchcombe. Disordered asymmetric simple exclusion process: Mean-field treatment. *Phys. Rev. E*, 70:016108, 2004.

[43] C. Heussinger and E. Frey. Stiff polymers, foams, and fiber networks. *Phys. Rev. Lett.*, 06:017802, 2006.

[44] J.-D. Huang, S. T. Brady, B. W. Richards, D. Stenoien, J. H. Resau, N. G. Copeland, and N. Jenkins. Direct interaction of microtubule- and actin-based transport motors. *Nature*, 397:267, 1999.

[45] C. W. Jacobs, A. E. Adams, P. J. Szaniszlo, and J. R. Pringle. Functions of microtubules in the Saccharomyces cerevisiae cell cycle. *J. Cell Biol.*, 107:1409, 1988.

[46] S. A. Janowsky and J. L. Lebowitz. Finite-size effects and shock fluctuations in the asymmetric simple-exclusion process. *Phys. Rev. A*, 45:618, 1992.

[47] S. A. Janowsky and J. L. Lebowitz. Exact results for the asymmetric simple exclusion process with a blockage. *J. Stat. Phys.*, 77:35, 1993.

[48] A. John, A. Schadschneider, D. Chowdhury, and K. Nishinari. Trafficlike collective movement of ants on trails: Absence of a jammed phase. *Phys. Rev. Lett.*, 102:108001, 2009.

[49] R. Juhász and L. Santen. Dynamics of an exclusion process with creation and annihilation. *J. Phys. A: Math. Gen.*, 37:3933, 2004.

[50] R. Juhász, L. Santen, and F. Iglói. Partially asymmetric exclusion processes with sitewise disorder. *Phys. Rev. E*, 74:061101, 2006.

[51] Y. Kafri and D. R. Nelson. Sequence heterogeneity and the dynamics of molecular motors. *J. Phys. Cond. Matt.*, 17:3871, 2005.

[52] J. F. Kane. Effects of rare codon clusters on high-level expression of heterologous proteins in Escherichia coil. *Curr. Op. Biotech.*, 6:494, 1995.

[53] S. Klumpp and R. Lipowsky. Active diffusion of motor particles. *Phys. Rev. Lett.*, 95:268102, 2005.

[54] S. Klumpp, T. M. Nieuwenhuizen, and R. Lipowsky. Movements of molecular motors: Ratchets, random walks and traffic phenomena. *Physica E: Low-dimensional Systems and Nanostructures*, 29:380, 2005.

[55] A. Kolomeisky, G. M. Schütz, E. B. Kolomeisky, and J. P. Straley. Phase diagram of one-dimensional driven lattice gases with open boundaries. *J. Phys. A*, 31:6911, 1998.

[56] A. B. Kolomeisky. Asymmetric simple exclusion model with local inhomogeneity. *J. Phys. A: Math. Gen.*, 31:1153, 1998.

[57] K. M. Kolwankar and A. Punnoose. Disordered totally asymmetric simple exclusion process: Exact results. *Phys. Rev. E*, 61:2453, 2000.

[58] Y. A. Komarova, A. S. Akhmanova, S. Kojima, N. Galjart, and G. G. Borisy. Cytoplasmic linker proteins promote microtubule rescue in vivo. *J. Cell Biol.*, 159:589, 2002.

[59] B. A. Korgel, J. H. van Zanten, and H. G. Monbouquette. Vesicle size distributions measured by flow field-flow fractionation coupled with multiangle light scattering. *Biophysical Journal*, 74:3264, 1998.

[60] J. Krug. Boundary-induced phase transitions in driven diffusive systems. *Phys. Rev. Lett.*, 67:1882, 1991.

[61] J. Krug. Phase separation in disordered exclusion models. *Braz. J. Phys.*, 30:97, 2000.

[62] J. Krug and P. A. Ferrari. Phase transitions in driven diffusive systems with random rates. *J. Phys. A: Math. Gen.*, 29:L465, 1996.

[63] G. Lakatos, T. Chou, and A. Kolomeisky. Steady-state properties of a totally asymmetric exclusion process with periodic structure. *Phys. Rev. E*, 71:011103, 2005.

[64] R. Lipowsky, S. Klumpp, and T. M. Nieuwenhuizen. Random walks of cytoskeletal motors in open and closed compartments. *Phys. Rev. Lett.*, 87:108101, 2001.

[65] C. Loverdo, O. Bénichou, M. Moreau, and R. Voituriez. Enhanced reaction kinetics in biological cells. *Nature Physics*, 4:134, 2008.

[66] C. MacDonald, J. Gibbs, and A. Pipkin. Kinetics of biopolymerization on nucleic acid templates. *Biopolymers*, 6:1, 1968.

[67] P. Meakin and F. Family. Structure and kinetics of reaction-limited aggregation. *Phys. Rev. A*, 38:2110, 1988.

[68] R. D. Mullins, J. A. Heuser, and T. D. Pollard. The interaction of ARP2/3 complex with actin: Nucleation, high affinity pointed end capping, and formation of branching networks of filaments. *Proc. Natl. Acad. Sci.*, 95:6181, 1998.

[69] K. Nagel and M. Schreckenberg. A cellular automaton model for freeway traffic. *J. Phys. I France*, 2:2221, 1992.

[70] M. E. J. Newman. Power laws, Pareto distributions and Zipf's law. *Contemporary Physic*, 46:323, 2005.

[71] K. Nishinari, Y. Okada, A. Schadschneider, and D. Chowdhury. Intracellular transport of single-headed molecular motors KIF1A. *Phys. Rev. Lett.*, 95:118101, 2005.

[72] J. D. Noh. Interacting particle systems in complex networks. *J. Kor. Phys. Soc.*, 50:327, 2007.

[73] J. D. Noh and H. Rieger. Random walks on complex networks. *Phys. Rev. Lett.*, 92:118701, 2004.

[74] Y. Okada and N. Hirokawa. A processive single-headed motor: Kinesin superfamily protein KIF1A. *Science*, 283:1152, 1999.

[75] A. Parmeggiani, T. Franosch, and E. Frey. Phase coexistence in driven one dimensional transport. *Phys. Rev. Lett.*, 90:086601, 2003.

[76] A. Parmeggiani, T. Franosch, and E. Frey. Totally asymmetric simple exclusion process with langmuir kinetics. *Phys. Rev. E*, 70:046101, 2004.

[77] D. A. Phoenix and E. Korotkov. Evidence of rare codon clusters within Escherichia coli coding regions. *FEMS Micobiol. Lett.*, 155:63, 1997.

[78] P. Pierobon. *Driven lattice gases: models for intracellular transport.* PhD thesis, LMU München: Faculty of Physics, 2006.

[79] P. Pierobon, M. Mobilia, R. Kouyos, and E. Frey. Bottleneck-induced transitions in a minimal model for intracellular transport. *Phys. Rev. E*, 74:031906, 2006.

[80] P. Pierobon, A. Parmeggiani, F. von Oppen, and E. Frey. Dynamic correlation functions and Boltzmann-Langevin approach for driven one dimensional lattice gas. *Phys. Rev. E*, 72:036123, 2005.

[81] V. Popkov, A. Rakos, R. D. Willmann, A. B. Kolomeisky, and G. M. Schütz. Localization of shocks in driven diffusive systems without particle number conservation. *Phys. Rev. E*, 67:066117, 2003.

[82] N. Rajewsky, L. Santen, A. Schadschneider, and M. Schreckenberg. The asymmetric exclusion process: Comparison of update procedures. *J. Stat. Phys.*, 92:151, 1998.

[83] A. Rákos, M. Paessens, and G. M. Schütz. Hysteresis in one-dimensional reaction-diffusion systems. *Phys. Rev. Lett.*, 91:238302, 2003.

[84] A. A. Rodal, L. Kozubowski, B. L. Goode, D. G. Drubin, and J. H. Hartwig. Actin and septin ultrastructures at the budding yeast cell cortex. *Molecular Biology of the Cell*, 16:372, 2005.

[85] A. Schadschneider. Traffic flow: a statistical physics point of view. *Physica A*, 313:153, 2002.

[86] G. Schütz and E. Domany. Phase transitions in an exactly soluble one-dimensional exclusion process. *J. Stat. Phys.*, 72:277, 1993.

[87] G. M. Schütz. *Phase Transitions and Critical Phenomena*, chapter 7, page 103. Academic Press, 2001.

[88] A. Seitz and T. Surrey. Processive movement of single kinesins on crowded microtubules visualized using quantum dots. *The EMBO Journal*, 25:267, 2006.

[89] I. N. Serdyuk, N. R. Zaccai, and J. Zaccai. *Methods in Molecular Biophysics.* Cambridge University Press, 2007.

[90] J. J. Sieber, K. I. Willig, C. Kutzner, C. Gerding-Reimers, B. Harke, G. Donnert, B. Rammner, C. Eggeling, S. W. Hell, H. Grubmüller, and T. Lang. Anatomy and dynamics of a supramolecular membrane protein cluster. *Science*, 317:1072, 2007.

[91] D. Sornette. *Critical Phenomena in Natural Sciences: Chaos, Fractals, Selforganization and Disorder.* Springer, Berlin, 2006.

[92] F. Spitzer. Interaction of Markov processes. *Advances in Math.*, 5:246, 1970.

[93] K. Stamer, R. Vogel, E. Thies, E. Mandelkow, and E.-M. Mandelkow. Tau blocks traffic of organelles, neurofilaments, and APP vesicles in neurons and enhances oxidative stress. *J. Cell Biol.*, 156:1051, 2002.

[94] D. Stauffer, F. W. Hehl, N. Ito, V. Winkelmann, and J. G. Zabolitzky. *Computer Simulation and Computer Algebra: Lectures for Beginners.* Springer, New York, 1993.

[95] G.-F. T.Chen and M. Inouye. Suppression of the negative effect of minor arginine codons on gene expression; preferential usage of minor codons within the first 25 codons of the Escherichia coli genes. *Nucleic Acids Res.*, 18:1465, 1990.

[96] G. Tripathy and M. Barma. Driven lattice gases with quenched disorder: Exact results and different microscopic regimes. *Phys. Rev. E*, 58:1911, 1997.

[97] G. Tripathy and M. Barma. Steady state and dynamics of driven diffusive systems with quenched disorder. *Phys. Rev. Lett.*, 78:3039, 1997.

[98] J. Valdez-Taubas and H. R. B. Pelham. Slow diffusion of proteins in the yeast plasma membrane allows polarity to be maintained by endocytic cycling. *Current Biology*, 13:1636, 2003.

[99] S. Varenne, D. Baty, H. Verheij, D. Shire, and C. Lazdunski. The maximum rate of gene expression is dependent on the downstream context of unfavourable codons. *Biochimie*, 71:1221, 1989.

[100] K. W. Wolf and K. J. Böhm. Organisation von Mikrotubuli in der Zelle. *Biologie in unserer Zeit*, 27.2:87, 1997.

[101] S. L. Wolin and P. Walter. Ribosome pausing and stacking during translation of a eukaryotic mRNA. *EMBO Journal*, 7:3559, 1988.

Acknowledgments

At this point I want to thank the people that helped me to complete this work. In particular (but not exclusive):

Ludger Santen for the supervision of my work in the second part of the thesis, and for helping me in the main conceptional aspects of the work. Moreover I thank him to allow me the possibility to keep my center of life in Cologne and to provide the conditions to work mainly remote from Saarbrücken, in particular for the possibility to travel with him between Bonn and Saarbrücken.

Andreas Schadschneider for supervising me in the first part of my thesis and leading me in the field of driven systems, while giving me the freedom to develop own ideas .

My office co-workers **Alexander Wollny, Lucas Hollender and Mehrnaz Bozorgh-Nia**, for fruitful discussions and for the good working atmosphere.

Konrad Böhm and Manfred Schmitt for providing some experimental background motivation for the thesis.

Otto Pulkkinen, Johannes Berg, Maximilian Ebbinghaus, Debashish Chowdhury and Joachim Krug for fruitful discussions that helped me in some aspects of the work.

And of course **my parents, Brigitte and Karl-Otto** for controversal discussions and improving suggestions for my thesis. Moreover, I also thank for inspiring my interest in science already in my early years and helping me in any aspects of life .